Universidade de São Paulo
Instituto de Astronomia, Geofísica e Ciências Atmosféricas
Departamento de Geofísica

Jamison Assunção

Dynamic topography and mantle convection induced by subduction of oceanic lithosphere: a numerical approach

São Paulo
2019

Jamison Assunção

Dynamic topography and mantle convection induced by subduction of oceanic lithosphere: a numerical approach

Dissertation presented to the Instituto de Astronomia, Geofísica e Ciências Atmosféricas of the Universidade de São Paulo to obtain the title of Master in Geophysics.

Concentration Area: Geophysics
Supervisor: Prof. Dr. Victor Sacek

Versão Corrigida. O original encontra-se disponível na Unidade.

São Paulo
2019

Dedico este trabalho aos inesquecíveis.

Acknowledgements

First of all, I would like to thank my supervisor, Victor Sacek, for all the support, patience and knowledge. It will always be a pleasure to learn from you and with you.

I would like to thank my family, specially my mother Giselma, my brother Lucas, and my dog Susy as well (she's a very good girl).

I would like to thank all the people who gave me support, inside and outside the university, which includes my friends and all the employees from IAG.

A special thanks to Guilherme and Felipe who I can count on.

Many thanks to the Trindade and the Coelho families, who lent me the first books I ever read and gave me the first piece of knowledge I ever studied.

I would like to thank those people who didn't know they helped me. I will let you know, eventually.

I would like to thank CNPq and Petrobras for their financial support.

Thank you very much, guys.

“*Se podes olhar, vê. Se podes ver, repara.*”

Livro dos Conselhos

Resumo

Uma das principais forças que guiam a tectônica de placas é induzida pela subducção da litosfera oceânica fria e densa, criando uma flutuabilidade negativa em relação ao manto mais quente adjacente. Esse movimento descendente perturba o padrão de fluxo principalmente no manto superior, afetando também o deslocamento vertical da superfície da Terra na escala de tempo geológica, fenômeno conhecido como topografia dinâmica. Devido à complexidade física desses processos, uma maneira natural de estudar a subducção de placas litosféricas é através do uso de modelos numéricos. O objetivo do presente trabalho é o desenvolvimento de cenários numéricos que reproduzam alguns dos principais aspectos observados sobre geometria e cinemática de placas oceânicas em subducção com base em vínculos geofísicos. Especificamente, concentrei minha atenção na subducção da placa de Nazca sob a litosfera continental da América do Sul, a uma latitude de 18°S. Na primeira parte deste projeto, várias simulações numéricas foram feitas para estudar a flutuabilidade da placa de Nazca. Os resultados mostraram que, para uma litosfera oceânica relativamente mais espessa, a placa tende a defletir para baixo em relação à geometria observada da placa, mas resiste mais à flexão devido à sua rigidez. Já a crosta oceânica contribuiu para uma deflexão ascendente da placa em subducção, mesmo quando a densidade resultante de toda a placa era maior que a densidade do manto astenosférico circundante. A melhor combinação encontrada para a menor deflexão foi a de uma litosfera oceânica de 80 km com uma crosta oceânica de 8 km com uma densidade de 2800 kg/m^3. Na segunda parte deste projeto, a placa de Nazca foi simulada por mais de 50 Myr para estudar sua estagnação próximo à transição para o manto inferior. Percebeu-se que o aumento da viscosidade por si só não pode explicar a horizontalização da placa em 660 km, pois a mudança de fase, induzindo um aumento da densidade no manto inferior, foi crítico para simular-se a estagnação de placas oceânicas acima do manto inferior.

Palavras-chave: subducção da litosfera oceânica; convecção do manto; topografia dinâmica; método dos elementos finitos.

Abstract

One of the main forces that drive plate tectonics is induced by the subduction of cold and dense oceanic lithosphere, creating a negative buoyancy relative to the adjacent hotter mantle. This downward movement perturbs the flow pattern mainly in the upper mantle, also affecting the vertical displacement of the Earth's surface in the geological time scale, phenomenon known as dynamic topography. Due to the physical complexity of these processes, a natural way to study subduction of lithospheric plates is through the use of numerical models. The aim of the present work is the development of numerical scenarios that reproduce some of the main aspects observed about geometry and kinematics of oceanic plates in subduction based on geophysical constraints. Specifically, I focused my attention on the subduction of the Nazca plate under the continental lithosphere of South America, at a latitude of 18°S. On the first part of this project, several numerical simulations were made to study the buoyancy of the Nazca plate. The results showed that for a relatively thicker oceanic lithosphere, the slab tends to deflect downwards, but it resists more to bending due to its rigidity. An opposing buoyant force produced by the oceanic crust contributed to an upward deflection of the subducting slab even when the resulting density of the entire slab was greater than the surrounding asthenospheric mantle density. The best combination found for the smallest deflection was that of an 80 km thick oceanic lithosphere with an 8 km thick oceanic crust with a density of 2800 kg/m^3. On the second part of this project, the Nazca plate was simulated for more than 50 Myr to study its stagnation on the upper-to-lower mantle boundary. It was noticed that increasing the viscosity alone cannot explain slab flattening at 660 km, as phase change reflected by the increase in density was critical when studying slab penetration in the lower mantle.

Keywords: subduction of oceanic lithosphere; mantle convection; dynamic topography; finite element method.

List of Figures

Contents

Chapter 1

Introduction

In computational fluid dynamics, the numerical simulation of mantle convection represents one of the most challenging problems, mainly due to its complex rheology through the geological history of planet Earth (Ranalli, 1995). This becomes evident when we compare the large variations in viscosity in the interior of the planet relative to other fluids: the effective viscosity of the Earth's mantle can range 10 orders of magnitude ($10^{16} - 10^{26}$ Pa·s, Gerya, 2010), while the effective viscosity of other geophysical fluids, like water in the ocean and the air in the atmosphere, varies less than one order of magnitude. Additionally, the convection in the mantle presents non-linear behavior, specially in the cold and rigid lithosphere, turning the convergence of the numerical solutions a challenging task (Zhong et al., 2007).

Specifically, the simulation of slabs in subduction to reproduce the final fate of cold oceanic lithosphere in the interior of Earth's mantle is more difficult to be simulated than the pure convection in the asthenosphere, without the incorporation of the rigid lithosphere in the convection, known as Rayleigh-Taylor-like models (Gerya, 2010). In the Rayleigh-Taylor-like models, the asthenospheric mantle is convecting continuously, interacting with the base of the lithospheric mantle, that remains nearly motionless close to the free surface. This kind of regime is known as stagnant lid model (Korenaga, 2013), assumed to be the present geodynamic regime of other terrestrial planets in the Solar System, like Mars and Venus (Figure 1.1a). On the other hand, in the plate tectonics regime, the lithospheric plate actively participate in the convection in the mantle, being continuously recycled in the Earth's interior (Figure 1.1b). In this situation, the penetration of a rigid plate into the weak asthenosphere involves the simulation of abrupt spatial variations in viscosity, making the convergence of the numerical model harder to be achieved.

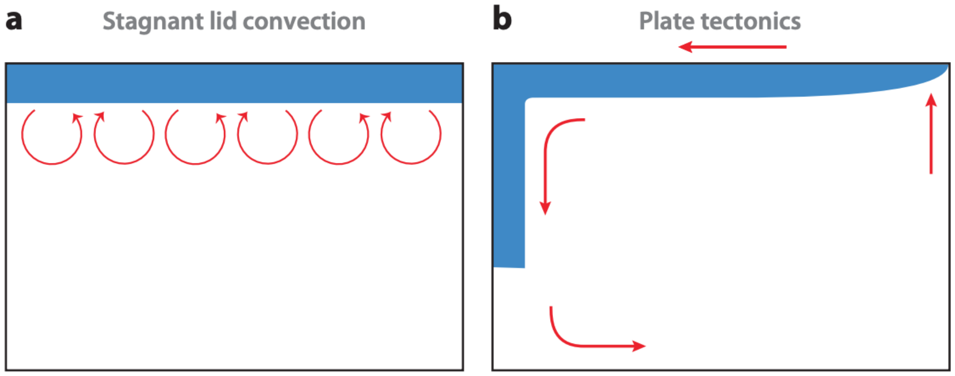

Figure 1.1: Comparison of two possible convective regime in terrestrial planets. (a) Stagnant lid regime; (b) Plate tectonics regime. Extracted from Korenaga (2013)

One of the first numerical experiments created to study subduction of cold lithosphere in the Earth's mantle was designed by Christensen and Yuen (1984), taking into account what is the effect of phase transformations during the downward movement of the slab, although the geometry of the slab is oversimplified, assuming essentially vertical movement of the plate. In the following years, new numerical experiments were developed to create asymmetric downwellings, compatible with the observed angle of subduction of oceanic lithosphere (e.g. Gurnis and Hager, 1988; King and Hager, 1994; Ita and King, 1998).

Concomitant with the development of numerical models of mantle convection in the last decades, parallel research was made to quantify the surface effect of mantle convection, especially mantle flow induced by subduction of lithospheric plates (e.g. Hager et al., 1985; Mitrovica et al., 1989; Gurnis, 1992; Moucha et al., 2008), affecting, for example, the evolution of sedimentary basins. The convecting pattern in the asthenosphere can exert viscous forces on the base of the rigid lithosphere causing vertical displacement of the surface of the planet. This displacement is the result of mantle flow caused by density variations as a function of mainly temperature and composition. The convecting mantle ascends and descends interacting and modifying the boundary between the rigid lithosphere and the asthenosphere (Braun, 2010). In regions where the mantle flows upwards, there will be positive stresses under the lithosphere which will result in uplift of the surface. In contrast, regions where the mantle flows downwards will induce the subsidence of the surface due to negative stresses. This change in topography caused by mantle flow is known as dynamic topography (see Figure 1.2).

The calculation of mantle convection and the resulting dynamic topography involves

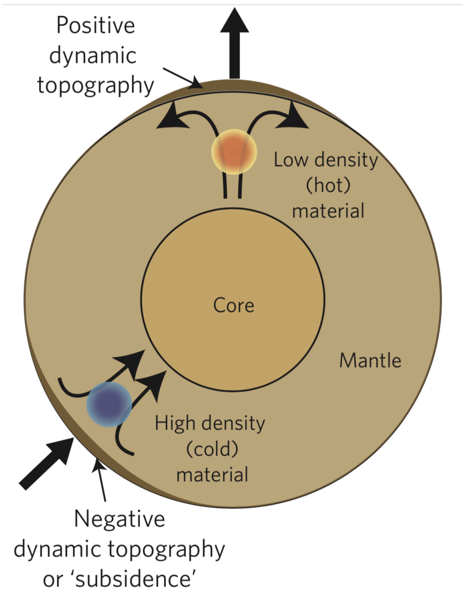

Figure 1.2: Simple illustration of how upwelling and downwelling mantle flows correlate with dynamic topography on the surface. Adapted from Braun (2010).

the solution of conservation equations of mass, energy and momentum. These equations are analytically solved only on relatively simple scenarios (Turcotte and Schubert, 2002). Because of the complex nature of the convection problem, numerical approach is indispensable to solve the model problem where initial conditions, boundary conditions, and constitutive relations are needed (Ribe, 2007).

The goal of this project was to calculate how the topography evolved within the South American plate being affected by the subduction of the Nazca plate. For that, I used the MD3D numerical model (Sacek, 2017) to simulate mantle convection and calculated the topography from the thermal and density data generated. In addition, I studied how the buoyancy of the subducting Nazca changed based on some of the parameters that were considered.

In the second chapter of this dissertation, I discuss about previous numerical models used to study the subduction pattern of the Nazca plate and its effect on the landscape evolution of South America, contextualizing the present work. The third chapter is dedicated to show the mathematical formalism to describe the mantle convection model and the numerical approach using the finite element method. Additionally, this chapter presents some general aspects about the model setup used in the numerical scenarios to simulate slab subduction.

The forth and fifth chapters present the main results obtained in this project. The forth chapter shows numerical experiments about the relationship between the buoyancy of the subducting slab and the angle of subduction, exploring how the thickness and density structure for the oceanic crust and lithospheric mantle affect the geometry of the plate. The fifth chapter extends these previous simulations for up to 100 million years of simulation, testing the numerical stability of the code and the compatibility of the results with geophysical constraints, analyzing the geometry of the plate depending on boundary conditions and the rheological properties of the upper and lower mantle.

Finally, the sixth chapter is dedicated to the main conclusions of the work, giving additional information for future works and how to improve the present scenarios.

Chapter 2

Dynamic topography in South America induced by the subduction of the Nazca Plate

In a first approximation, the main topographic features in our planet can be explained by flexural isostasy of the rigid lithosphere. However, part of the vertical movement of the Earth's surface cannot be explained without the incorporation of the flow dynamics in the mantle. The correct separation of the influence of the isostatic and flexural components from the dynamic mantle influence is essential to understand the mechanisms involved in the creation and evolution of sedimentary basins. Because isostatic and flexural models are not unique due to uncertainties relative to the geophysical structure of the lithosphere, independent dynamic topography models are also important to explain the surface evolution of the Earth, as studies in the Andean region have shown (e.g. Dávila and Lithgow-Bertelloni, 2013).

Therefore, the regional topography can be broken down in two groups by its genetic mechanism (Lithgow-Bertelloni and Silver, 1998; Braun, 2010). The first group is that of isostatic and flexural compensation, related to the changes in density and thickness of the lithosphere. The second group is the mantle-induced topography, the dynamic topography. Because of that, if we remove the isostatic topography from the observed topography, we would end up with a dynamic topography map. However, as previously commented, this is not a simple task because the uncertainties on the isostatic and flexural models prevent us from making such statement and we should refer to this map as residual topography map instead of dynamic topography. Nevertheless, the difference between dynamic topography and isostatic compensated topography do not differ beyond a few hundred meters as the topographic load works against the mantle flow, and about 90% of the observed topography can be explained by the isostatic component (Molnar et al., 2015).

Figure 2.1 shows two maps of the residual topography calculated by Steinberger (2007) and Steinberger et al. (2017) for the whole Earth. Both Figures 2.1a and 2.1b are very different from the wavelength perspective, which adds to the uncertainties regarding the determination of the dynamic topography from theses models as well.

A direct strategy to calculate the dynamic topography is the simulation of the mantle flow based on a rheological stratification of the crust and mantle, done in detail in regional or continental scale (Dávila and Lithgow-Bertelloni, 2013, and references therein). In South America, the subduction of the Nazca Plate induced a regional subsidence that extends more than 1000 km eastward from the Andean Cordillera, affecting the evolution of the interior sedimentary basins (Flament et al., 2015, Figure 2.2), creating a net subsidence of the western lowlands in South America of nearly 500 m during the last 50 Ma. This dynamic topography pattern is in agreement with previous calculations of dynamic topography derived by Shephard et al. (2010). However, both articles are not based on the direct simulation of the subduction of the Nazca plate, but used seismic tomography data to create the density contrast model in the upper mantle, blurring the geometry of the Nazca plate. Additionally, in their reverse numerical model, some simplifications were done to make the code stable backward in time: (1) they artificially increased the effective viscosity of the asthenosphere, making the model less chaotic (more deterministic) for tens of million years; (2) they suppressed some diffusive terms in the energy equation to be numerically stable. A noticeable exception is the work of Eakin et al. (2014), where the geometry of the oceanic lithosphere was directly used to calculate the dynamic topography in western Amazonia based on forward models of mantle convection.

In the present work I studied the mantle convection dynamics and the consequent dynamic topography induced by the subduction of the Nazca plate at the latitude of 18°S. The choice of this latitude coincides with the active Pantanal Basin (Figure 2.3), which is situated in the Upper Paraguay River depression, west-central Brazil. It is a Cenozoic sedimentary basin structured by faults and its sedimentation started after the Tertiary period with the development of a foreland system during the Quaternary (de Freitas, 1951). The basin has a surface area of about $150,000$ km^2 and it has a sedimentary package of up to 500 m. Although the long wavelength feature of dynamic topography cannot explain the localized depression of the Pantanal basin, the aim of the present work is a tentative

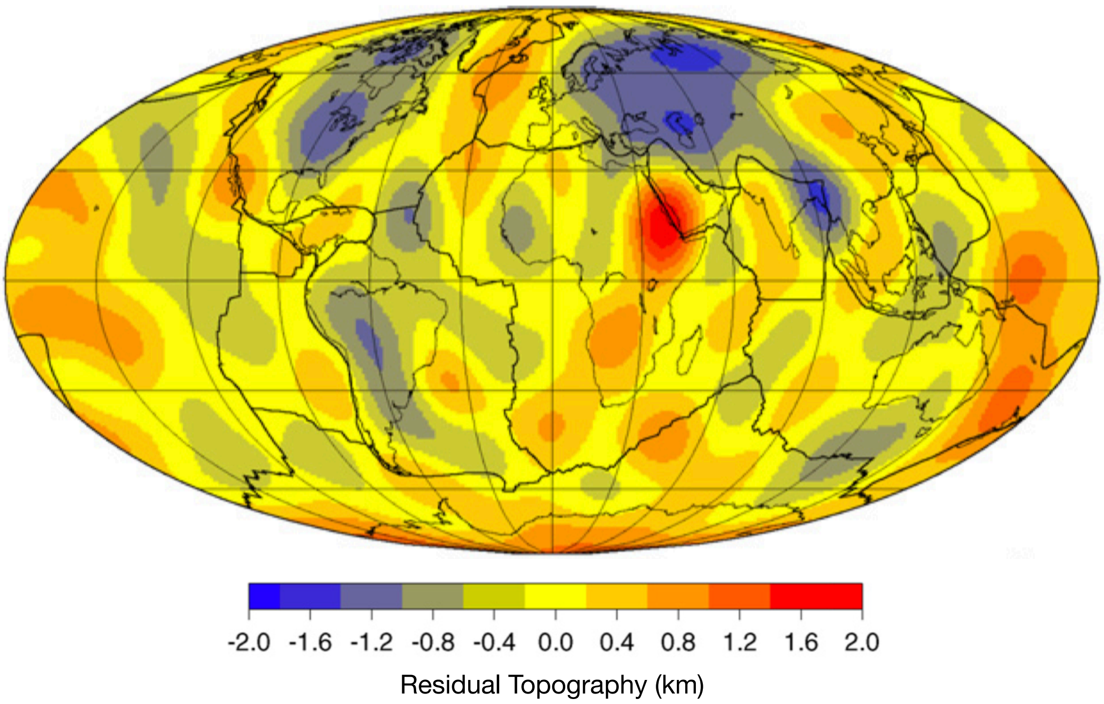

(a) Global residual topography. Adapted from Steinberger (2007).

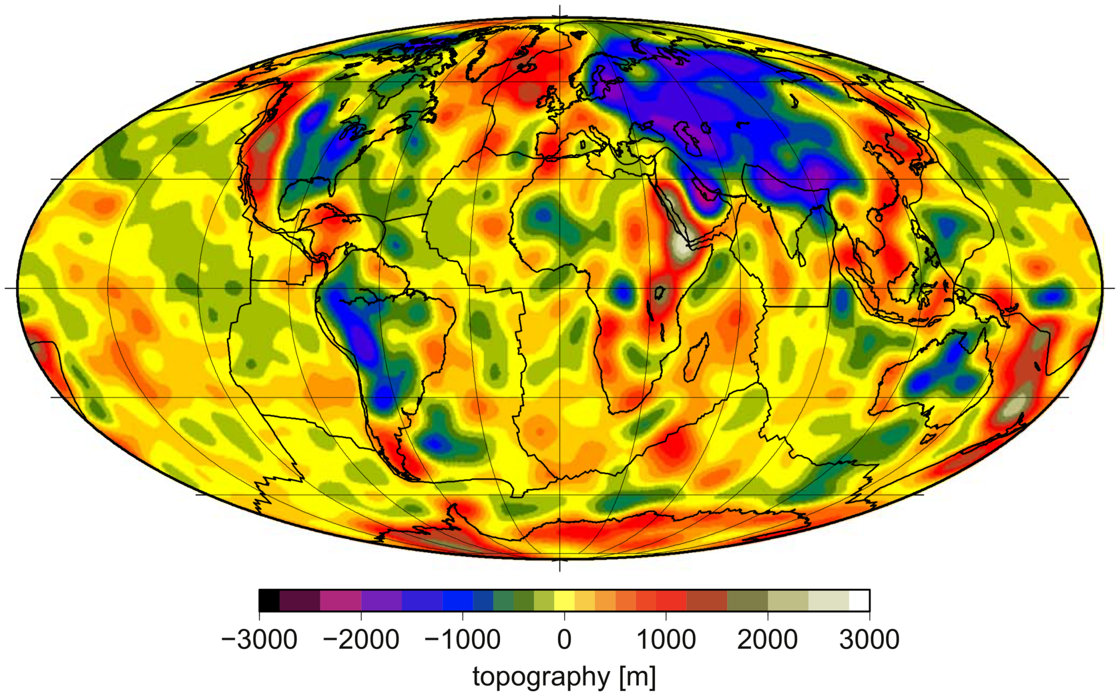

(b) Global residual topography. Adapted from Steinberger et al. (2017).

Figure 2.1: Maps showing the global residual topography that, ideally, should coincide with the dynamic topography.

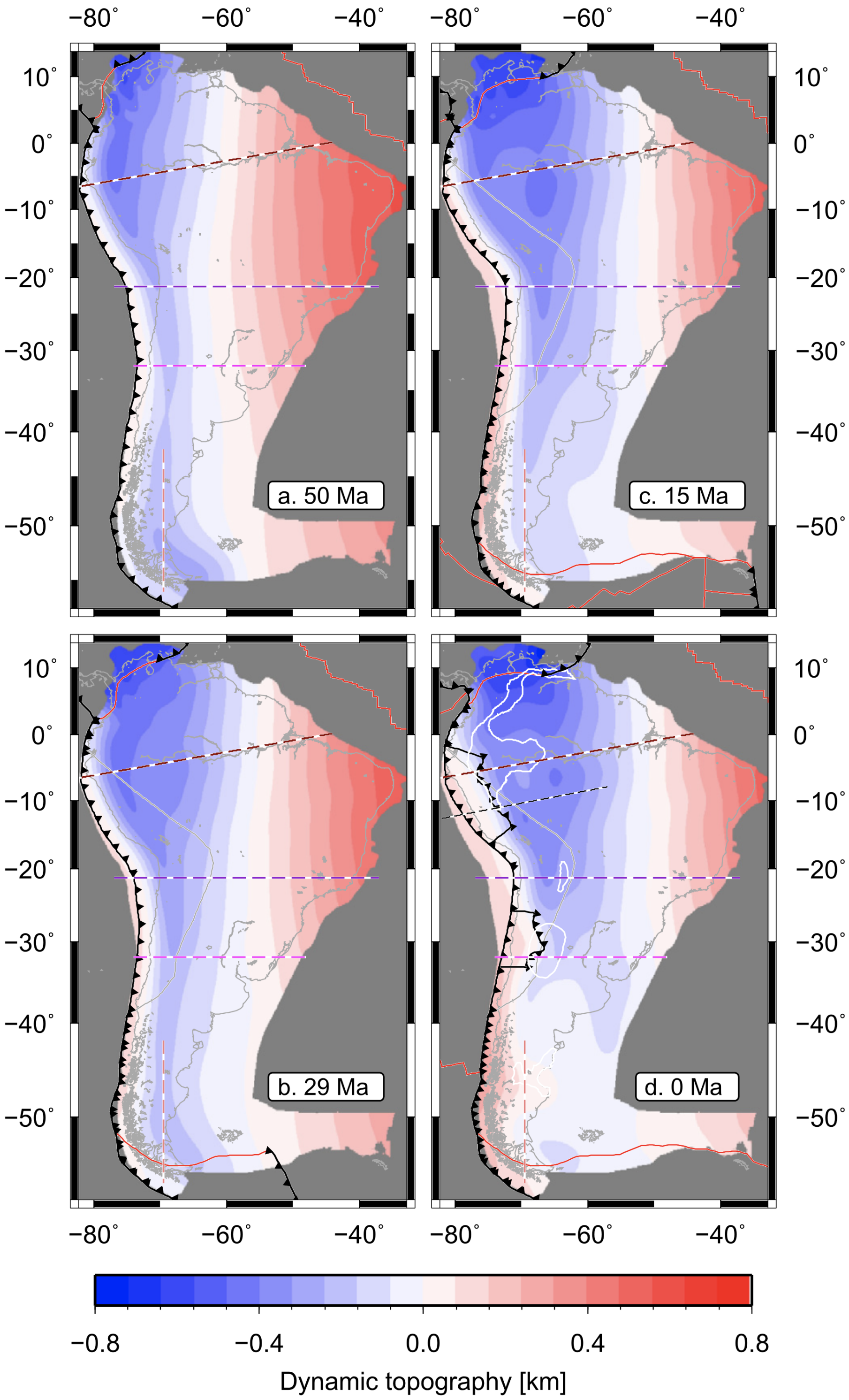

Figure 2.2: Absolute dynamic topography for South America during the last 50 Ma. Extracted from Flament et al. (2015). Observe that the vertical variations of dynamic topography is represented by the changes in absolute topography through time.

calculation of the magnitude of dynamic topography, resulting in a regional subsidence.

The origin of the basin is still in debate and likely developed as a result of the Andean chain load on the west causing uplift and flexural extension of the upper crust (Ussami et al., 1999). However, shallow and reverse faulting events can be observed in the basin (horst and graben structures), which are incompatible with such an extensional scenario (Assumpção and Suárez, 1988). Earthquakes associated with these faults are invoked as responsible for the differential subsidence that gives the basin one of its most recognizable characteristic, permanent flooded areas (Bergier and Assine, 2016).

It is also a debate if the basin is situated on the fore-bulge, as flexural models suggest (Ussami et al., 1999), or if it rests on the back-bulge (Horton and DeCelles, 1997), which justifies its sediment content. Nonetheless, the proposed flexural model needs a very large value for the elastic thickness of the lithosphere, which also results in a flexural bulge too far away from the load.

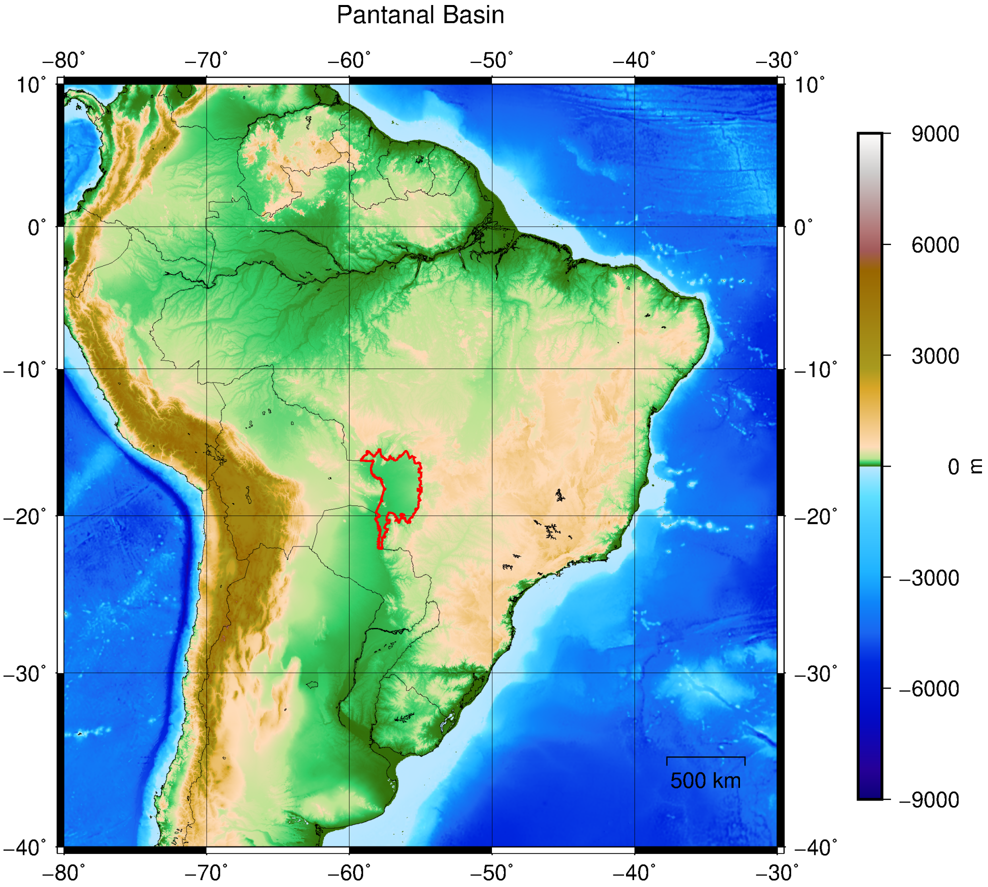

Figure 2.3: Topographic map of South America showing the Pantanal basin perimeter in red.

The basin is also situated over a low velocity anomaly in the asthenosphere (Schaeffer and Lebedev, 2013; French and Romanowicz, 2014; Auer et al., 2014), as can be seen in the surface waves tomography on Figure 2.4. This low velocity signature can be a low density region, which is commonly associated with relatively high temperature, but the signature can be an indicative of its composition as well.

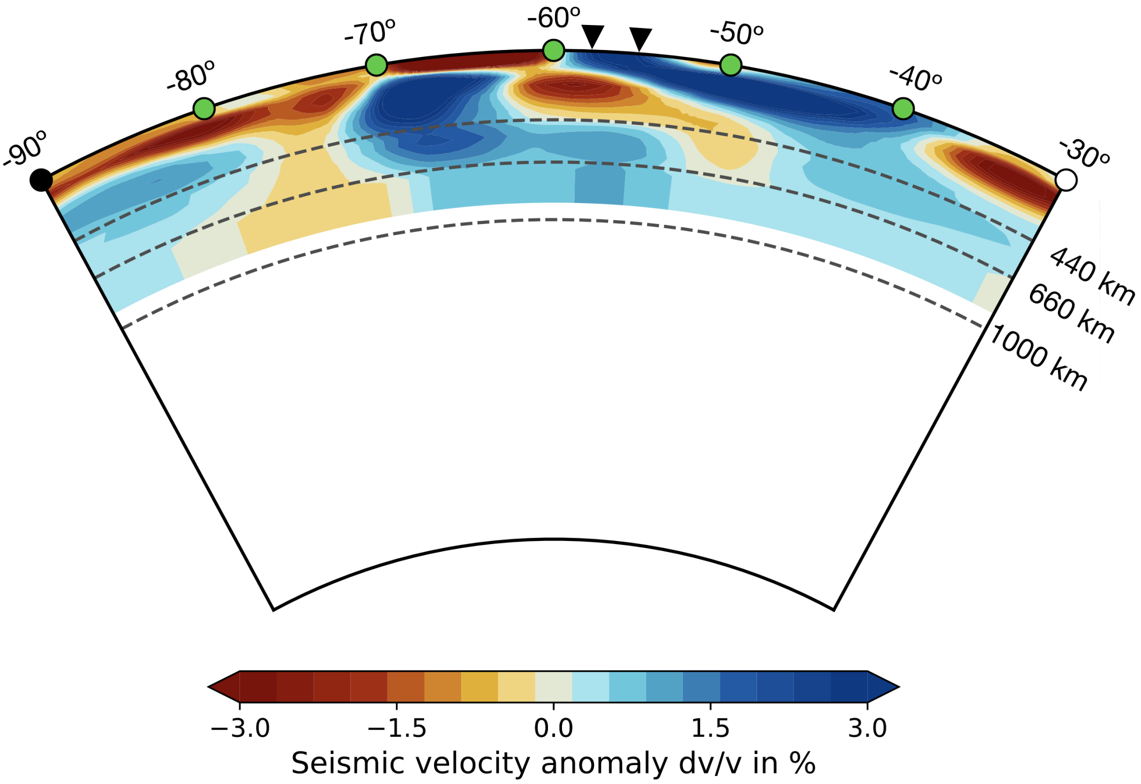

Figure 2.4: Surface wave tomography model SL2013sv. The latitude of the cross section is 18.00°S, which approximately crosses the center of the Pantanal basin. The black triangles indicate the longitudinal limits of the basin.

The map from Steinberger (2007) shows a negative residual topography for the Pantanal basin area. Assuming that the residual topography reasonably represents the dynamic topography, this suggests that the basin has a negative dynamic topography component with a value around −1.0 km in addition to the isostatic topography. However, the updated residual topography map from Steinberger et al. (2017) suggests the residual subsidence within the region of less than 500 m in magnitude.

Chapter 3

Methods

There are many criteria that were adopted to perform the numerical simulations proposed by this work. In this chapter I will introduce the numerical code and discuss the initial conditions, presenting the data used for the geometry of the model, as well as the formulations that were used to calculate the initial thermal structure, and also the justification of the approximations that were taken.

3.1 Numerical Methods

The equations which describe the behavior of the mantle are those of conservation of mass, momentum, and energy (Zhong et al., 2007). Considering the mantle to be a fluid in the geological time scale, with advective inertial forces smaller than the viscous forces (Stokes flow or creeping flow) and using the Boussinesq approximation, these equations assume the form of equations 3.1, 3.2, and 3.3 to solve the Stokes flow for an incompressible fluid.

$$u_{i,i} = 0 \tag{3.1}$$

$$\sigma_{ij,j} + g\rho_0\alpha T\delta_{i3} = 0 \tag{3.2}$$

$$\frac{\partial T}{\partial t} + u_i T_{,i} = \kappa T_{,ii} + \rho_0 H - \frac{\alpha T g u_3}{C_p} \tag{3.3}$$

where u_i is the velocity in the i direction, $\sigma_{i,j}$ is the stress tensor (Equation 3.4), g is the acceleration of gravity, ρ_0 is the mantle reference viscosity, α is the thermal expansivity, T is temperature, δ_{ij} is a Kroenecker delta function, t is the time, κ is the thermal diffusivity, and C_p is the specific heat. Repeated indexes in the same term represent summation and indexes after comma are partial derivative to a spatial coordinate.

$$\sigma_{ij,j} = -P\delta_{,ij} + \eta(u_{i,j} + u_{j,i}) \tag{3.4}$$

where P is the dynamic pressure, and η is the viscosity.

For this work, I used the MD3D numerical code (Sacek, 2017), which solves equations 3.1, 3.2, and 3.3. Figure 3.1 represents a flow chart of how the numerical code solves these conservation equations. The code accepts inputs such as files containing an initial velocity field, an initial thermal configuration, and initial interfaces to discriminate the different rheological units. Velocity boundary conditions and temperature boundary conditions were also used within MD3D and will be discussed in this chapter.

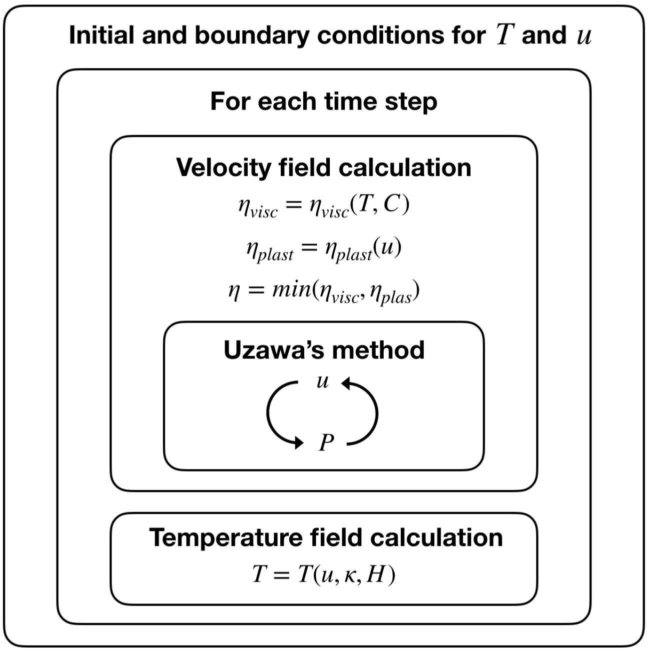

Figure 3.1: Flow chart showing the steps the MD3D numerical code takes to solve the equations of conservation of mass, momentum and energy.

3.2 *Initial conditions*

For the current study method, many initial conditions had to be considered to simulate the convecting-mantle. For a cross section of the Earth, I set a reasonable geometry for the geodynamic units, an initial thermal structure, a rheological model, an initial velocity field, and finally thermal and velocity boundary conditions. Calculating initial conditions such as the temperature field is nontrivial and it depends on thicknesses and temperature models which yet are objects of study.

The general purpose of all the approximations that were taken in this work was to allow a simple yet realistic model for the initial thermal and geometry structures. Therefore, all the initial conditions will be discussed thoroughly in the next subsections, taking into consideration both the model problem, the time constrains, the data that was used and the literature.

3.2.1 Layer model

For this study, it is important to define what was considered to be a rheological unit. A rheological unit is simply a geodynamic unit with a set of compositional parameters, such as viscosity and density.

For numerical simulations, discriminating rheological units consists one of the main challenges when defining the initial conditions. The interfaces between these units delimit where all the intrinsic parameters will be, how the material will be affected by the extrinsic parameters, and how the units will interact with one another. For this study the temperature, rheology, velocity and their respective boundary conditions were calculated from the geometry of the rheological units.

There are uncertainties regarding the determination of the depths of interfaces, such as the crust-mantle boundary (Mohorovičić discontinuity, which I will refer to as Moho, for short), the lithosphere-asthenosphere boundary (LAB), and the upper-to-lower mantle boundary. For this study, I'm not considering upper and lower crusts as distinct rheological units. Because of these uncertainties, every numerical simulation is limited by the geometry of its units and its results will depend on the adopted interfaces as it is the delimiter of the properties of the medium (Bercovici, 2007).

It is important to point out that there are situations where we cannot calculate dynamic topography by only removing the isostatic component from the observed topography (Braun, 2010). This residual topography can be explained by both dynamic topography and the deviations from the thickness models (which are the sources to flexural and isostatic models). Until certain extent, when one performs a simulation using a thickness model, the thickness model itself is being tested. With that in mind, I decided to use the LITHO1.0 model (Pasyanos et al., 2014) together with the Slab2 model (Hayes et al., 2018) for this work as they are reasonable starting models, consistent with many studies (Yuan and Romanowicz, 2010; Priestley and Tilmann, 2009).

The LITHO1.0 model is a tessellated model of the crust and upper mantle and it provided the data to trace all the interfaces within the continental and oceanic lithospheres (Figure 3.2 and Figure 3.3). The model was saturated at a minimum depth of 100 km for the LAB (inside the continental region, as suggested by Pasyanos et al. (2014)) and it was saturated at a maximum depth of 10 km for the Moho (inside the oceanic region). This saturation steps were taken because the model provides unrealistic small depths for the LAB in the continental areas and very thick oceanic crust. This model does not provide information about the structure of the subducting slabs and the Slab2 model was used to complement it.

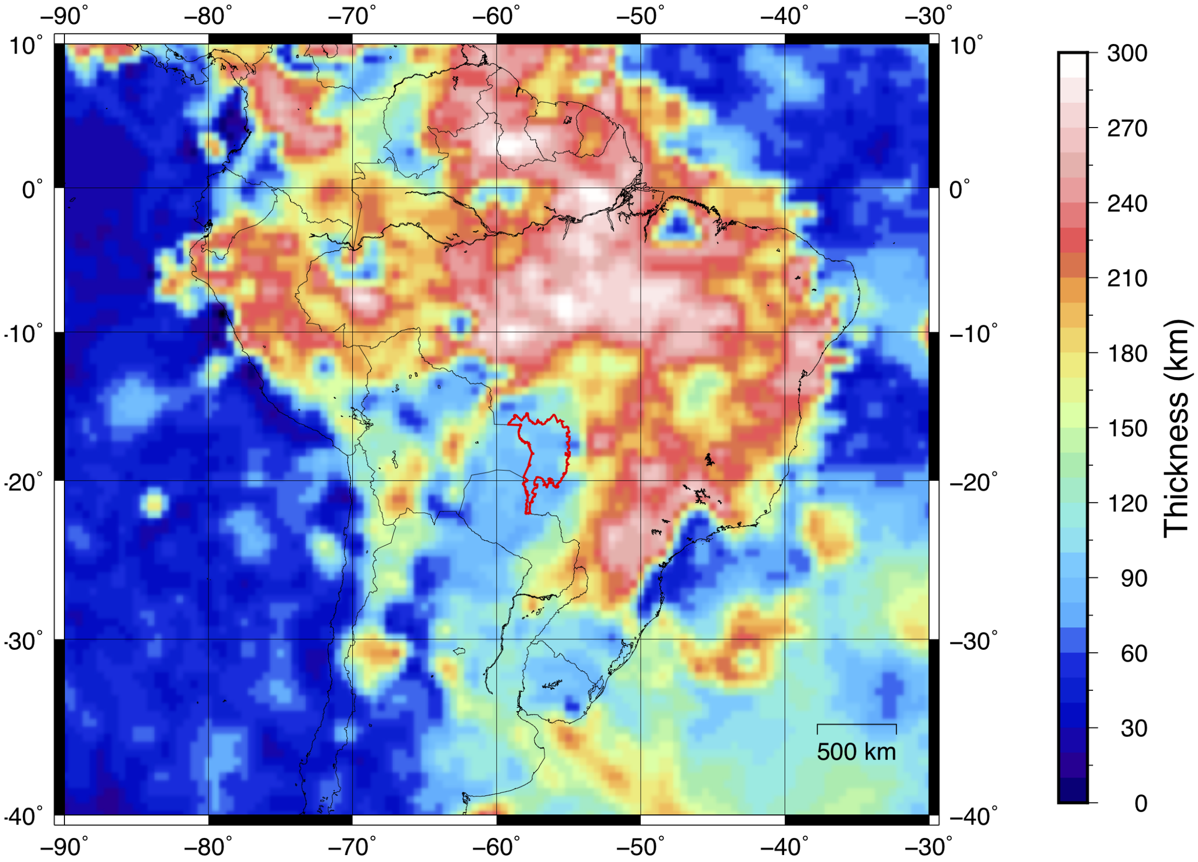

Figure 3.2: Map showing the LAB Depth resampled from the LITHO1.0 model, without any saturation.

The Slab2 model is a global three dimensional geometry model of active subducting slabs and it contains information about the depth of the subducting slabs as well as their thicknesses, dip angles, and strike angles (Figure 3.4). One of its limitations is that the slab geometry is calculated until the deepest earthquake, not representing the full shape of the plate as some tomography models do (Fukao and Obayashi, 2013). When combined with

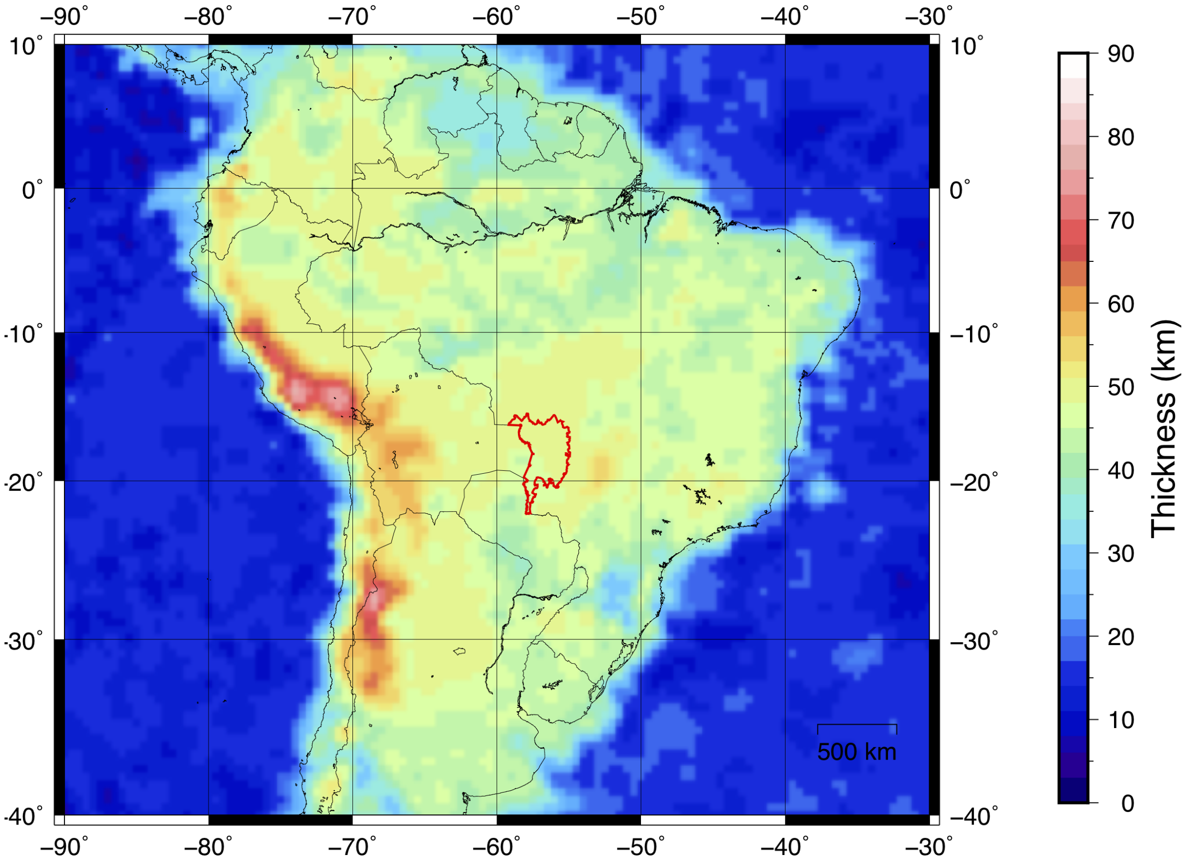

Figure 3.3: Map showing the Crust Depth resampled from the LITHO1.0 model, without any saturation.

the LITHO1.0, such resulting model will provide a global thickness database, containing the geometry of the whole lithosphere, as well as of its subdivision.

The steps to make a depth model for the South American region was very straightforward. I first considered the depths of the different geodynamic units provided by the LITHO1.0 model and resampled them to the model problem grid. The subducting slab depths from the Slab2 model were then resampled to the same grid and added over it. Finally, the initial dip angle of the subducting slab was considered to extrapolate linearly the subducting slab until its bottom crossed the LAB depth of the LITHO1.0 model, connecting the subducting slab to the lithosphere and limiting the mantle and continental wedges.

In the South America region, the Nazca plate is descending under the South American plate from west to east. Figure 3.5 shows the product of the LITHO1.0 and the Slab2 models combined to make a geometry model crossing South America at latitude 18.00°S,

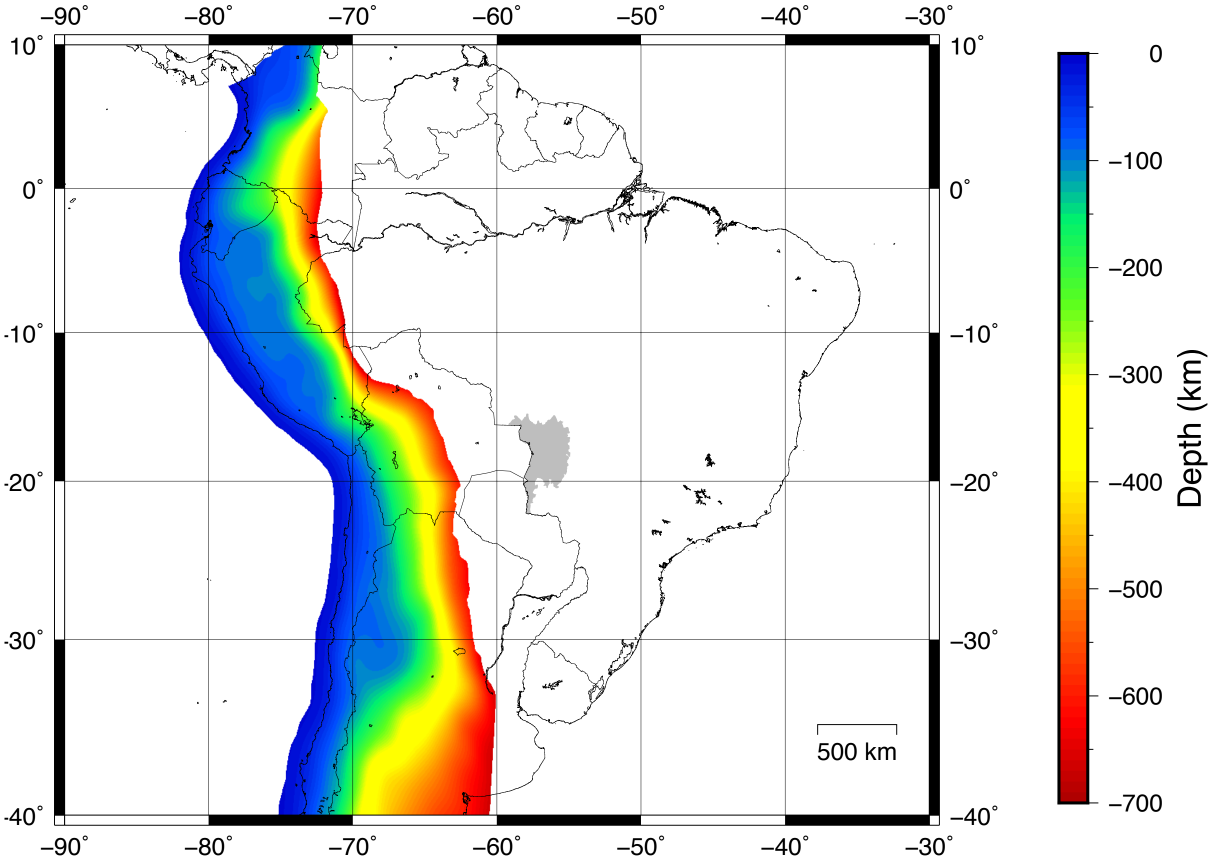

Figure 3.4: Map showing the depth of the upper surface of the Slab2 model and the location of the Pantanal basin (in grey).

at approximately the middle of the Pantanal basin. This model will be used in Chapter 4 and Section 5.2.1. Figure 3.6 show the same model, but with a ridge-like structure on the west border that is going to be used in Section 5.2.2.

The identified units in Figure 3.5 are the units from the LITHO1.0 model which will be considered in this work. The figure also shows an artificial unit called Lubricant Layer. The Lubricant Layer is a layer 60 km thick which corresponds to a zone of different rheology from the "normal" continental lithosphere. For this work, this difference consist in a less viscous material, which will be discussed in the next sections. The role of this unit was to ease the subduction of the Nazca plate, providing a surface for the slab to slide and a volume to allow some deformation. This procedure is commonly used in geodynamic models to simulate subduction zones King (2007).

This work differs from other approaches such as those from Flament et al. (2015) and Hu et al. (2017) by actually using a topography for the subducting slab, where the dip of

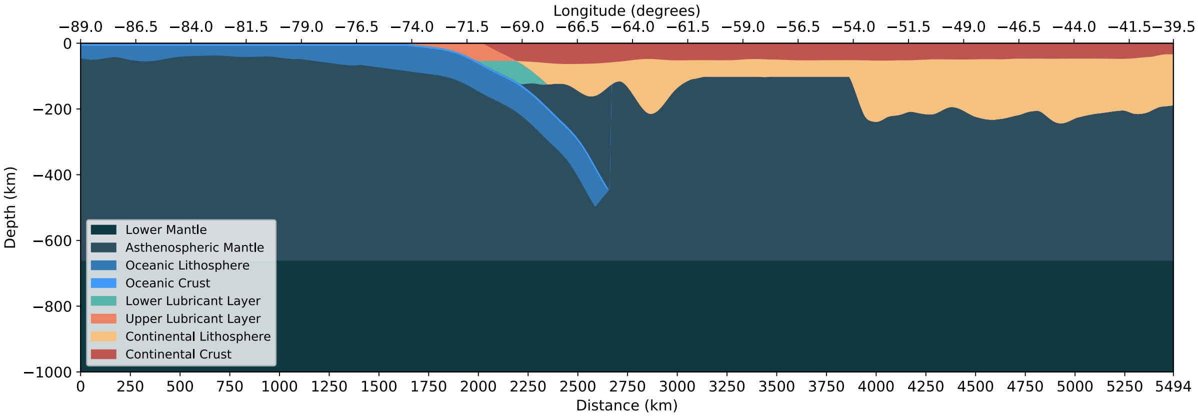

Figure 3.5: Example of geometry model at latitude 18.00°S showing the Nazca plate subducting under the South America plate.

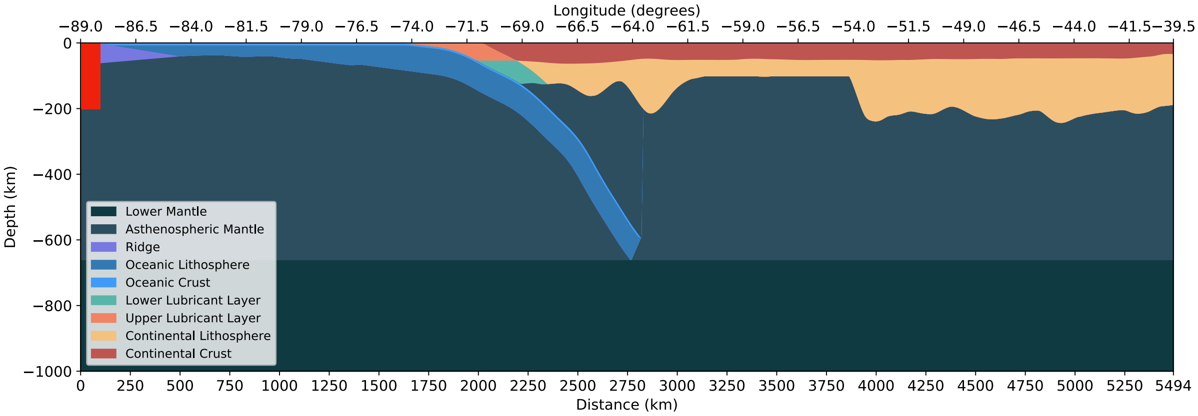

Figure 3.6: Example of geometry model at latitude 18.00°S showing the Nazca plate subducting under the South America plate with a ridge-like structure on the west border, also with a low viscosity region (red rectangle).

the slab is a function of its position.

3.2.2 Thermal structure

The approach to establish an initial thermal structure was to divide it in three steps. The first step was using the LITHO1.0 model to calculate a background temperature field. The second step was calculating the temperature for the subducting slab using the Slab2 model and replacing the corresponding values of slab temperature on the background temperature previously calculated. The third step was applying the diffusion equation to smooth the thermal structure and simulate conduction in the whole model.

3.2.2.1 *Background thermal structure*

Two models will be considered to calculate the temperature at depth for the background thermal structure.

For the purpose of simplicity, the first model assumes that the temperature varies linearly with depth, with no heat internal sources. Temperature was set to 0°C on the surface of the lithosphere and increased so it would be 1300°C at its bottom. This is reasonable because the produced heat within the oceanic lithosphere is negligible. For this work, the heat produced within the continental lithosphere was also considered negligible.

The second model considers the temperature to be the same throughout the medium, except for an adiabatic heat contribution, as Equation 3.5 illustrates (Stein and Wysession, 2009). This thermal configuration describes a convecting-mantle medium as it is assumed that self-compression occurs adiabatically (Stein and Wysession, 2009).

$$T(z) = (T_0 - 273.15) \exp \frac{\alpha g z}{C_p} \tag{3.5}$$

where T_0 is the potential temperature of the mantle on the surface at $z = 0$, $\alpha = 3.28^{-5}\mathrm{K}^{-1}$ is the thermal expansion coefficient, $g = 9.8$ m/s^2 is the gravity, and $C_p = 1250$ m$^2/Ks^2$ is the heat capacity. Equation 3.5 needs to be solved for T_0 as the temperature at the bottom of the model (at 660 km) will be set to be constant.

Both linear and adiabatic models were combined to calculate the background thermal structure. The profile was built with the minimum of both models, keeping the temperature at 1300°C at the Moho discontinuity. The results of such models will be presented on Section 3.2.2.2, together with the initial slab temperature model.

3.2.2.2 *Slab initial temperature model*

There are several kinematic temperature models used to calculate the thermal structures of subducting slabs. Examples of such models are those used by McKenzie (1969), Minear and Toksöz (1970) and King et al. (1990). For this work, I decided to use an analytical approach instead of a numerical one to calculate the initial temperature configuration for the simulation, as it provides a reasonable thermal structure and it is consistent with various numerical models.

From the equation of conservation of energy, one can calculate the temperature within a rectangular slab with Equation 3.6, which is a different form of Equation 3.3 (Zhong et al., 2007; McKenzie, 1969).

$$\rho C_p\left(\frac{\partial T}{\partial t}+v\cdot\nabla T\right)=\nabla(\kappa\nabla T)+H \tag{3.6}$$

where ρ is the density of the slab, C_p is the specific heat, T is the temperature, v is the velocity of the slab, κ is thermal conductivity, and H is the internal heat generation. The Equation 3.6 has four main parts. The first one is the $\partial T/\partial t$, which corresponds to the variation of temperature in time, where it can be considered null, as the model does not lose heat through time. The second part is the $v\cdot\nabla T$, which is the advective therm, associated to the plate motion. The third part is the $\nabla(\kappa\nabla T)$, which is the conduction therm, responsible for the diffusion of the heat within the slab. The fourth therm, H, is the rate of production of heat withing the slab, which can also be considered to be null as we are dealing with an oceanic lithosphere in subduction.

Assuming that the properties ρ, C_p and κ do not depend on the position, Equation 3.6 can be rewritten as Equation 3.7 for a two dimensional slab.

$$\rho C_p v\cdot\nabla T=\kappa\nabla^2 T\Rightarrow\rho C_p v\frac{\partial T}{\partial x}=\kappa\left(\frac{\partial^2 T}{\partial x^2}+\frac{\partial^2 T}{\partial y^2}\right) \tag{3.7}$$

Equation 3.7 has a series solution (Stein and Wysession, 2009) as follow:

$$T(x,y)=T_m\left[1+2\sum_{n=1}^{\infty}\frac{(-1)^n}{n\pi}\exp\frac{\beta_n x}{L}\sin\frac{n\pi y}{L}\right] \tag{3.8}$$

where T_m is the temperature of the surrounding mantle, L is the thickness of the slab, $\beta_n=\sqrt{(R^2+n^2\pi^2)}-R$, and $R=\rho C_p vL/(2\kappa)$ is the dimensionless Reynolds number, which corresponds to the rate at which the material heats up by conduction during the subduction.

There are a few generalizations that can be understood from Equation 3.8. The presence of a T_m indicates an uniform temperature mantle surrounding the slab; the slab is also penetrating the mantle with a uniform velocity; and the slab does not exchange mass with the mantle.

The temperature of the subducting slab T_S can then be written as the sum of the temperature defined by Equation 3.5 and an adiabatic contribution $dT=T(z)-T_0$, as Equation 3.9 shows.

$$T_S=T(x,y)+dT \tag{3.9}$$

Once the temperature of the background and the temperature of the subducting slab were defined, I applied the diffusion equation (Equation 3.10) for a period of 10 Myr to simulate the heat diffusion of the slab and the mantle, making the initial thermal structure more geologically reasonable. Additionally, this diffusion step is important to deal with any numerical artifacts that could have been generated.

$$\frac{\partial T}{\partial t} = \alpha \nabla^2 T \tag{3.10}$$

The initial thermal structure is shown on Figure 3.7, where Figure 3.7a shows the thermal structure before the 2D diffusion and Figure 3.7b shows the temperature after 10 Myr of diffusion. Figure 3.7 is shown here as an illustration, as different geometries and velocities had different initial thermal configurations.

3.2.3 Rheology model

In the present visco-plastic formulation, the effective viscosity η follows the formulation described by Solomatov and Moresi (2000), combining the Frank-Kamenetskii approximation for the viscous deformation and the Byerlee Law for plasticity.

The viscosity was considered to vary exponentially as a function of the temperature T and the compositional factor C, which is the Frank-Kamenetskii approximation (see Equation 3.11). This relation for the viscosity was used instead the Arrhenius relationship because they are essentially identical. Regardless of this choice, both the Arrhenius relationship and the Equation 3.11 consider the mantle to be a variable viscosity fluid for a steady state ductile creep, as it is usually considered for convection problems in geodynamics (Solomatov and Moresi, 2000).

$$\eta_{visc}(T, C) = C\eta_r b^* \exp -\gamma T \tag{3.11}$$

where η_r is the reference viscosity, b^* and $\gamma = E_a/RT_b^2$ are constants where, which in turn, E_a is the activation energy, R is the gas constant, and T_b is the basal temperature.

The Byerlee Law (Byerlee, 1968) is used to determine the rupture tension:

$$\tau_{yield} = c_0 + \mu\rho g z \tag{3.12}$$

where $c_0 = 22$ MPa is internal cohesion (Petersen et al., 2010), $\mu = 0.588$ is the friction coefficient (Petersen et al., 2010), and z is depth.

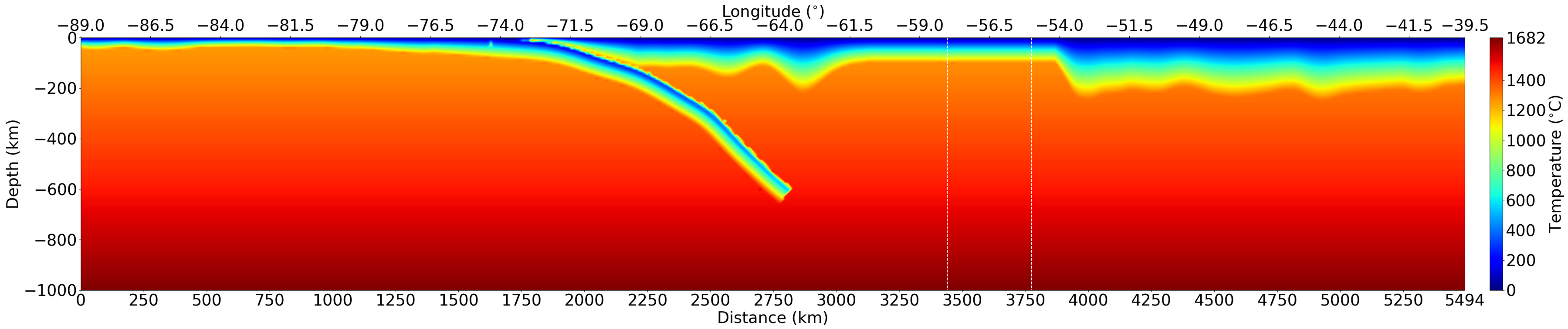

(a) Thermal model without 10 Myr diffusion.

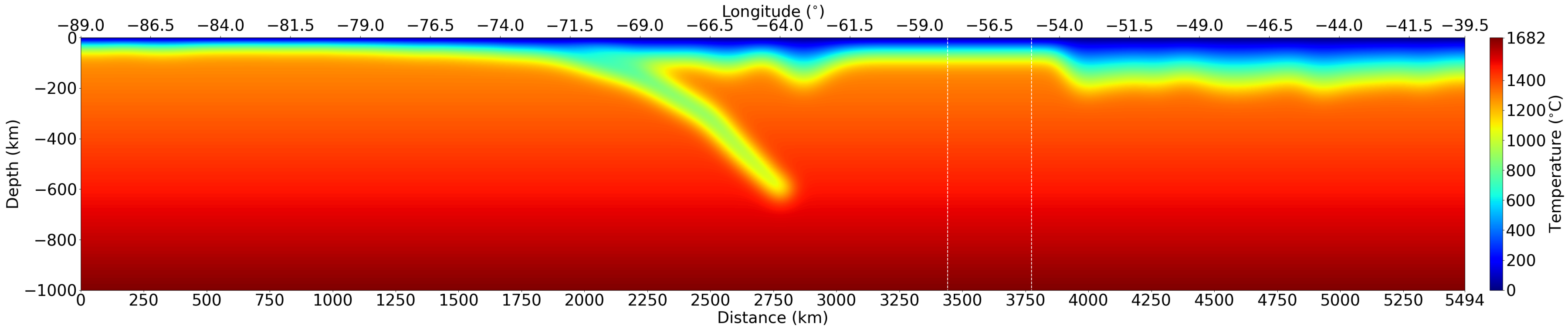

(b) Thermal model with 10 Myr diffusion.

Figure 3.7: Initial thermal model for the complete Slab2 model at the latitude 18.00°S. The slab velocity was set to 50 mm/yr.

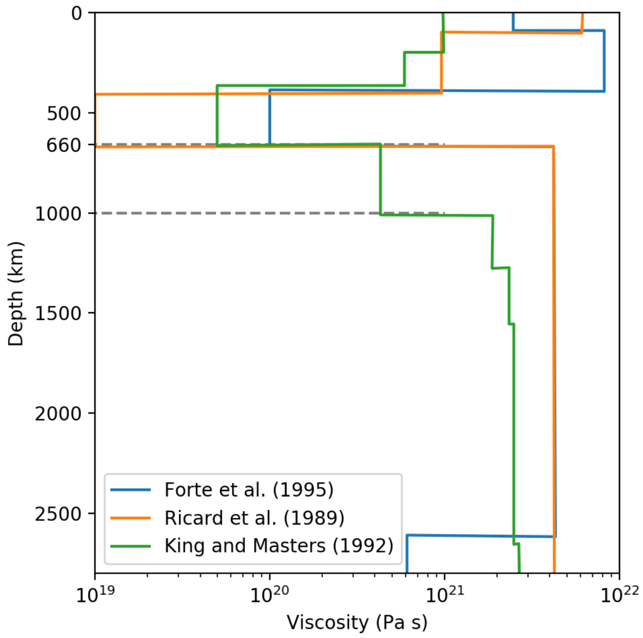

Figure 3.8: Relative viscosity profiles from Forte et al. (1991); Ricard et al. (1989); King and Masters (1992).

The effective viscosity for the non-linear deformation induced by plasticity is given by the following expression Solomatov and Moresi (2000):

$$\eta_{plast} = \frac{\tau_{yield}}{J_2} \tag{3.13}$$

where J_2 is the second invariant of the deviatoric stress tensor.

The effective viscosity η is therefore calculated as the minimum between η_{visc} and η_{plast}:

$$\eta = \min\left(\eta_{visc}, \eta_{plast}\right). \tag{3.14}$$

Additionally, for the lower mantle, I adopted an increase in viscosity of 20 times relative to the upper mantle. This increase is compatible with previous estimations of viscosity increase at 660 km due to phase transformations in the mantle (Figure 3.8 shows how the viscosity of the lower mantle changes for three different studies from Forte et al. (1991), Ricard et al. (1989) and King and Masters (1992)).

3.2.4 Velocity field

Because the model was not a closed box, material flowed in and out through its east and west borders. Therefore, the velocity field represents the speed with which the material enters and leaves the model domain for the whole simulation.

I used two different velocity models for the velocity field in this project. I modified these models for each simulation and they were used for specific setups and objectives. The choice of the velocity models will be discussed in Chapters 4 and 5 for each simulation.

The first velocity model pushed the Nazca plate with a constant velocity towards the South American plate. In this scenario, the subducting slab slid under the lubricant layer and moved into the mantle. The second velocity model let the slip velocities free all around the model and applied a eastward normal velocity that pushed the lower mantle instead with a constant velocity, decreasing it linearly until zero at the depth of 300 km.

First velocity model (FVM). On the first velocity model, the slip velocity was set to be fixed and null only for the top border of the model. For the other borders, the velocity was free. This strategy meant to hold the South American plate in place and push the Nazca plate from west to east, as well as some of the lubricant unit. Normal velocities on all borders were fixed, such that they were null on the top and bottom of the model, but they were different on the sides.

On the west border, the normal velocity was constant and positive until the LAB depth, with the magnitude of the velocity v_x of the Nazca plate relative to the South American plate. On the east, the velocity was constant and positive for an interval right above the 660 km interface; it also had a magnitude v_x. To smooth the velocity transition from null to non-null, I used Equation 3.15, the error function (see Figure 3.9a).

$$erf(x) = \frac{2}{\sqrt{\pi}} \int_0^x e^{-t^2} dt \tag{3.15}$$

The velocity respected the equation of conservation of mass (Equation 3.1). Therefore, the mass flowing in through the west border was compensated by the same mass flowing out at the east border. Because the model was purposely made to be wide, the geodynamic effects of the inflow and outflow should be negligible far away from the sides.

Second velocity model (SVM). For the second velocity model, I set the slip velocity free on all borders of the model, but I also made simulations with the static continent, as in the first velocity model. The normal velocity on the top and bottom were also null, but the velocities on the sides were different. While the first model considered the velocity of the slab in respect to the continent, this velocity model considered the velocity of the lower mantle in respect to the continent. Thus, the velocity was zero until 300 km deep, increased linearly until the 660 km, and was constant in the lower mantle, from 660 to

1000 km deep, as Figure 3.9b illustrates.

3.2.5 Isostasy and flexure

To calculate the topography for the simulations at distinct simulation time steps, I used Equation 3.16 to account for thermal expansivity (Sacek, 2017).

$$S_t = \int_{z_0}^{z_1} \Delta\rho g dz \tag{3.16}$$

where $\Delta\rho = \rho_1(1-\alpha T_1) - \rho_0(1-\alpha T_0)$, ρ_i and T_i are the density and the temperature for a given point at an instant i, α is the expansivity coefficient, and z_0 and z_1 are depth value at the surface and at the bottom of the model, respectively.

To calculate the subsidence due to flexure of the lithosphere, I also solved the flexure equation shown on Equation 3.17 (Fowler, 2002).

$$D\frac{dw^4}{dx^4} + \Delta\rho g w = p(x) \tag{3.17}$$

where D is the flexural rigidity of the plate, w is the subsidence, $\Delta\rho$ is the density difference between the slab and its filling content, g is the gravity acceleration, and $p(x)$ is the load. The flexural rigidity of the plate D is defined on Equation 3.18.

$$D = \frac{ET_e^3}{12(1-\nu^2)} \tag{3.18}$$

where E is the elasticity modulus, T_e is the effective elastic thickness, and ν is the Poisson coefficient.

The purpose is to use both Equations 3.16 and 3.17 to calculate the the topography for a simulation with mostly thermal subsidence and for any other simulation. Subtracting the the calculated thermal subsidence from other simulation, the result will be a topography only due to mantle convection, dynamic topography.

3.2.6 Fixed parameters

The parameters that were fixed (constants) and used for this project are presented on Table 3.1, as well as their units and values. The values come from Sacek (2017), Turcotte and Schubert (2002) and Gerya (2010).

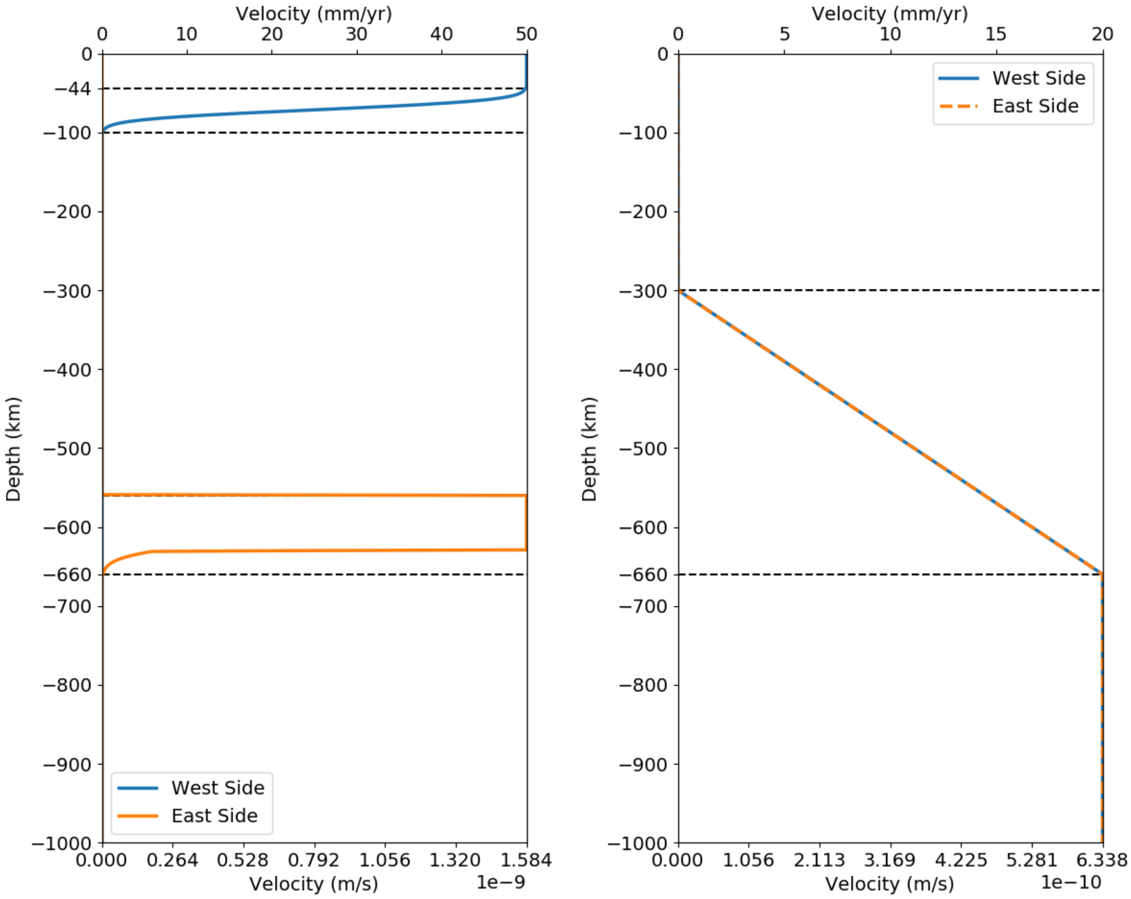

(a) First velocity scenario. Velocity at the east and west boundaries of the model showing how velocity was set using Equation 3.15.

(b) Second velocity scenario. Velocity at the east and west boundaries of the model showing linear variation of the velocity for the second scenario.

Figure 3.9: Velocity profiles for the first scenario (left) and the second scenario (right) showing how velocity was set as a function of depth. The shown velocities are only for the sides of the model.

Table 3.1 - Fixed parameters.

	Parameters	Description	Value
Mantle convection	Myr	Million years	1.0×10^{6} years
	α	Thermal expansivity	$3.28 \times 10^{-5}\,{}^{\circ}\mathrm{C}^{-1}$
	κ	Thermal diffusivity	1.0×10^{-6} m^{2}s
	g	Gravity acceleration	9.8 m/s^2
	C_p	Specific heat	1250 J/K
	η_r	Reference viscosity	1.0×10^{19} Pa s
	E_a	Activation energy	240 kJ/mol
	R	Gas constant	8.31 J/mol K
	T_b	Basal temperature	1682°C
	b^*	Proportionality constant	1.0×10^{7}
Flexure and isostasy	E	Young's modulus	1.0×10^{11} N/m^2
	ν	Poisson's ration	0.25
	Te	Effective elastic thickness	70km

Chapter 4

Nazca plate buoyancy

This project was divided into two different parts. The first part was the study of how the buoyancy of the Nazca plate could be affected by the initial parameters that were used and will be presented on this chapter. The second part was the study of how the subduction of the Nazca plate could affect the evolution of the topography of the South American plate through mantle convection; this part will be presented on Chapter 5.

4.1 Numerical setup

For this buoyancy study, I used the MD3D numerical code to simulate mantle convection under the Nazca and the South American plates. The geometry of the LITHO1.0 and the Slab2 models were used (Section 3.2.1) for the simulations. Because I wanted to observe how the slab would change its trajectory without penetrating the lower mantle, the subducting slab was cut to a depth of 450 km. The two-dimensional models were profiles at latitude 18.00°S, from longitude 89.00°W to 39.50°W, and with depth ranging from 0, at the surface, to 1000 km, at the bottom.

In respect to the number of elements in the grid, the models were made with 551 nodes in the longitudinal direction, and 101 nodes in the depth direction. Therefore, all the simulations had $(551, 101)$ points or $(500, 100)$ elements. This discretization was used because of the approximation I adopted for the Cartesian grid, where 1° of longitude corresponded to 111.0 km. This approximation resulted in a grid with elements with an area of around 100 km^2, where each element had a height of 10.00 km and a thickness of 9.99 km.

The simulations were made with different oceanic crust densities, oceanic crust thicknesses, oceanic lithospheric mantle thicknesses, and slab velocities. The tested values of oceanic crust were 2800, 2950 and 3100 kg/m^3, and they were chosen around the mean global value of 2950 kg/m^3 (Turcotte and Schubert, 2002). The chosen values for the oceanic lithospheric mantle thicknesses were picked around the thickness of the Slab2 model of 85.5 km, and were 70.0, 75.0, 80.0, 85.5 and 90.0 km. The values for the oceanic crust thicknesses were picked around the global mean of 6 km (Turcotte and Schubert, 2002), and were 5, 6, 7, 8 and 9 km. The values of the velocity for the subducting slab were imposed as 50 and 70 mm/yr relative to the South America plate. These velocities were estimated from typical Nazca plate relative velocity values, such as those found in Schellart et al. (2007), Norabuena et al. (1999) and Angermann et al. (1999).

I simulated 5 Myr of geodynamic evolution so it would be possible to study the changes within a period comparable to the age that is usually associated to the Pantanal basin, around 2.5 Myr. These simulations assessed how the deflection of the Nazca plate changed according to each combination of these parameters.

4.2 Results

For this study, I first chose two different slab velocities of 50 and 70 mm/yr. For each velocity, I divided the simulations in three groups with a different density each. For each oceanic crust density, a combination of oceanic lithospheric mantle thickness and oceanic crust thickness was used, which resulted in twenty five simulations. The chosen values of density were 2800, 2950 and 3100 kg/m^3, which are utilized in numerical studies (Gerya, 2010). The thicknesses were also picked around the global mean (Turcotte and Schubert, 2002).

For a velocity of 50 mm/yr, the results for each oceanic crust density are shown on figures 4.1a, 4.1b and 4.1c.

It is possible to notice from figures 4.1a, 4.1b and 4.1c that, for a simulation time of about 5.0 Myr, the mean subduction angle difference between the simulated slab and the Slab2 doesn't go beyond the interval of ±17 degrees. A positive angle in the correlation graphs from Figure 4.1 represents a slab that deflected upwards in respect to the Slab2 model. When the angle is negative, the simulated slab deflected downwards.

It is noticeable on Figure 4.1 that until 2.5 Myr of simulation, the dip of the subducting

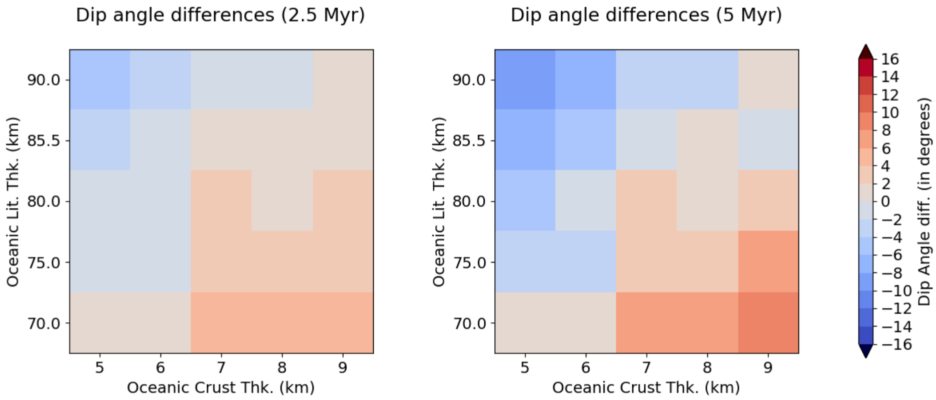

(a) Results for $\rho_{oc} = 2800$ kg/m^3. Simulation time is $\sim$ 2.5 Myr (on the left), and $\sim$ 5.0 Myr (on the right).

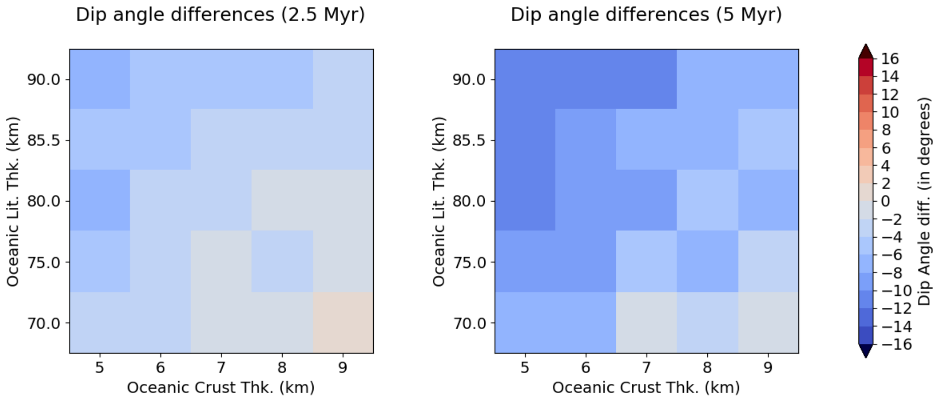

(b) Results for $\rho_{oc} = 2950$ kg/m^3. Simulation time is $\sim$ 2.5 Myr (on the left), and $\sim$ 5.0 Myr (on the right).

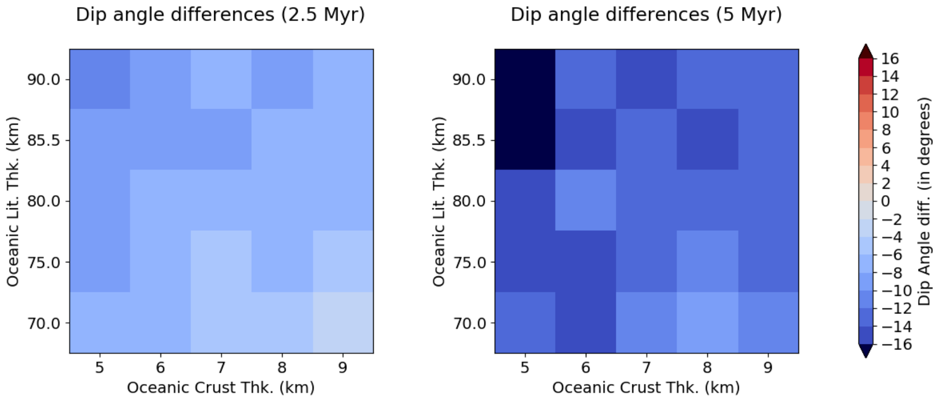

(c) Results for $\rho_{oc} = 3100$ kg/m^3. Simulation time is $\sim$ 2.5 Myr (on the left), and $\sim$ 5.0 Myr (on the right).

Figure 4.1: Mean dip angle difference between the Slab2 model and the simulated subducting slab with an imposed velocity of 50 mm/yr. Correlations are shown for each oceanic crust density ρ_{oc}.

slab behaves on a clear fashion for the proposed combinations of oceanic lithospheric mantle and oceanic crust thicknesses. This behaviour also evolves as the oceanic crust density increased. On Figure 4.1a, where the oceanic lithospheric mantle is relatively thicker than the oceanic crust, the slab deflected downwards, while the oceanic lithospheric mantle with a thicker oceanic crust deflected upwards. Once the density was increase from 2800 to 2950 kg/m^3 (Figure 4.1b), only the smallest oceanic lithospheric mantle thickness combined with the biggest oceanic crust thickness yielded an upward deflection in 2.5 Myr. From that point, when I utilized the oceanic crust density of 3100 kg/m^3, no upward deflection was observed for the simulated slab in respect to the Slab2 model.

At 5.0 Myr, all the dip angles increased and upward deflection of the slab was only observable on the simulations where the oceanic crust density was 2800 kg/m^3. Yet, by that time step, the correlations trend still behaved the same as in the results at 2.5 Myr.

The difference between the mean subduction angle of the Slab2 model and the simulated slab for the velocity of 70 mm/yr are presented on figures 4.2a, 4.2b, and 4.2c.

The trend of the difference of the dip angles for a velocity of 70 mm/yr followed roughly the trend of the simulations with the velocity of 50 mm/yr. It was clear that increasing the oceanic crust thickness, for the same oceanic lithospheric mantle thickness, caused the slab to be relatively more buoyant for the simulations until 2.5 Myr.

At 5.0 Myr, it was possible to observe that the slabs with a relatively smaller thickness bent and deflected down more. The amplitude of the dip difference was also inversely proportional to the oceanic crust thickness. Thus, a relatively thinner slab with a relatively thinner oceanic crust will deflect more.

Beyond the difference between the mean slab dip angles, the simulated Nazca plate moved about 40 km eastward, as Figure 4.3 shows for the simulation with and oceanic lithospheric mantle 70 km thick and an oceanic crust with a thickness of 5 km. Figures 4.3a and 4.3b show the position of the surface of the plate, the velocity field, and the logarithm of the viscosity η at two different times of the simulation. The displacement was the consequence of the initial geometry and compositional parameters. To ease the slip of the Nazca plate under the South American plate, a lubricant layer of 60 km was put between the oceanic lithosphere and the continental lithosphere. This lubricant layer had an initial viscosity 1000 times smaller than the viscosity of the asthenospheric mantle. The relatively soft lubricant layer deformed because of the subducting lithosphere, as it is

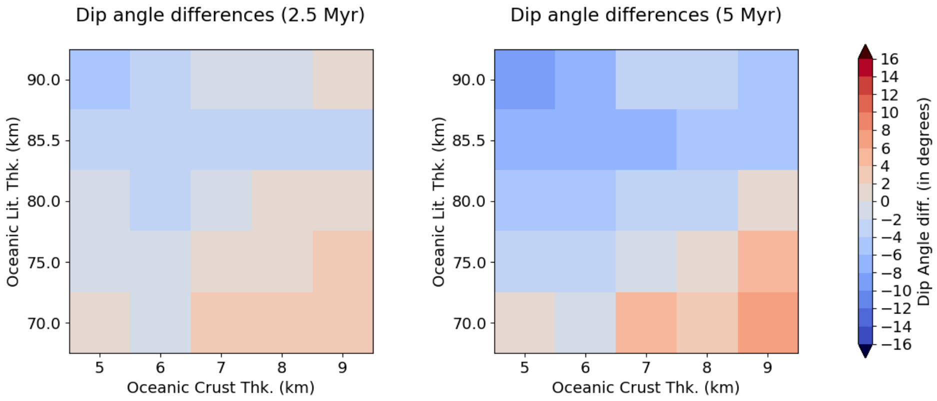

(a) Results for $\rho_{oc} = 2800$ kg/m^3. Simulation time is ~ 2.5 Myr (on the left), and ~ 5.0 Myr (on the right).

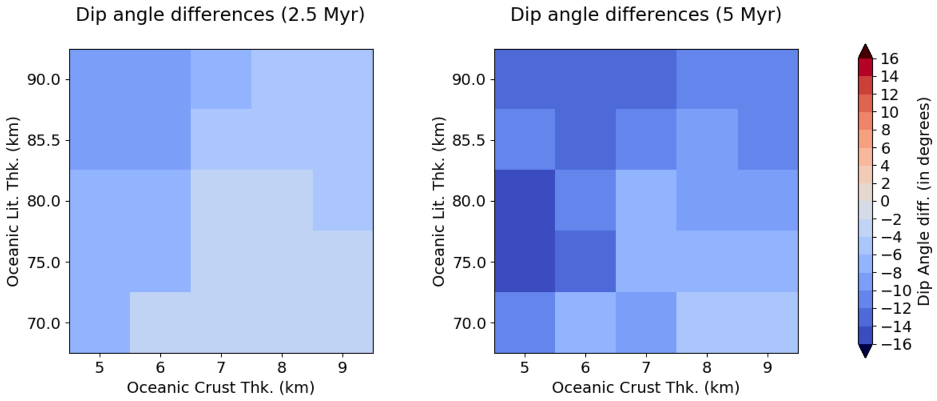

(b) Results for $\rho_{oc} = 2950$ kg/m^3. Simulation time is ~ 2.5 Myr (on the left), and ~ 5.0 Myr (on the right).

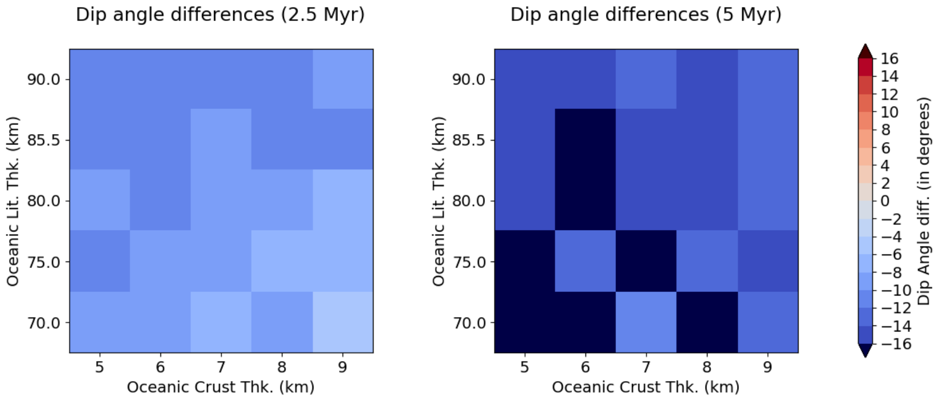

(c) Results for $\rho_{oc} = 3100$ kg/m^3. Simulation time is ~ 2.5 Myr (on the left), and ~ 5.0 Myr (on the right).

Figure 4.2: Mean dip angle difference between the Slab2 model and the simulated subducting slab with an imposed velocity of 70 mm/yr. Correlations are shown for each oceanic crust density ρ_{oc}.

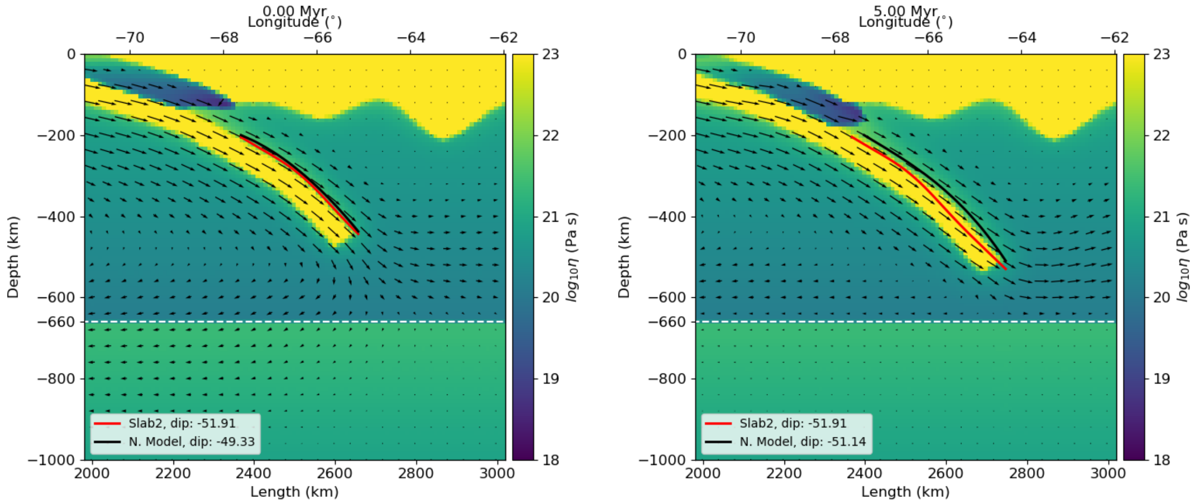

(a) Viscosity field at the beginning of the simulation. Here it is possible to notice the difference between the mean Slab2 dip and the mean calculated slab dip.

(b) Viscosity field at 5 My showing the lubricant layer compression and deformation.

Figure 4.3: Viscosity profiles at the beginning and at the end of the simulation, 5 My, for an oceanic lithospheric mantle 70 km thick and an oceanic crust 5 km thick. The arrows come from the velocity field, but are here only to represent the relative flow direction. The simulated Nazca place surface is shown in black and the Slab2 surface is shown in red.

possible to see on figures 4.3a and 4.3b.

From all the simulations that were made, it was possible to define that the Nazca plate will deflect less in a period of 5.0 Myr for a density of 2800 kg/m^3. Nevertheless, for periods of less than 2.5 Myr, densities around the global mean of 2950 kg/m^3 are also reasonable. From all the simulations, the values that resulted in the smallest deflection from the Slab2 model was the simulation for an oceanic crust with a density of 2800 kg/m^3 and thickness of 8 km, and an oceanic lithospheric mantle thickness of 80 km and imposed velocity 50 mm/yr, which deflected 0.227 degrees upwards.

4.3 Discussion

The first aspect of the simulations that was noticed was that, for both 50 and 70 mm/yr slab velocities, the subducting Nazca plate behaved more or less as expected. The expectation was that the resulting density of the subducting slab would influence its own buoyancy and, therefore, trajectory. For a surrounding asthenospheric mantle with a density of 3300 kg/m^3, the first expectation was to consider that any slab with a lesser density than the asthenospheric mantle would deflect upwards because of the buoyant forces.

The density was not the only parameter that affected the slab deflection. Other parameters such as mantle flow configuration and flexural rigidity of the subducting slab must be considered when studying the slab buoyancy. The slab bending resistance, the flexural rigidity, is proportionally related to the cube of its elastic thickness (Equation 3.18). This can be observed on the simulations where the slab velocity is 70 mm/yr, particularly on Figure 4.2c. For a oceanic crust density of 3100 kg/m^3, the dip angle difference is higher when both the oceanic lithospheric mantle and the oceanic crust are thinner.

Chapter 5

Full length simulations

The full length simulations study was the second part of this project, where I used the complete Slab2 model and simulated for longer periods, more than 50 Myr. There were two different approaches for this second part. The first approach was similar to the one presented in Chapter 4, where the Nazca plate was pushed towards the fixed continent with a constant velocity, named the forced slab approach. The second approach was to let the Nazca plate move by itself without any initial velocity, the free slab approach. Both approaches will be discussed thoroughly in the next sections.

5.1 *Numerical setup*

The mesh-grid for each simulation had $(500, 100)$ elements, started at 89.00°W and ended at 39.50°W. The latitude was 18.00°S and the models were 1000 km thick. The grid was identical to the one used in the buoyancy study (see Section 4.1).

Regarding the velocity field, while Chapter 4 used the relative velocity between the subducting plate and the South America plate (first velocity model, see Section 3.2.4), this part of the project considered the same relative velocity, but also incorporated the relative velocity between the Nazca plate and the lower mantle (second velocity model, see Section 3.2.4).

5.2 *Results*

Before simulating with any external velocity, I made a control simulation to study how thermal diffusion influenced the overall evolution of the model through time. To do this, I simulated a scenario using the default Slab2 thickness, as well as the LITHO1.0 geometry

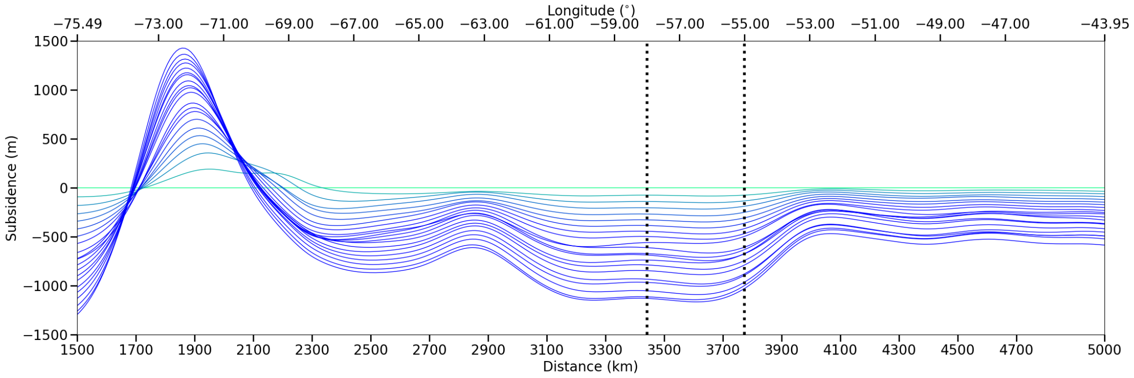

Figure 5.1: Isostatic topography evolution from thermal subsidence. The curves show the evolution from 0 (light green) to 100 Myr (blue) at intervals of 5 Myr. The vertical dashed lines represent the approximate longitudinal limits of the Pantanal basin.

saturated at 100 km at the continental region.

To solve the initial thermal structure of the slab, I used the velocity of 50 mm/yr for the advection term (Equation 3.8). The density of the continental crust was set to 2750 kg/m^3, and the oceanic crust was set to the global mean of 2950 kg/m^3. The density of the lithospheric mantle was set to be the same as the one from the asthenospheric mantle, 3300 kg/m^3, and the lower mantle density was set to be 3700 kg/m^3.

The results for this simulation were used to generate an evolution history of the thermal subsidence S_t shown on Figure 5.1. This topography was calculated using Equations 3.16 and 3.17 from Section 3.2.5.

The thermal structure for the studied scenario is shown on Figures 5.2a and 5.2b at the beginning and at the end of the numerical simulation, respectively. They suggest that the thermal subsidence had an amplitude of up to 1000 m for a period of 100 Myr, with a mean subsidence rate of about 10 m/Myr. This occurs because the initial thermal condition is not at the dynamic equilibrium, and thermal diffusion mainly in the lithosphere induces its secular cooling. These figures show the evolution of a Rayleigh-Taylor instability scenario, where the convection develops from the small disturbances in the model (Gerya, 2010).

I chose to run this simulation for 100 Myr only to have a big enough time interval to use it together with the upcoming simulations. Because all these simulations were made until the subducting slab crossed the east limit of the Pantanal basin and because the slab velocity changed depending on the initial conditions, the models took between 30 to 80 Myr to be completed.

The high amplitudes of the velocity vectors that are observed are due to flow inside the

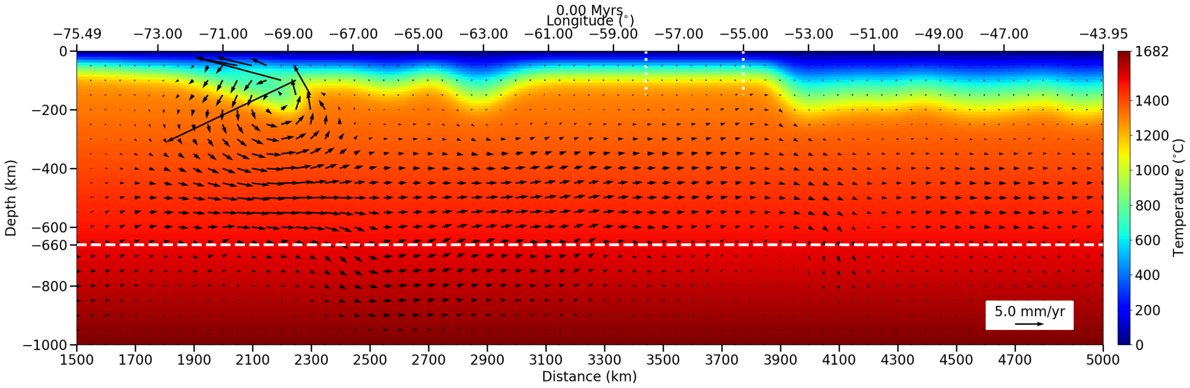

(a) Temperature field at the beginning of the simulation.

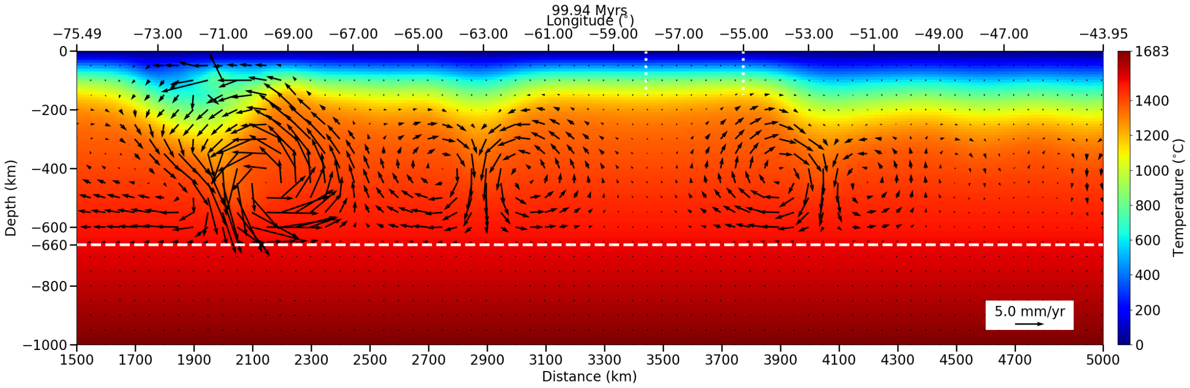

(b) Temperature field at the end of the simulation, around 100 Myr.

Figure 5.2: Thermal structure at instants 0 and 100 Myr of the simulation. Dotted vertical white lines are the approximate lateral boundaries of the active Pantanal basin.

low viscosity lubricant layer, $10^{-3}\eta_r$, and consequent uncoupling of the oceanic lithosphere. The Nazca plate does not sink because it is attached to the top of the model due to the null velocity boundary conditions. This study will focus on the areas that are within the interior of the continent, from around 65.0°W to 45.0°W.

5.2.1 *Forced slab approach*

The following approach for the numerical study was to continue what was developed in Chapter 4. Therefore I made two distinct simulations using the FVM from Section 3.2.4. The first simulation modeled an oceanic lithosphere with a velocity of 50 mm/yr relative to the continent for 50 Myr and with a lower mantle density of 3300 kg/m^3. In the second simulation, the lower mantle density was changed to 3700 kg/m^3. The initial parameters for this study were very similar to those used in the buoyancy study. The only difference was the initial geometry for the subducting slab, which in this case was not cut. The details of these two simulations are discussed in Appendix A, as well as their results.

However, these group of scenarios presented some unrealistic behavior regarding the thickening of the oceanic lithosphere. It was unrealistic because the horizontal compression, induced by the coupling between the oceanic and continental lithosphere, formed an oceanic lithosphere with more than 200 km thick. One consequence of this behavior is the incipient penetration of the slab into the mantle. Therefore, these scenarios are just briefly described in this project.

The thickening of the oceanic lithosphere, the strong coupling between oceanic and continental slabs, the relative small penetration of the subducting plate were the reasons I changed the approach to another model setup, described in the following section.

5.2.2 *Free slab approach*

The free slab approach consisted in letting the tangential velocity for the nodes at the surface free for the oceanic lithosphere. In these scenarios, the movement of the lithosphere is determined internally by the conservation equations, representing a natural convection instead of imposed velocities at the top boundary. To avoid problems with return flow (Gurnis and Hager, 1988), I imposed a velocity for the lower mantle relative to the continental lithosphere. I tested two velocities for the lower mantle, assuming an eastward movement of 10 and 20 mm/yr relative to the continent, evaluating their effects on the overall evolution of the simulations. I also defined a ridge-like structure on the west side of the model with a low viscosity to allow free movement of the oceanic lithosphere. Additionally, no velocity was defined for the oceanic lithosphere, which would sink under its own weight (slab pull).

Table 5.1 shows the common parameters that were used to run this set of simulations, as well as their values. From now on, the only parameters that are mentioned to describe each simulation are those that set them apart from each other. These parameters are the density of the lower mantle, ρ_{LM}, the density of the oceanic lithospheric mantle, ρ_{OL}; the compositional factor of the oceanic crust and lithospheric mantle, C_{OC} and C_{OL}, respectively; and the velocity of the lower mantle relative to the South American plate, v_{LM}. It is also indicated if the simulation has a stationary continental slab (SCS), not being allowed to move sideways, or if it is a free continental slab (FCS), being able to move and compress in the longitudinal direction.

Table 5.1 - Common simulation parameters used for simulations presented in section 5.2.2.

Parameters	Values
Length	5494.5 km/49.5°
Thickness	1000.0 km
Continental crust density	$\rho_{CC} = 2750$ kg/m^3
Oceanic crust density	$\rho_{OC} = 2950$ kg/m^3
Upper lubricant unit density	$\rho_{UL} = 2750$ kg/m^3
Continental lithosphere density	$\rho_{CL} = 3300$ kg/m^3
Lower lubricant unit density	$\rho_{LL} = 3200$ kg/m^3
Mantle density	$\rho_M = 3300$ kg/m^3
Density below oceanic ridge	$\rho_R = 3200$ kg/m^3
Continental crust compositional factor	$C_{CC} = 1000$
Oceanic crust compositional factor	$C_{OC} = 1000$
Upper lubricant unit compositional factor	$C_{UL} = 0.001$
Continental lithosphere compositional factor	$C_{CL} = 1000$
Oceanic lithosphere compositional factor	$C_{OL} = 1000$
Lower lubricant unit compositional factor	$C_{LL} = 0.001$
Mantle compositional factor	$C_M = 1$
Compositional factor below ridge	$C_R = 0.001$

In the present study, I analyzed how the Nazca plate trajectory evolved through time inside the mantle and evaluated the conditions for penetration in the lower mantle, as well as the longitudinal extent of the subducting plate under the South America lithosphere (Fukao and Obayashi, 2013). I analysed the simulations until the point where the subducting slab crossed the region corresponding to the Pantanal basin. Nevertheless, all the simulations ran for 100 Myr.

I was able to test many scenarios, which were valuable resources to understand the influence of some parameters on the simulations. The first parameter was the velocity boundary condition on the surface of the continental plate. On Section B.0.1 in the Appendix B, I showed through a series of simulations how the continent is deformed accommodating the stresses due to the subducting plate. This deformation made these models unusable for the current study where I used the surface as my reference to calculate the dynamic topography. For the following simulations, I used a stationary South American plate (Section B.0.2 on Appendix B).

Due to the great number of numerical experiments presented here, for clarity, in the present chapter I focused only on four representative scenarios:

- M1: $\rho_{OL} = 3300$ kg/m^3, $\rho_{LM} = 3700$ kg/m^3, $v_{LM} = 20$ mm/year
- M2: $\rho_{OL} = 3300$ kg/m^3, $\rho_{LM} = 3300$ kg/m^3, $v_{LM} = 20$ mm/year
- M3: $\rho_{OL} = 3400$ kg/m^3, $\rho_{LM} = 3700$ kg/m^3, $v_{LM} = 20$ mm/year
- M4: $\rho_{OL} = 3400$ kg/m^3, $\rho_{LM} = 3300$ kg/m^3, $v_{LM} = 20$ mm/year

The other numerical experiments are shown in the Appendix B.

For model M1, due to the large density contrast between the subducting slab and the lower mantle (reference $\Delta\rho = 400$ kg/m^3), the slab flattens above the 660-km interface. It is possible to observe that the angle of subduction becomes shallower through time and the coupling between the slab and the continental lithosphere induces partial deformation in the oceanic lithosphere (Figures 5.3 and 5.4). Concomitantly, the cooling of the subducting slab induces the increase of its effective density, accentuating the subsidence over time for the overlying continental slab (Figure 5.5). The maximum subsidence in the foreland basins (between longitude -63° and -59°) is nearly 500 m, with a decreasing amplitude to the interior of the continent, reaching a magnitude of 300 m in the Pantanal basin, compatible with the results obtained by Flament et al. (2015). It is important to highlight that the subsidence obtained here are based on the air loaded model (see Equation 3.16) and if the surface depressions are filled by sedimentary layers, the subsidence can be amplified by nearly 3 times, depending on the density of the sedimentary package.

For model M2, the reference density of the lower mantle was assumed to be the same of the upper mantle (3300 kg/m^3) but I maintained the viscosity contrast of 20 times as previously described.

This difference in viscosity is not enough to avoid the penetration of the slab into the lower mantle (Figures 5.6 and 5.7). Due to the motion of the lower mantle relative to the continental lithosphere combined with the gravitational forces pulling the cold oceanic lithosphere, it is possible to observe a slab break-off (Figure 5.6). In this situation, the replacement of the hot lower mantle by the cold lithosphere (Figure 5.7) amplifies the negative dynamic topography at the surface (Figure 5.8), reaching more than 750 m of air-loaded subsidence, that migrates progressively eastward.

The partial stretching of the oceanic lithosphere on both models M1 and M2 was observed to be caused by the buoyancy of the oceanic lithosphere, which stayed coupled with the overlying continental lithosphere. Because the effective density of the subducting slab $\rho_{OL,E} = \rho_{OL}(1-\alpha T)$ is not much greater than the effective density of the surrounding mantle, the slab sinks relatively slowly and it is dragged by the increasing deep flow. One possible solution for this problem is to increase the ρ_{OL} to 3400 kg/m^3 (models M3 and M4).

The next simulations adopted the new density for the oceanic lithosphere (models M3 and M4). The resulting simulations presented a much faster subduction with less stretching, of reasonably more constant thickness throughout the simulation (Figures 5.9-5.12). Similarly to models M1 and M2, in model M3, the high density of the lower mantle (3700 kg/m^3) impeded the penetration of the subducting slab, while in model M4 the subducting slab crossed the 660 km interface.

Despite being faster and retaining the thickness of the subducting lithosphere, the results with these conditions presented a very high subsidence across all continental area, reaching more than 2000 m of air-loaded subsidence. These unrealistic vertical movement of the continent interior indicate that the reference density for the oceanic lithospheric mantle of 3400 kg/m^3 is too high.

Additionally, these experiments with free slab can mimic the behavior of a temporal variation in subduction velocity, as observed by Norabuena et al. (1999). In all our nu-

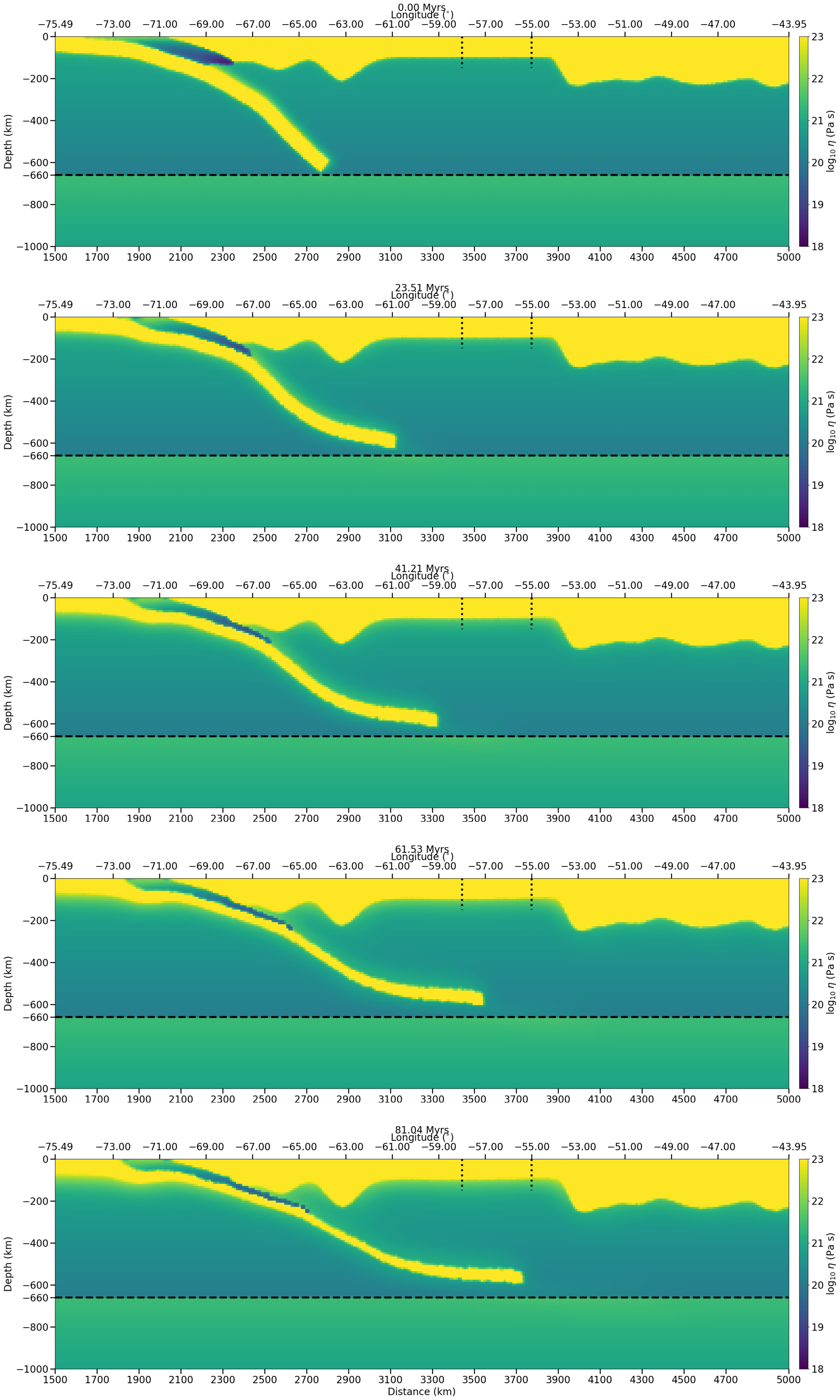

Figure 5.3: Viscosity evolution for model M1.

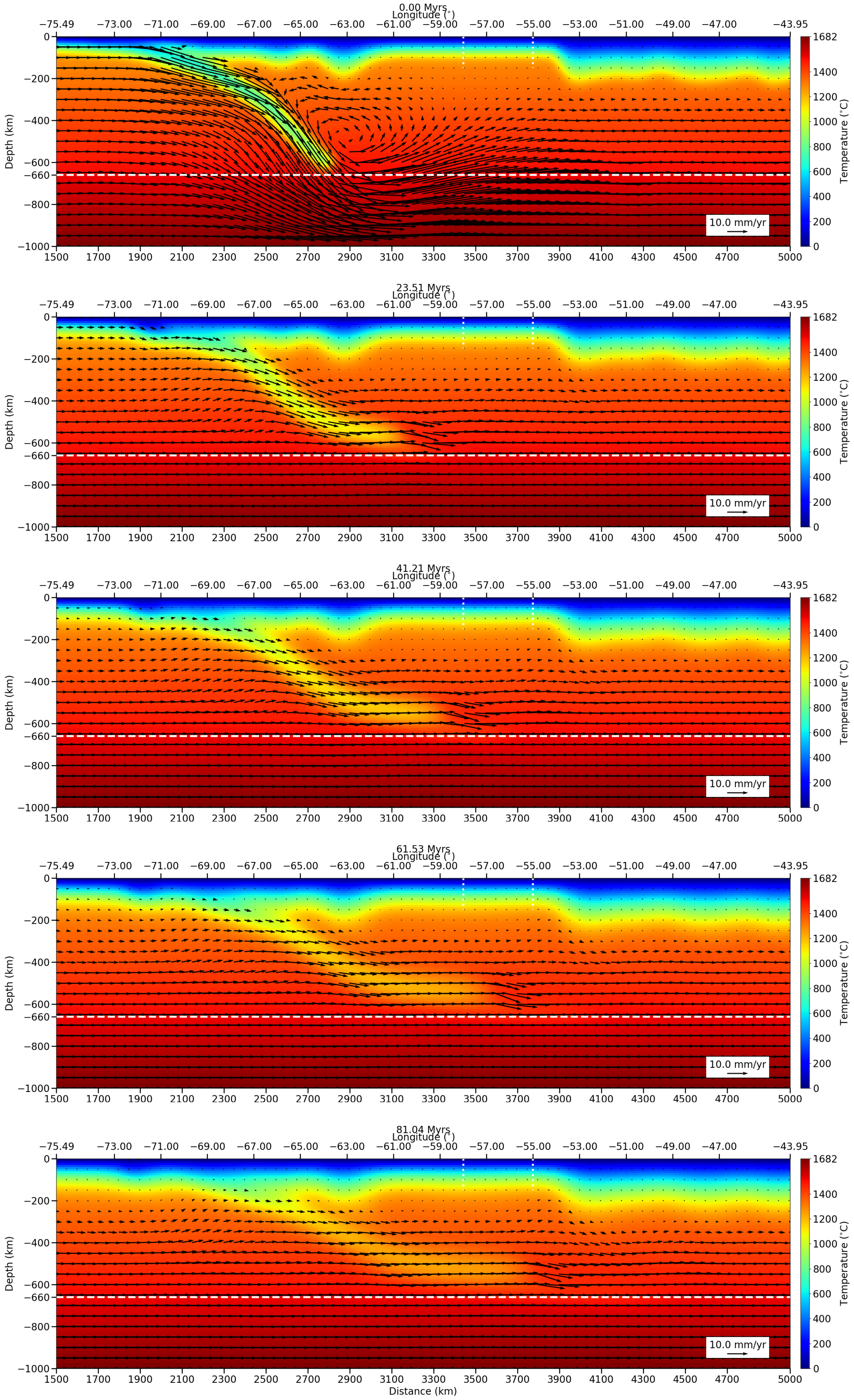

Figure 5.4: Temperature and velocity field through time for model M1.

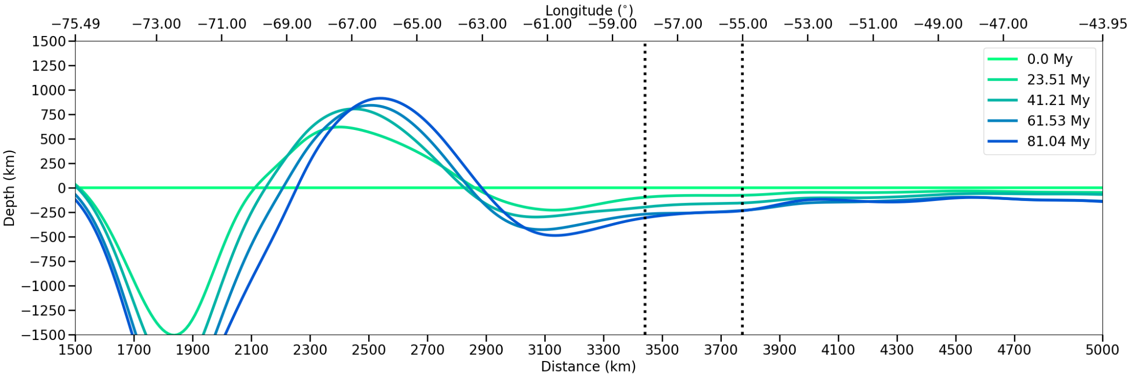

Figure 5.5: Dynamic topography evolution for the model M1.

merical experiments, the subduction velocity decreases monotonically through time as the plate starts to interact with the lower mantle.

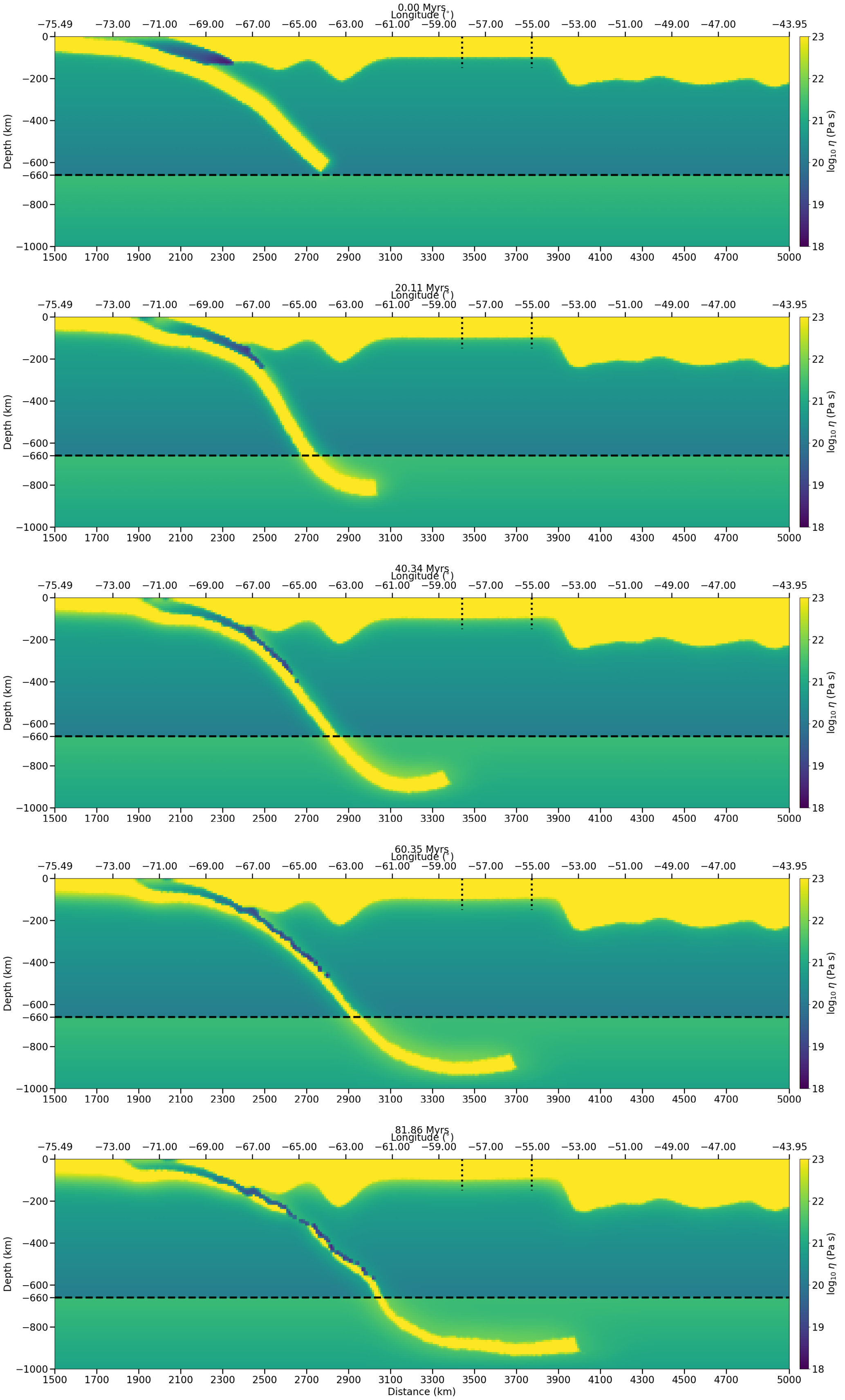

Figure 5.6: Viscosity evolution for model M2.

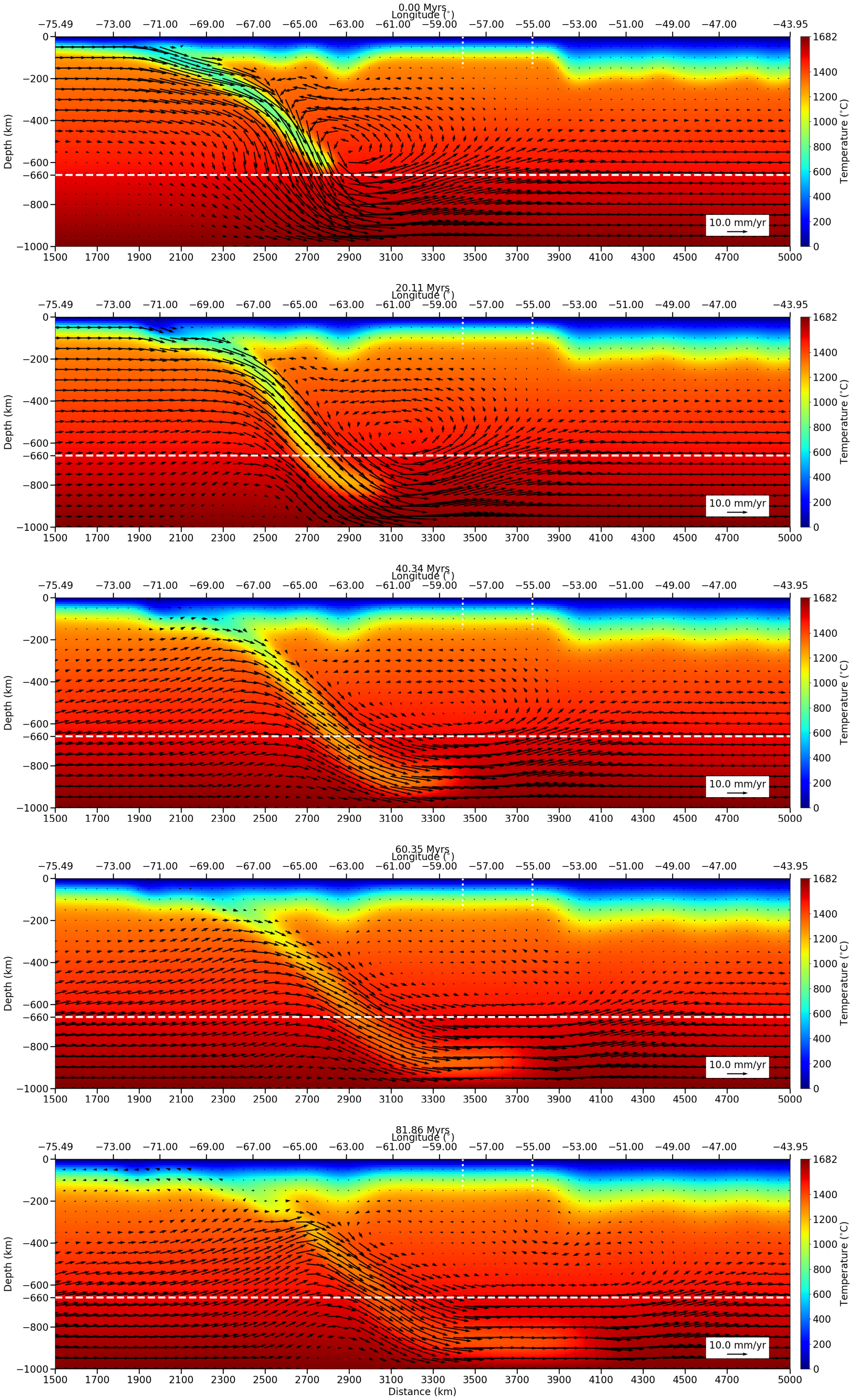

Figure 5.7: Temperature and velocity field through time for model M2.

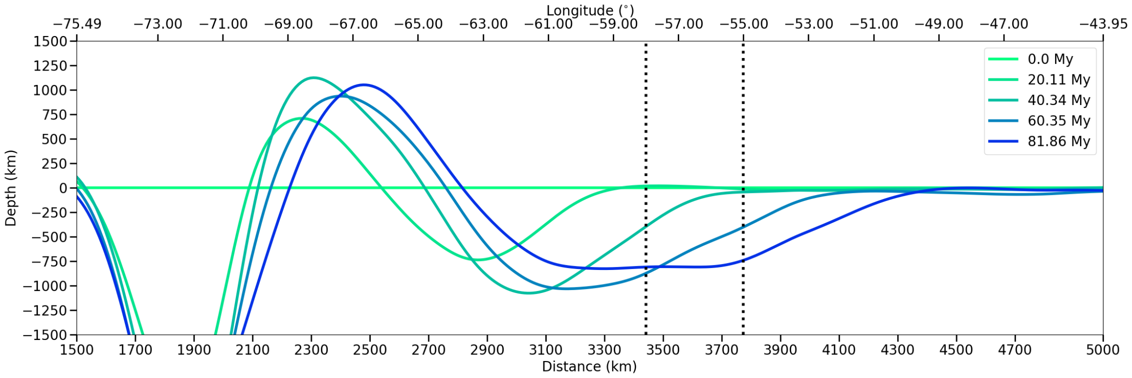

Figure 5.8: Dynamic topography evolution for the model M2.

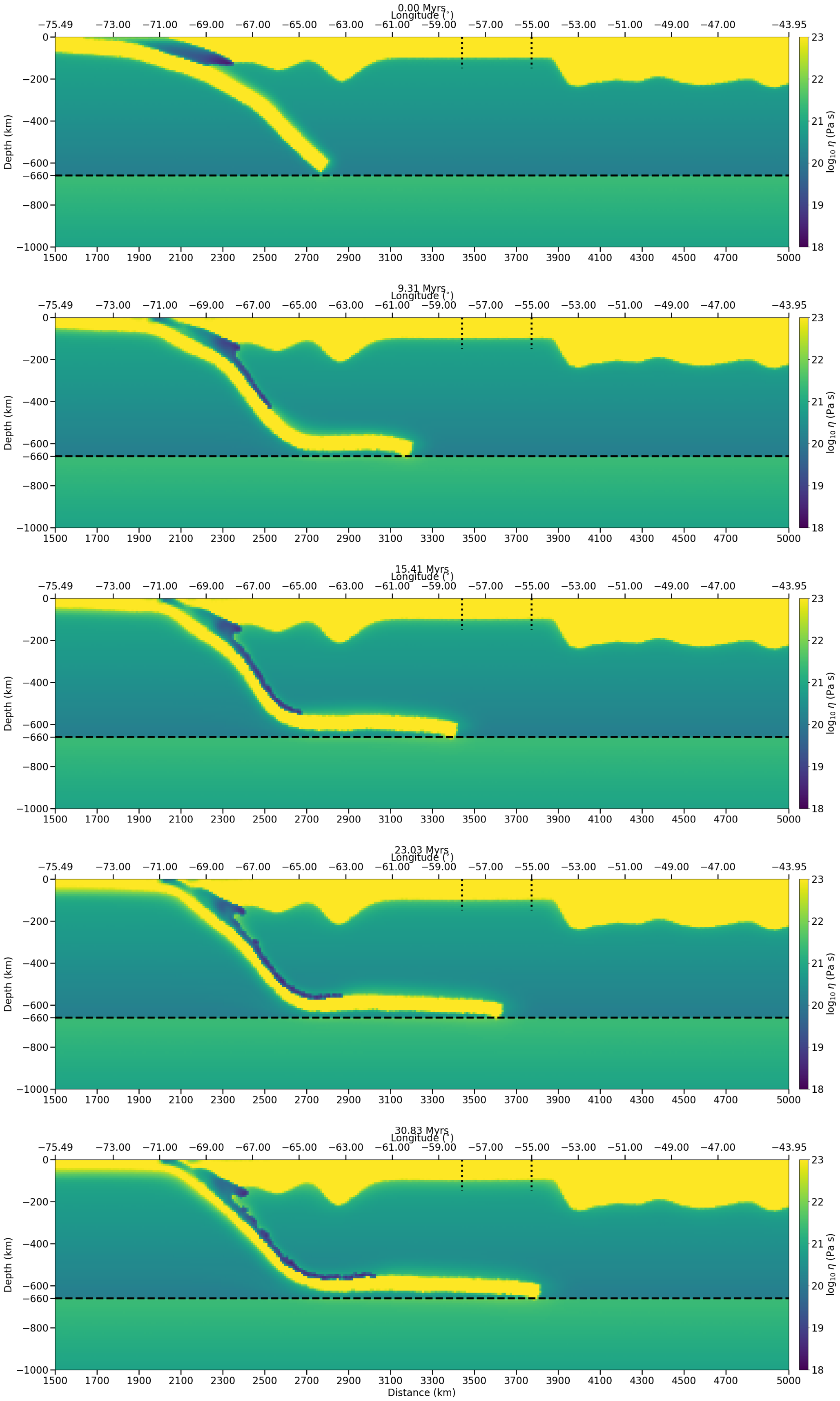

Figure 5.9: Viscosity evolution for model M3.

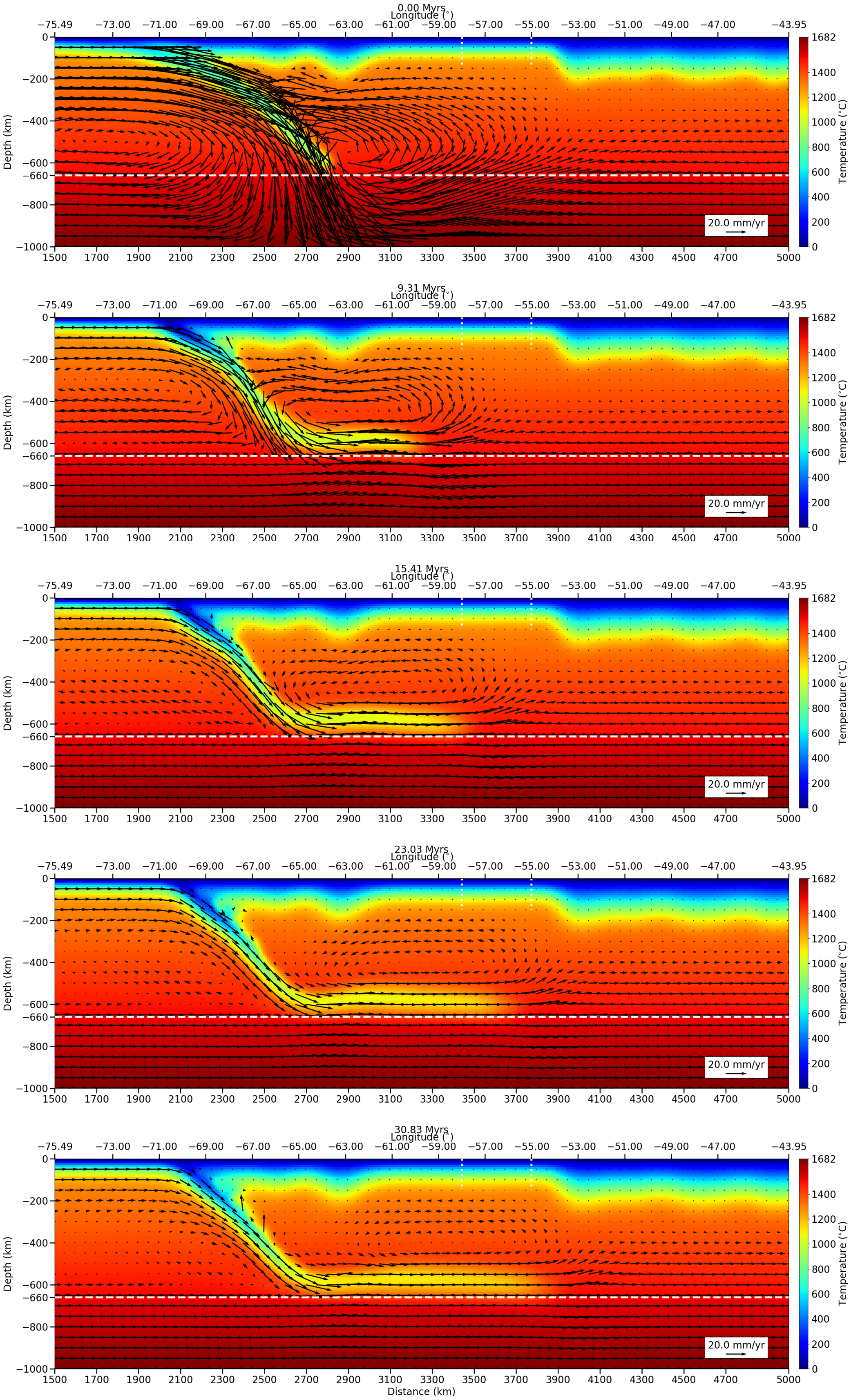

Figure 5.10: Temperature and velocity field through time for model M3.

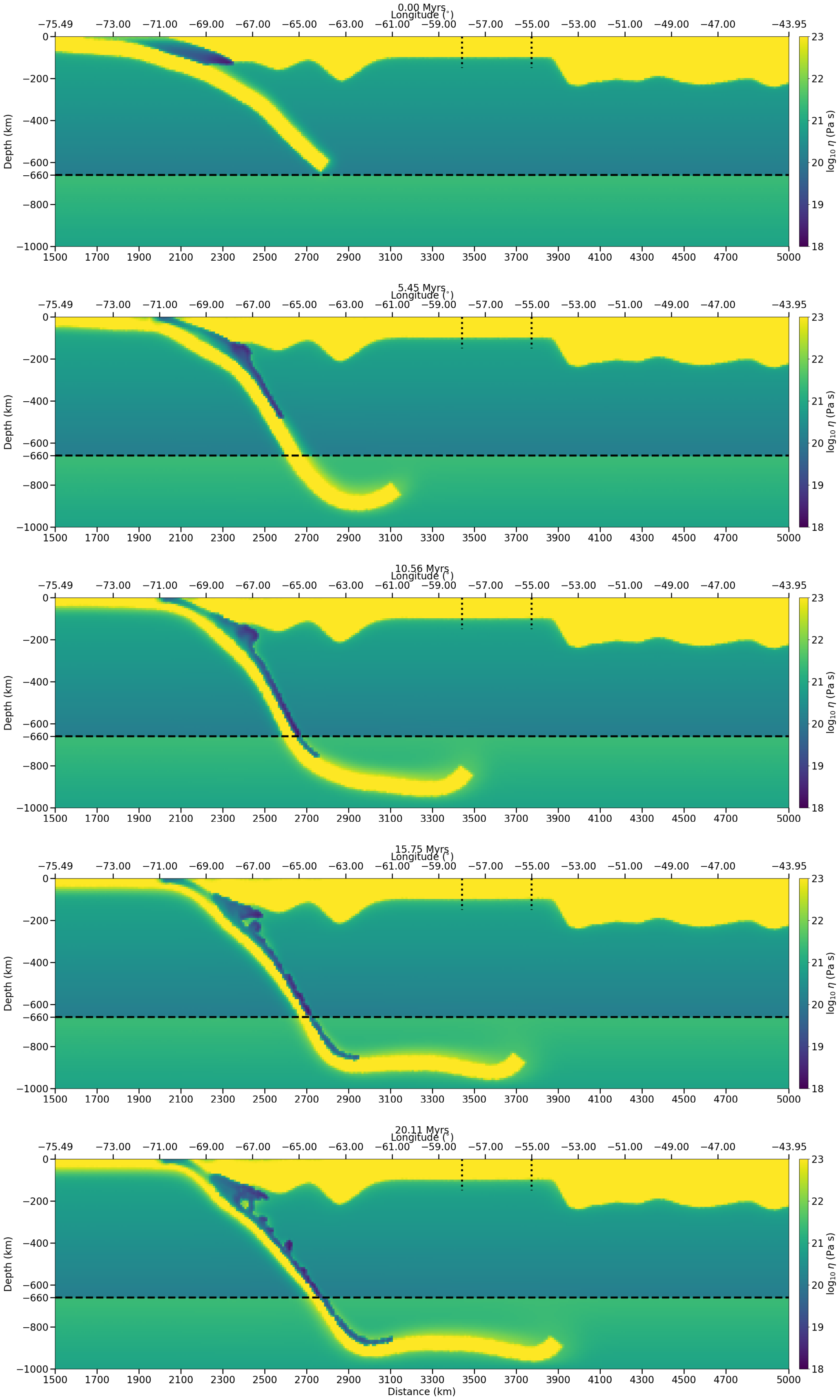

Figure 5.11: Viscosity evolution for model M4.

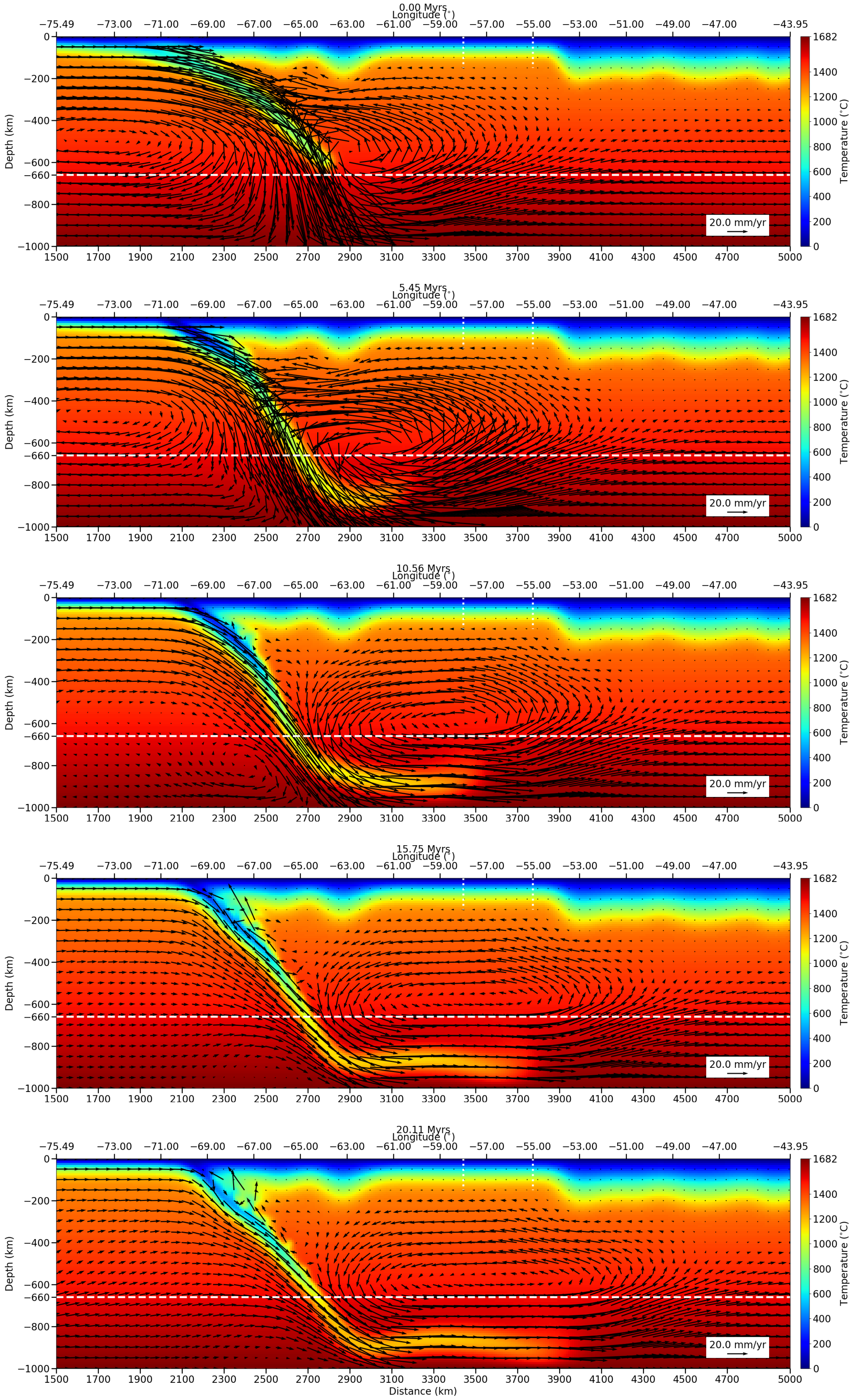

Figure 5.12: Temperature and velocity field through time for model M4.

5.3 Discussion

5.3.1 Forced slab

For the models where the subducting slab had a constant velocity, the slab was forced, there was strong coupling between the subducting slab and the South American plate. This produced a very thick region under the trench as Figures A.1 and A.2 show. A similar feature was observed on the previous buoyancy study, but its influence was small because of the simulation time that was significantly smaller. From the buoyancy study, Figure 4.3 showed how a subducting slab can move along the longitudinal direction, deforming the lubricant layer.

Once the subducting slab advanced eastwards, the whole lubricant layer was deformed and there was no way of easing the oceanic lithosphere subduction. That caused the slab to thicken below the trench region. The resulting oceanic lithosphere could not penetrate the mantle as fast as it was entering on the west side of the model, resulting in the observed coupling of the two lithospheres, and consequent thickening. This was valid for both models of different densities.

Because the continental lithosphere had its surface position fixed, this also helped to increase the thickening effect observed on both models. Such boundary condition prevented the continent from absorbing some of the stresses that were generated by the subduction.

The model with a lower mantle with a smaller density, 3300 $\mathrm{kg/m^3}$, illustrated a scenario where there would not be a phase change at the boundary between the asthenospheric mantle and the lower mantle at 660 km. That resulted in a subducting slab that did not stagnated at this boundary, which caused the Nazca plate to penetrate deeper, becoming more stretched in the process.

When the density of the lower mantle was adjusted to represent a phase change, defined as a jump of 400 $\mathrm{kg/m^3}$ in density (Gerya, 2010; Turcotte and Schubert, 2002), the slab could not enter the lower mantle region. This suggested that the phase change is crucial to the slab flattening at 660 km. Previously, it was thought that the viscosity would be the dominant factor, as it would allow a viscous force to resist the slab penetration. Although this viscous force might be acting on the subducting slab, it is now known that the density plays a very important role.

Both these simulations show how modeling subduction can be a challenge task when working with initial conditions.

5.3.2 Free slab

The other approach when simulating the Nazca plate subduction was much more promising than the forced slab approach. This was because it was possible to observe a much more behaved subduction pattern with much less coupling than the previous approach. The lubricant layer was also much more preserved through time.

The geometry of the Nazca plate observed on Figure 5.6 indicated that the slab tends to thin under those initial conditions. The excessive stretching of the plate also caused the slab to be flat, but with a dip angle less than 45°. The solution would be to either increase the compositional factor of the subducting slab, making it more rigid; increase the thickness of the lithospheric mantle; or decrease the velocity of the the underlying lower mantle and lower asthenospheric mantle, consequently.

Increasing the compositional factor caused the simulation run-time to increase dramatically and some results showed that the slab was unable to penetrate the asthenospheric mantle and horizontalize, as it was harder to bend with a higher viscosity, as seen on Figure 5.13. However other compositional factors should be tested and fine-tuned.

The simulations with densities of 3400 and 3700 $\mathrm{kg/m^3}$ for the lower mantle and a density of 3300 $\mathrm{kg/m^3}$ for the subducting slab suggested that there will be no penetration in the lower mantle if the contrast of density $\Delta\rho = \rho_{LM} - \rho_{SLAB}$ is at least 100 $\mathrm{kg/m^3}$. For the penetration to occur, it is necessary that phase change is incorporated, so the density of the subducting slab can increase with depth and time.

In future works, the full simulation of phase transitions will be incorporated in the constitutive equations, taking into account the latent heat in the energy equation, following the formulation described by Zhong et al. (2007).

Relative to the dynamic topography derived from these simulations with free slab, reasonable values were obtained for model M1, where the reference density for the oceanic lithospheric mantle is the same of the asthenospheric mantle. In this case the difference in effective density is only due to thermal effects. Additionally, the slab stayed during all the simulation in the upper mantle. The combination of these characteristics promoted a subsidence compatible with the values observed by Flament et al. (2015).

However, when the slab crossed the interface at 660 km (model M2), the density con-

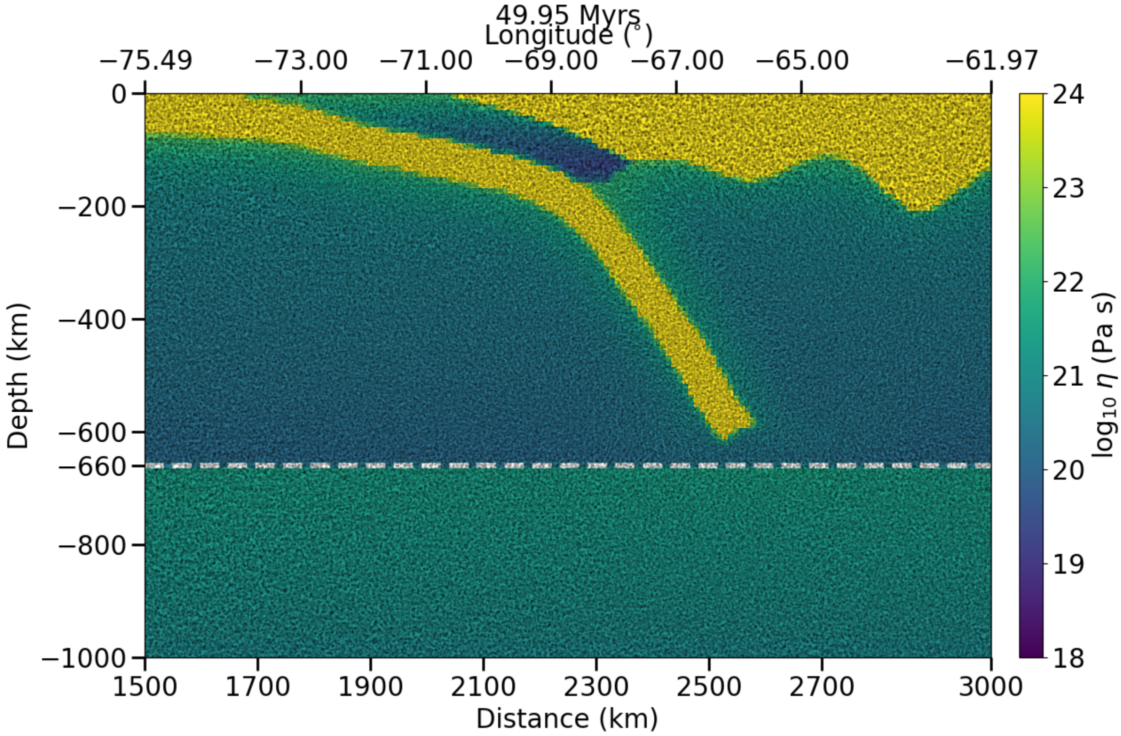

Figure 5.13: Viscosity profile simulated with a free slab approach, assuming a compositional factor for viscosity of 10^4 for the lithosphere, making the plates more rigid. The density of the lower mantle is 3700 kg/m^3 and the model initial velocity field is illustrated by Figure 3.9b. The instant is 49.95 Myr. The Lagrangian particles are presented here by small black dots.

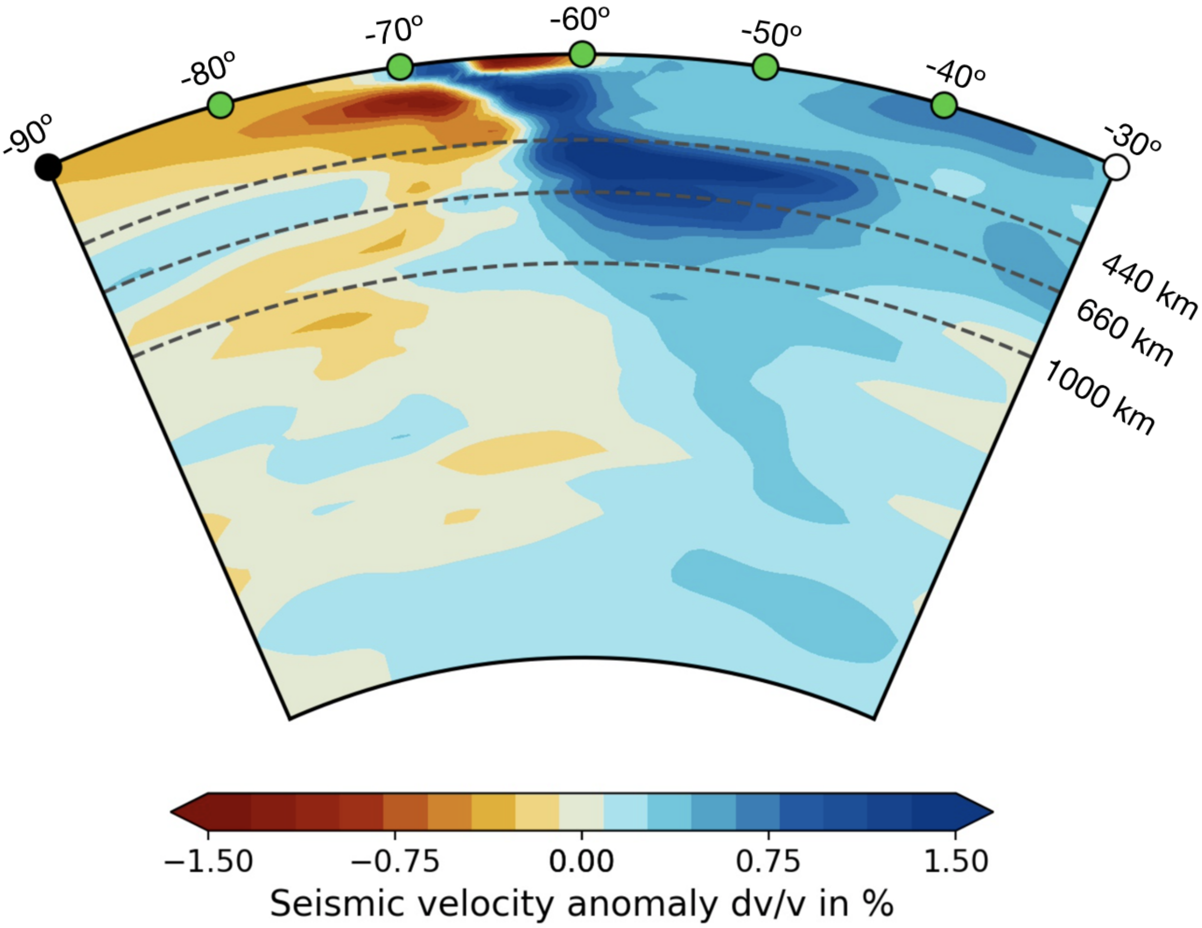

Figure 5.14: P-wave tomography profile at latitude 18°S derived from Fukao and Obayashi (2013).

trast was much larger, inducing a subsidence nearly 3 times larger than in the previous scenario. This effect was amplified when we assumed a density for the oceanic lithospheric mantle of 3400 kg/m^3 (model M3 and M4).

In fact, previous tomographic data suggest that the slab flattens above the interface of 660 km (Fukao and Obayashi, 2013) (see Figure 5.14), favoring parameters similar to the model M1. Therefore, I suggest that part of the subsidence observed in the foreland basins and in the Pantanal basin was induced by dynamic topography due to the subduction of the Nazca plate.

Certainly, other rheological models can be assumed to represent the physical behavior of the crust and mantle through time, replacing the Frank-Kamenetskii approach adopted here, using, for example, the Arrhenius law to describe the dependence on temperature and pressure, as well as other plastic weakening processes (Gerya, 2010).

Chapter 6

Conclusions

The first part of this project assessed that a subducting oceanic lithospheric mantle will deflect its trajectory according to the convection pattern of the surrounding mantle, its own rigidity and its effective density. The last comes from the ratio between the oceanic lithospheric mantle thickness and the oceanic crustal thickness, as well as their reference densities. Relatively thick oceanic lithospheric mantles with thin oceanic crust are more prone to deflect downwards than a thin slab with a thick oceanic crust. Furthermore, thin oceanic lithospheres bend easier than thick ones.

It was also concluded that for around 2.5 Myr of simulation, any value of density between 2800 and 2950 kg/m^3 can be used to represent the density of a subducting slab, for the current studied cases with respective parameters. This range of oceanic crustal density does not affect its mean deep angle considerably for the proposed thicknesses of oceanic lithospheric mantle and oceanic crust.

The second part of this project proposed that the free slab approach for a convection problem that takes several million years is more reasonable than the tested forced slab approach. The free slab approach provides less coupling between the subducting plate and the stationary plate; the subducting slab thickness is kept more or less the same across the simulation; and the model depends less on imposed extrinsic parameters. Moreover, the free slab approach also reproduces the scenario of variable subduction velocity through time, depending on the geometry and length of the subducted slab.

Within the free slab approach, the stationary continental lithosphere used as boundary condition is essential for the correct calculation of the dynamic topography through time based on a reference frame fixed on the continent.

When studying the dynamic topography through time during the subduction of the oceanic lithosphere, I observed that the amplitude of the subsidence of the continental interior depends on the geometry of the slab and the degree of penetration in the lower mantle. When the slab penetrates into the lower mantle, the replacement of hot mantle by cold oceanic lithosphere induces the amplification of the subsidence in the interior of the continent. However, when the slab flattens above the 660 km interface, the density contrast is not so abrupt and the induced dynamic topography is only a few hundreds of meters, with amplitude decreasing monotonically eastwards.

When simulating mantle convection, it is essential to incorporate phase change, as it plays an important role on the trajectory of a subducting plate at depth. Even small differences between the density of a subducting slab and the density of the lower mantle are enough to determine if the plate can sink into it.

Bibliography

Angermann D., Klotz J., Reigber C., Space-geodetic estimation of the Nazca-South America Euler vector, Earth and Planetary Science Letters, 1999, vol. 171, p. 329

Assumpção M., Suárez G., Source mechanisms of moderate-size earthquakes and stress orientation in mid-plate South America, Geophysical Journal International, 1988, vol. 92, p. 253

Auer L., Boschi L., Becker T., Nissen-Meyer T., Giardini D., Savani: A variable resolution whole-mantle model of anisotropic shear velocity variations based on multiple data sets, Journal of Geophysical Research: Solid Earth, 2014, vol. 119, p. 3006

Bercovici D., , 2007 in , Vol. 7, Treatise on Geophysics, Volume 7: Mantle Dynamics 1 edn, Elsevier Amsterdam Chapt. 1 pp 1–30

Bergier I., Assine M. L., Dynamics of the Pantanal Wetland in South America, 2016

Braun J., The many surface expressions of mantle dynamics, Nature Geoscience, 2010, vol. 3, p. 825

Byerlee J. D., Brittle-ductile transition in rocks, Journal of Geophysical Research, 1968, vol. 73, p. 4741

Christensen U. R., Yuen D. A., The interaction of a subducting lithospheric slab with a chemical or phase boundary, Journal of Geophysical Research: Solid Earth, 1984, vol. 89, p. 4389

Dávila F. M., Lithgow-Bertelloni C., Dynamic topography in South America, Journal of South American Earth Sciences, 2013, vol. 43, p. 127

de Freitas R. O., Ensaio sobre a tectônica moderna do Brasil, Boletim da Faculdade de Filosofia Ciências e Letras, Universidade de São Paulo. Geologia, 1951, pp 7–107

Eakin C. M., Lithgow-Bertelloni C., Dávila F. M., Influence of Peruvian flat-subduction dynamics on the evolution of western Amazonia, Earth and Planetary Science Letters, 2014, vol. 404, p. 250

Flament N., Gurnis M., Müller R. D., Bower D. J., Husson L., Influence of subduction history on South American topography, Earth and Planetary Science Letters, 2015, vol. 430, p. 9

Forte A., Peltier W., Dziewonski A., Inferences of mantle viscosity from tectonic plate velocities, Geophysical research letters, 1991, vol. 18, p. 1747

Fowler C. M. R., The Solid Earth, An Introduction to Global Geophysics 2 edn. Cambridge University Press New York, 2002

French S., Romanowicz B., Whole-mantle radially anisotropic shear velocity structure from spectral-element waveform tomography, Geophysical Journal International, 2014, vol. 199, p. 1303

Fukao Y., Obayashi M., Subducted slabs stagnant above, penetrating through, and trapped below the 660 km discontinuity, Journal of Geophysical Research: Solid Earth, 2013, vol. 118, p. 5920

Gerya T., Introduction to numerical geodyamic modelling 1 edn. Cambridge University Press Cambridge, 2010

Gurnis M., Rapid continental subsidence following the initiation and evolution of subduction, Science, 1992, vol. 255, p. 1556

Gurnis M., Hager B. H., Controls of the structure of subducted slabs, Nature, 1988, vol. 335, p. 317

Hager B. H., Clayton R. W., Richards M. A., Comer R. P., Dziewonski A. M., Lower mantle heterogeneity, dynamic topography and the geoid, Nature, 1985, vol. 313, p. 541

Hayes G. P., Moore G. L., Portner D. E., Hearne M., Flamme H., Furtney M., Smoczyk G. M., Slab2, a comprehensive subduction zone geometry model, Science, 2018, vol. 362, p. 58

Horton B. K., DeCelles P. G., The modern foreland basin system adjacent to the Central Andes, Geology, 1997, vol. 25, p. 895

Hu J., Faccenda M., Liu L., Subduction-controlled mantle flow and seismic anisotropy in South America, Earth and Planetary Science Letters, 2017, vol. 470, p. 13

Ita J., King S. D., The influence of thermodynamic formulation on simulations of subduction zone geometry and history, Geophysical research letters, 1998, vol. 25, p. 1463

King S., , 2007 in , Vol. 7, Treatise on Geophysics, Volume 7: Mantle Dynamics 1 edn, Elsevier Amsterdam Chapt. 8 pp 325–370

King S. D., Hager B. H., Subducted slabs and the geoid: 1. Numerical experiments with temperature-dependent viscosity, Journal of Geophysical Research: Solid Earth, 1994, vol. 99, p. 19843

King S. D., Masters G., An inversion for radial viscosity structure using seismic tomography, Geophysical Research Letters, 1992, vol. 19, p. 1551

King S. D., Raefsky A., Hager B. H., ConMan: Vectorizing a finite element code for incompressible two-dimensional convection in the Earth's mantle, Physics of the Earth and Planetary Interiors, 1990, vol. 59, p. 195

Korenaga J., Initiation and evolution of plate tectonics on Earth: theories and observations, Annual review of earth and planetary sciences, 2013, vol. 41, p. 117

Lithgow-Bertelloni C., Silver P. G., Dynamic topography, plate driving forces and the African superswell, Nature, 1998, vol. 395, p. 269

McKenzie D. P., Speculations on the consequences and causes of plate motions, Geophysical Journal International, 1969, vol. 18, p. 1

Minear J. W., Toksöz M. N., Thermal regime of a downgoing slab and new global tectonics, Journal of Geophysical Research, 1970, vol. 75, p. 1397

Mitrovica J., Beaumont C., Jarvis G., Tilting of continental interiors by the dynamical effects of subduction, Tectonics, 1989, vol. 8, p. 1079

Molnar P., England P. C., Jones C. H., Mantle dynamics, isostasy, and the support of high terrain, Journal of Geophysical Research: Solid Earth, 2015, vol. 120, p. 1932

Moucha R., Forte A. M., Mitrovica J. X., Rowley D. B., Quéré S., Simmons N. A., Grand S. P., Dynamic topography and long-term sea-level variations: There is no such thing as a stable continental platform, Earth and Planetary Science Letters, 2008, vol. 271, p. 101

Norabuena E. O., Dixon T. H., Stein S., Harrison C. G., Decelerating Nazca-South America and Nazca-Pacific plate motions, Geophysical Research Letters, 1999, vol. 26, p. 3405

Pasyanos M. E., Masters T. G., Laske G., Ma Z., LITHO1. 0: An updated crust and lithospheric model of the Earth, Journal of Geophysical Research: Solid Earth, 2014, vol. 119, p. 2153

Petersen K. D., Nielsen S., Clausen O., Stephenson R., Gerya T., Small-scale mantle convection produces stratigraphic sequences in sedimentary basins, Science, 2010, vol. 329, p. 827

Priestley K., Tilmann F., Relationship between the upper mantle high velocity seismic lid and the continental”lithosphere, Lithos, 2009, vol. 109, p. 112

Ranalli G., Rheology of the Earth. Springer Science & Business Media, 1995

Ribe N. M., , 2007 in , Vol. 7, Treatise on Geophysics, Volume 7: Mantle Dynamics 1 edn, Elsevier Amsterdam Chapt. 1 pp 167–226

Ricard Y., Vigny C., Froidevaux C., Mantle heterogeneities, geoid, and plate motion: a Monte Carlo inversion, Journal of Geophysical Research: Solid Earth, 1989, vol. 94, p. 13739

Sacek V., Post-rift influence of small-scale convection on the landscape evolution at divergent continental margins, Earth and Planetary Science Letters, 2017, vol. 459, p. 48

Schaeffer A., Lebedev S., Global shear speed structure of the upper mantle and transition zone, Geophysical Journal International, 2013, vol. 194, p. 417

Schellart W. P., Freeman J., Stegman D. R., Moresi L., May D., Evolution and diversity of subduction zones controlled by slab width, Nature, 2007, vol. 446, p. 308

Shephard G., Müller R., Liu L., Gurnis M., Miocene drainage reversal of the Amazon River driven by plate–mantle interaction, Nature Geoscience, 2010, vol. 3, p. 870

Solomatov V., Moresi L.-N., Scaling of time-dependent stagnant lid convection: Application to small-scale convection on Earth and other terrestrial planets, Journal of Geophysical Research: Solid Earth, 2000, vol. 105, p. 21795

Stein S., Wysession M., An introduction to seismology, earthquakes, and earth structure. John Wiley & Sons, 2009

Steinberger B., Effects of latent heat release at phase boundaries on flow in the Earth's mantle, phase boundary topography and dynamic topography at the Earth's surface, Physics of the Earth and Planetary Interiors, 2007, vol. 164, p. 2

Steinberger B., Conrad C. P., Tutu A. O., Hoggard M. J., On the amplitude of dynamic topography at spherical harmonic degree two, Tectonophysics, 2017

Turcotte D. L., Schubert G., Geodynamics 2 edn. Cambridge University Press New York, 2002

Ussami N., Shiraiwa S., Dominguez J. M. L., Basement reactivation in a sub-Andean foreland flexural bulge: The Pantanal wetland, SW Brazil, Tectonics, 1999, vol. 18, p. 25

Yuan H., Romanowicz B., Lithospheric layering in the North American craton, Nature, 2010, vol. 466, p. 1063

Zhong S. J., Yuen D. A., Moresi L. N., , 2007 in Bercovici D., ed., , Vol. 7, Treatise on Geophysics, Volume 7: Mantle Dynamics 1 edn, Elsevier Amsterdam Chapt. 5 pp 227–252

Appendix

Appendix A

Forced slab simulations

The first simulations used the mean global oceanic crust density 2950 kg/m^3 (Gerya, 2010), and the Slab2 thickness provided by Hayes et al. (2018). Figures A.1 and A.2 show the behaviour of two different simulations with different lower mantle densities. For a lower mantle with a density of 3300 kg/m^3, Figure A.1 shows the viscosity profiles at the beginning and at the end of the simulation (Figures A.2a and A.2c), and the temperature profile at the end of the simulation A.2c.

For a lower mantle with a density of 3700 kg/m^3, representing the mean contrast density between the asthenospheric mantle and the lower mantle (Turcotte and Schubert, 2002), the viscosity profiles generated are shown on figures A.1a and A.1b. The temperature profile at 50 Myr is on Figure A.1c.

When The lower mantle density is 3300 kg/m^3, the subducting slab penetrates it without much difficulty, contrasting with the simulation where the lower mantle density was 3700 kg/m^3, where the subducting slab stays horizontal right above 660 km interface.

Both simulations show a severe deformation of the lubricant layer, making it sink over the subducting Nazca plate beneath while being compressed between the two tectonic plates. On both simulations, the subducting slab thickened below the oceanic trench region. Nevertheless, the slab maintains the same thickness beyond the thickened region.

Regarding the velocity field, on figures A.2c and A.1c, the velocity amplitudes are significantly higher in the lower mantle when the density is smaller.

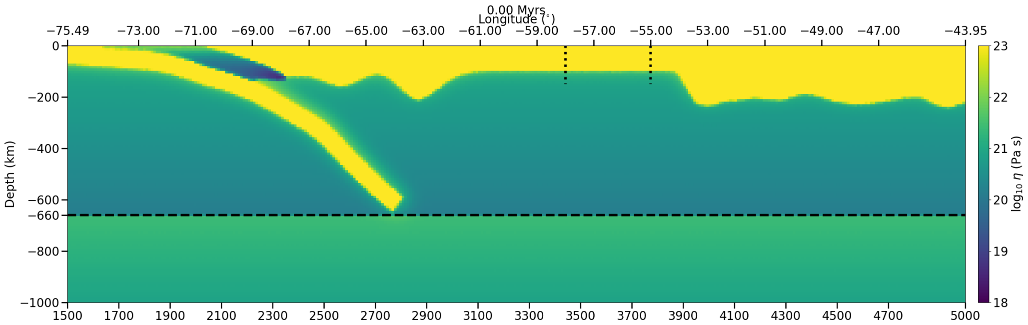

(a) Viscosity profile at the beginning of the simulation.

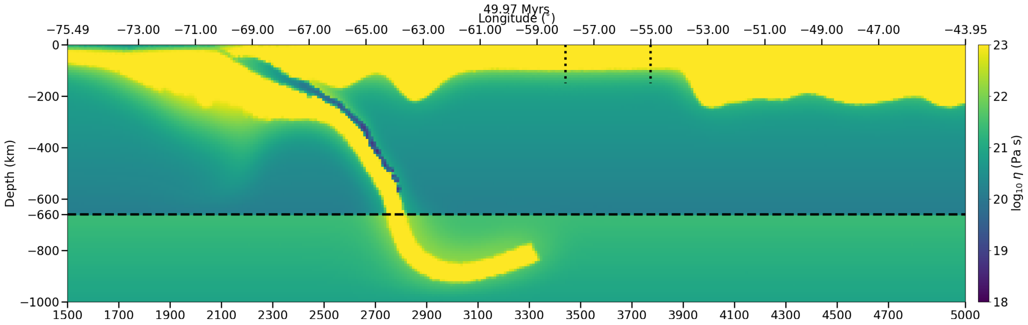

(b) Viscosity profile after ∼ 50 Myr.

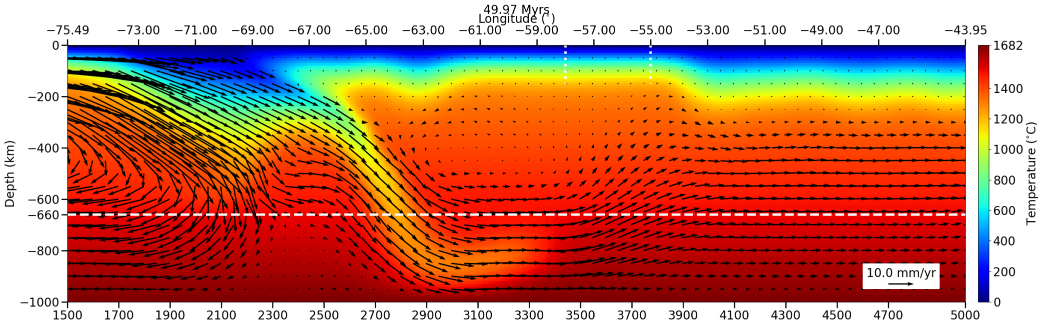

(c) Thermal e velocity profile after ∼ 50 Myr.

Figure A.1: Viscosity, temperature and velocity for a lower mantle with a viscosity of 3300 kg/m^3.

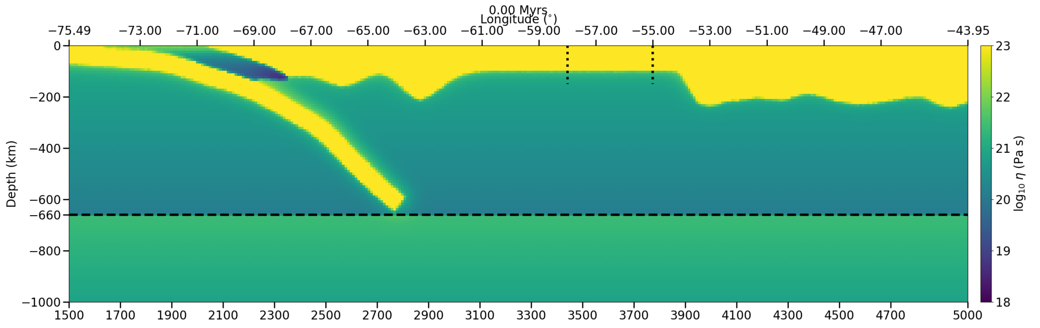

(a) Viscosity profile at the beginning of the simulation.

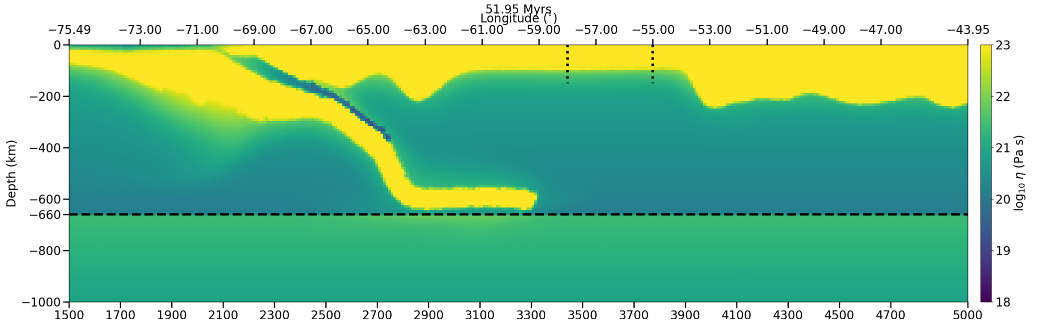

(b) Viscosity profile after ∼ 50 Myr.

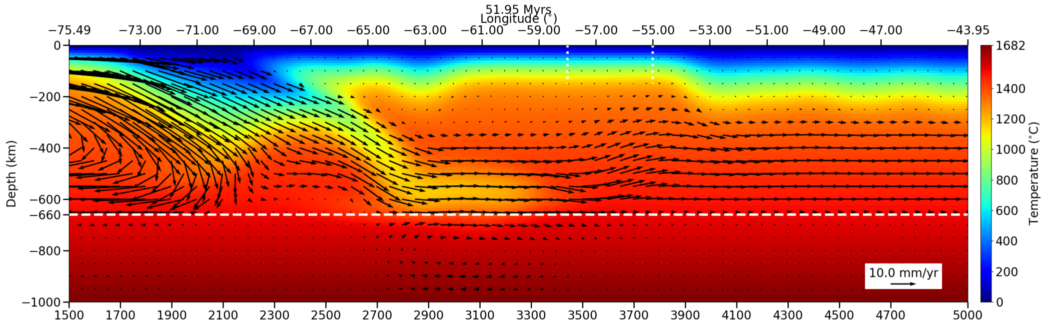

(c) Thermal e velocity profile after ∼ 50 Myr.

Figure A.2: Viscosity, temperature and velocity for a lower mantle with a viscosity of 3700 kg/m^3.

Appendix B

Free slab simulations

On this chapter, the results for the free slab simulations are presented. To make it easy to the reader, all the simulations of each group are briefly presented before all the results for each group are shown.

B.0.1 Free continental slab - FCS

Simulation FCS 01. FCS simulation, where $\rho_{LM} = 3300$ kg/m^3, $\rho_{OL} = 3300$ kg/m^3, $C_{OC} = 1000$, $C_{OL} = 1000$, $v_{LM} = 20$ mm/yr. The boundary conditions for the velocity are those from the SVM in Section 3.2.4, similar to Figure 3.9b.

Simulation FCS 02. FCS simulation, where $\rho_{LM} = 3300$ kg/m^3, $\rho_{OL} = 3300$ kg/m^3, $C_{OC} = 1000$, $C_{OL} = 1000$, $v_{LM} = 10$ mm/yr. The boundary conditions for the velocity are those from the SVM in Section 3.2.4, similar to Figure 3.9b, but the amplitude was halved.

Simulation FCS 03. FCS simulation, where $\rho_{LM} = 3700$ kg/m^3, $\rho_{OL} = 3300$ kg/m^3, $C_{OC} = 1000$, $C_{OL} = 1000$, $v_{LM} = 20$ mm/yr. The boundary conditions for the velocity are those from the SVM in Section 3.2.4, similar to Figure 3.9b.

Simulation FCS 04. FCS simulation, where $\rho_{LM} = 3700$ kg/m^3, $\rho_{OL} = 3300$ kg/m^3, $C_{OC} = 1000$, $C_{OL} = 1000$, $v_{LM} = 10$ mm/yr. The boundary conditions for the velocity are those from the SVM in Section 3.2.4, similar to Figure 3.9b, but the amplitude was halved.

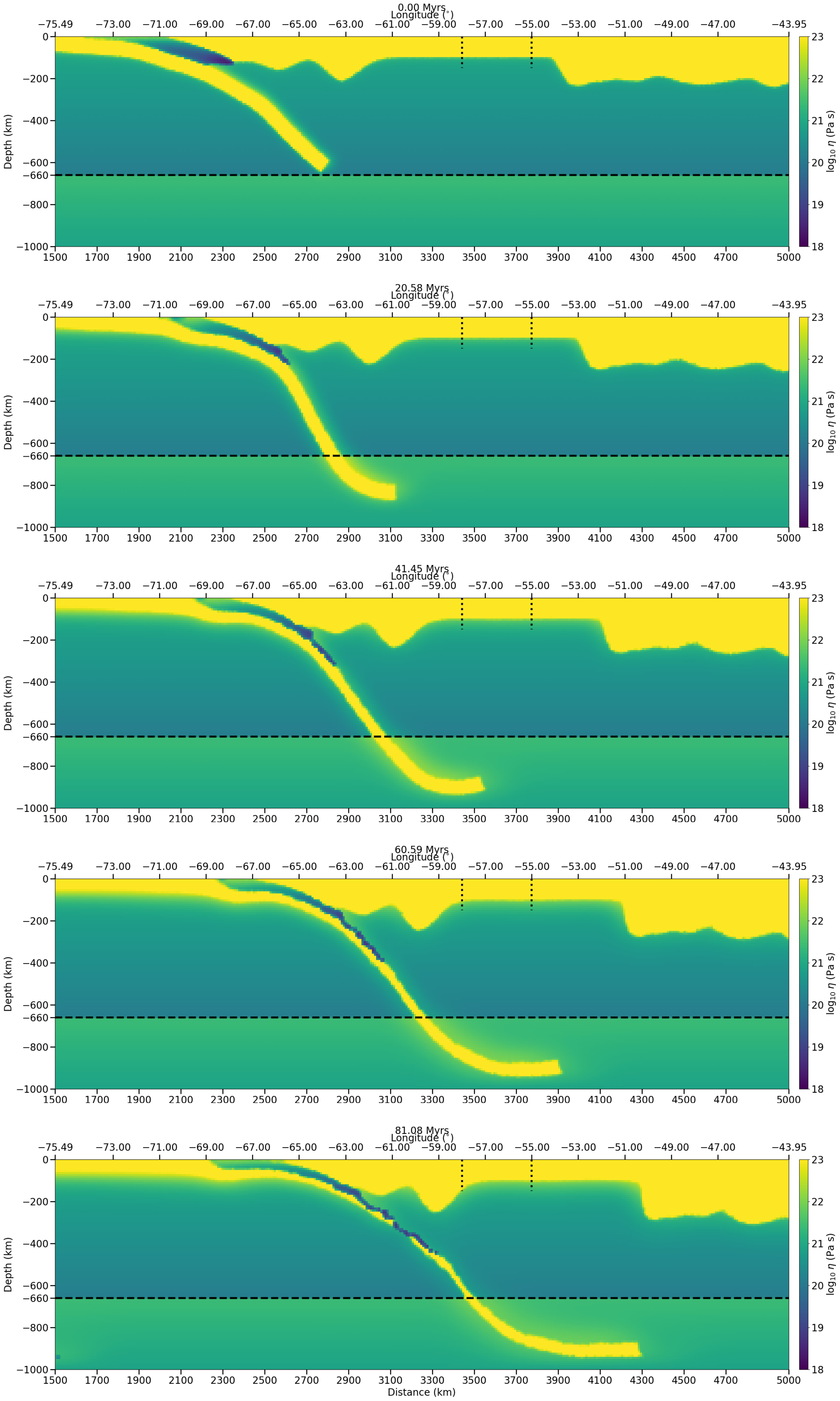

Figure B.1: Viscosity evolution for Simulation FCS 01.

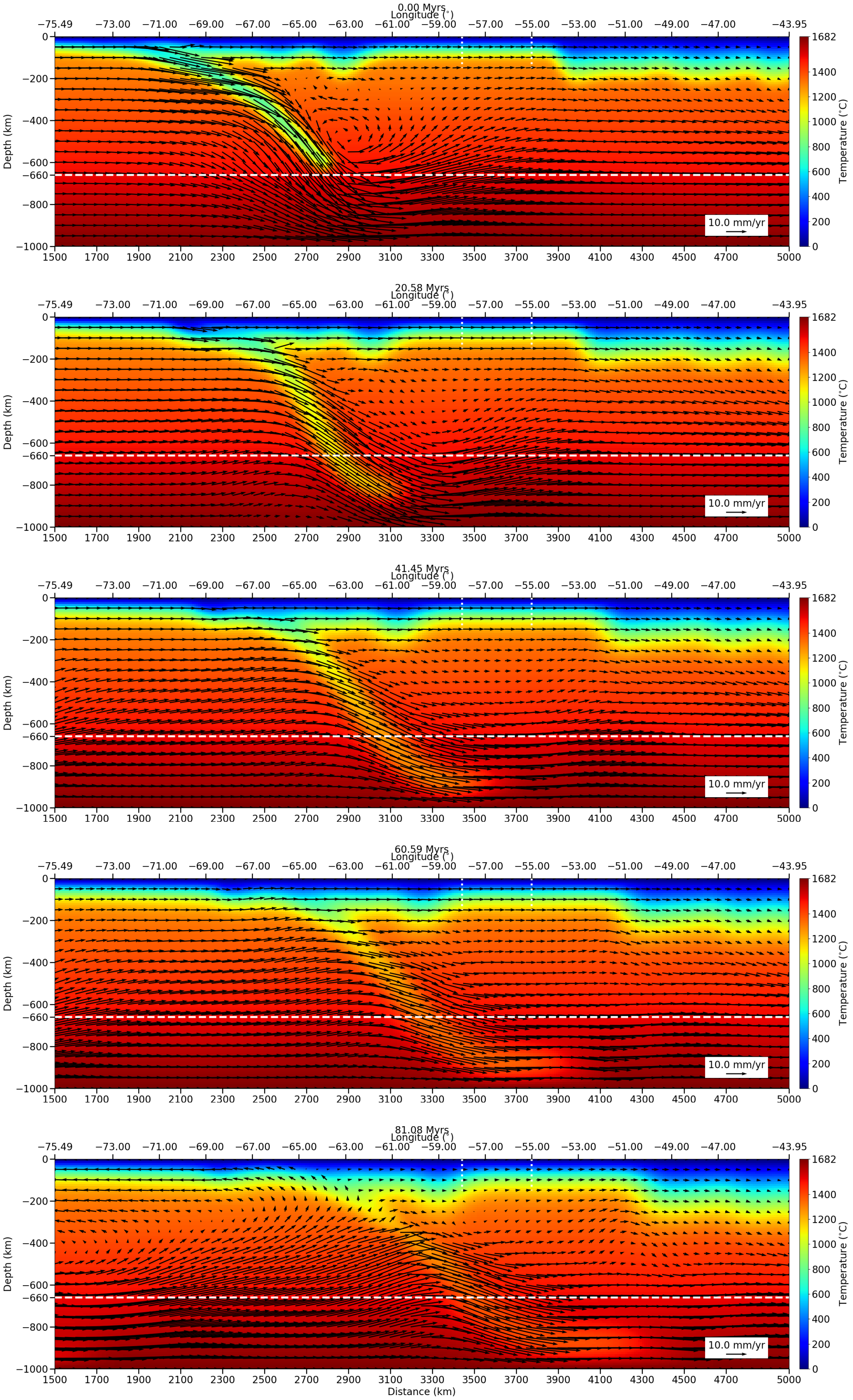

Figure B.2: Temperature and velocity field through time for Simulation SCS 01.

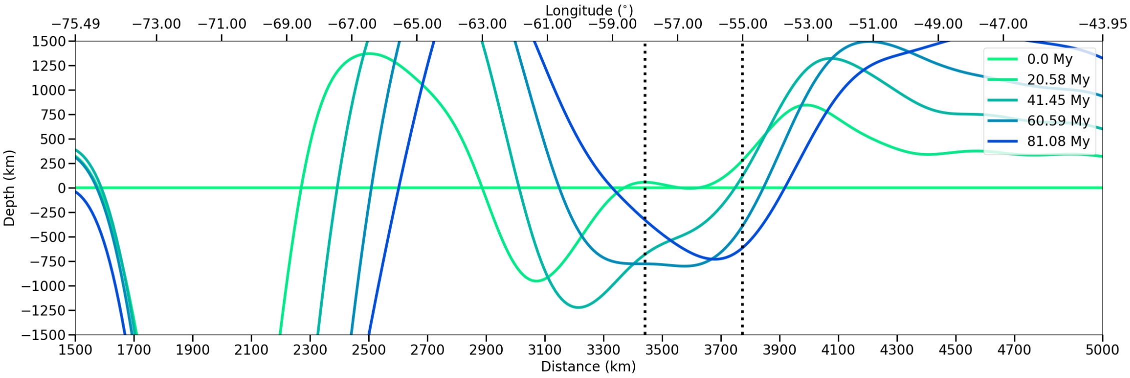

Figure B.3: Dynamic topography evolution for the Simulation FCS 01.

Figures B.1 showed great stretching for the subducting slab, causing it break-off around 80 Myr, better noticeable on Figure B.2. As the slab penetrated the lower mantle, it was pushed towards the east at the same speed as the lower mantle, which caused the slab to move until about 51°W.

The velocity and temperature evolution observed in Figure B.2 showed a vigorous flow across the domain with upward flow observed under the thinner continental slab and downward flow under the thicker continental area. Intense deformation of the lubricant layer and consequent drag occurred.

From the dynamic topography evolution (Figure B.3), we can see a very dynamic behaviour. This was caused because the continent moved eastward and the dynamic topography is not calculated properly anymore. Therefore, it is not a case where I can apply the current methodology for calculating the dynamic topography.

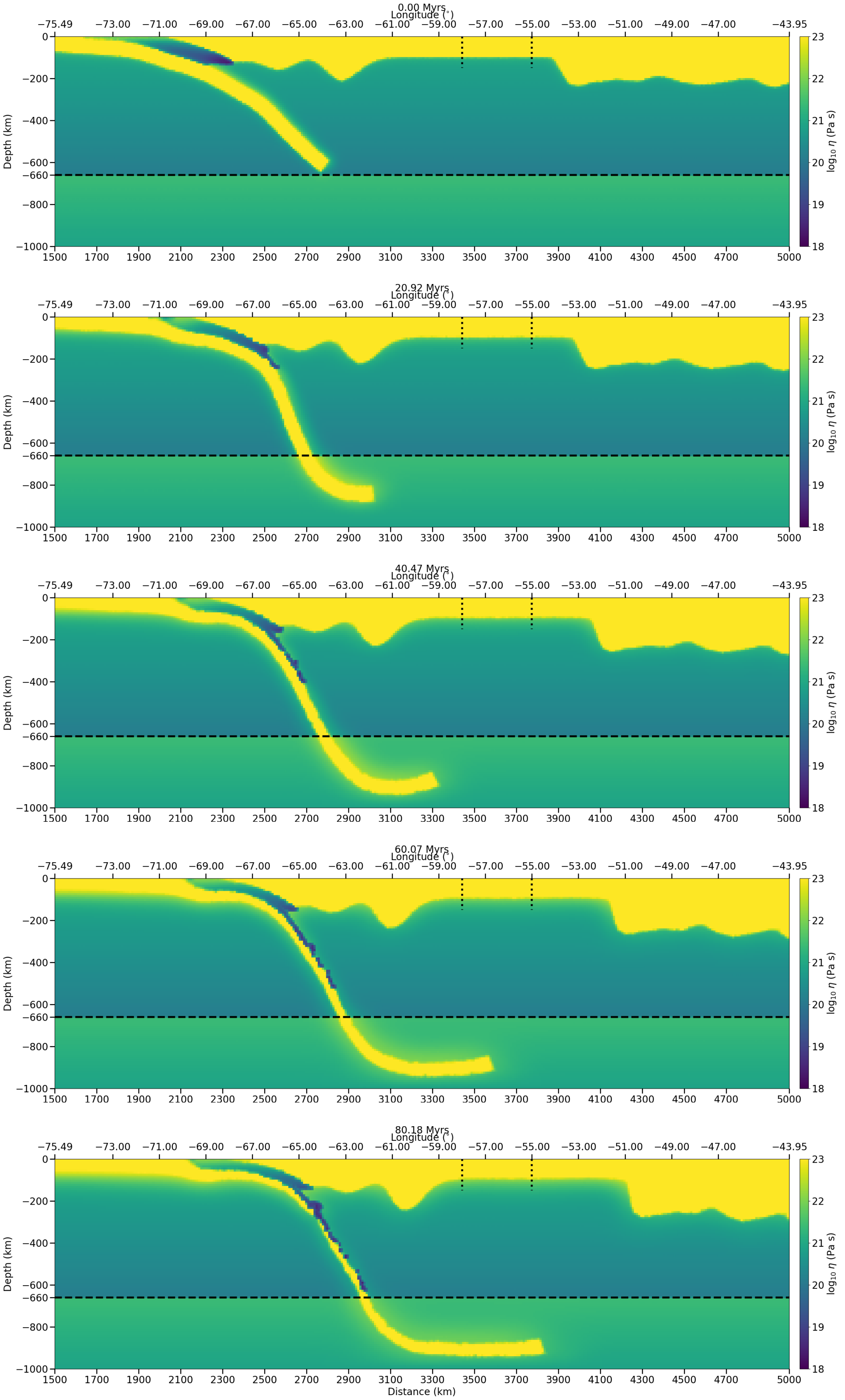

Figure B.4: Viscosity evolution for Simulation FCS 02.

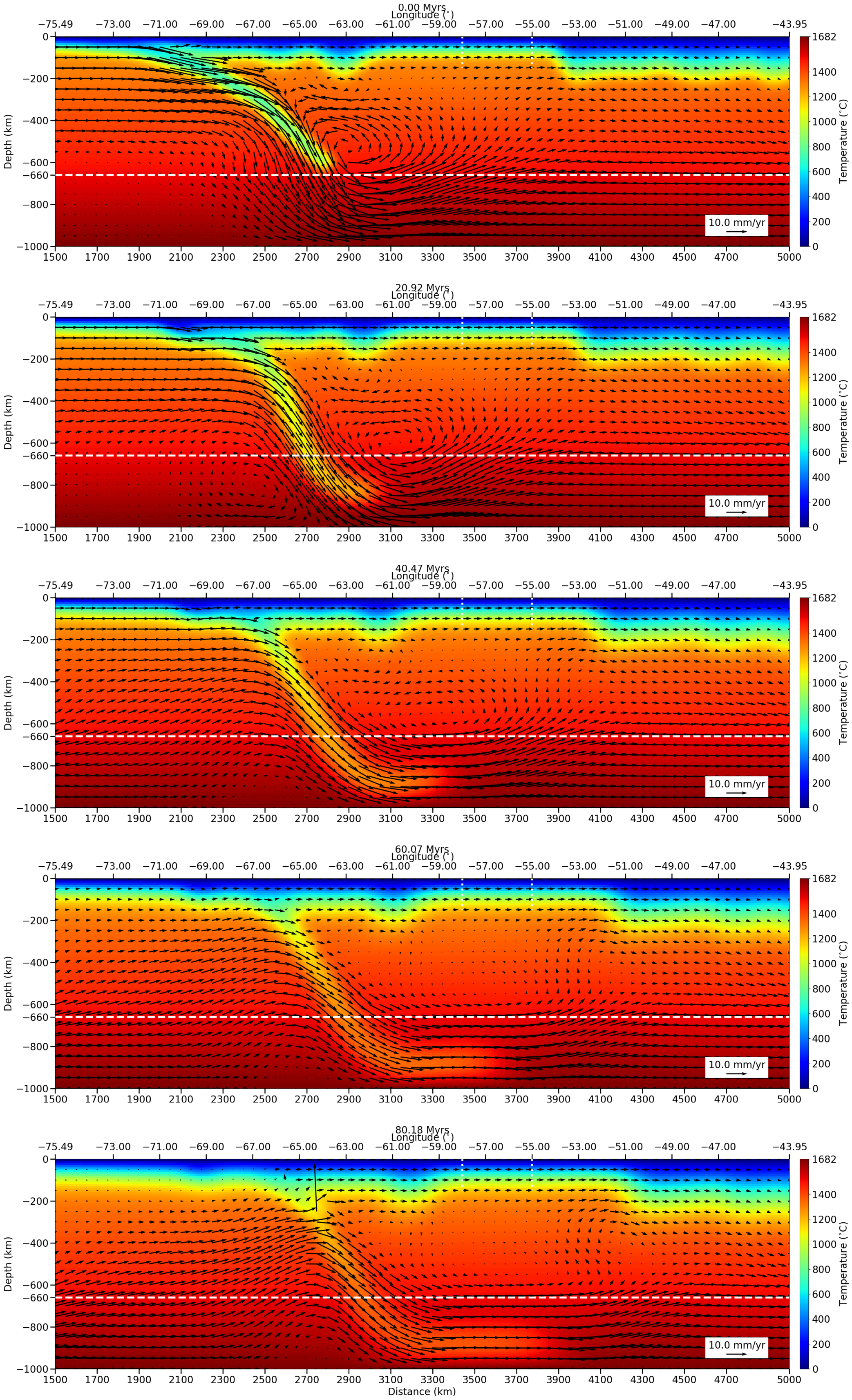

Figure B.5: Temperature and velocity field through time for Simulation FCS 02.

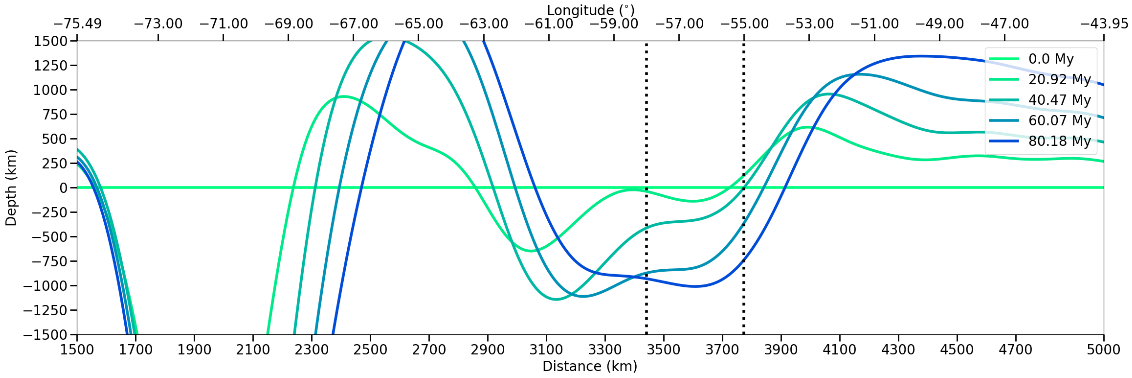

Figure B.6: Dynamic topography evolution for the Simulation FCS 02.

Figure B.4 showed stretching along the slope of the subducting slab and a portion of the lubricant layer was dragged until the 660 km interface. Different from the previous simulation with a v_{LM} twice the amplitude, there was no break-off in this simulation. The slab remained intact and horizontal at the bottom of the model.

Because this is a a FCS, the continent migrates to the east compressed by the subducting plate.

The thermal and velocity fields evolution presented a much more complex convecting system between the subducting slab and the overlying continental slab (Figure B.5) where the velocities decreased in amplitude with time.

Again, the topography evolution is not reliable (Figure B.6).

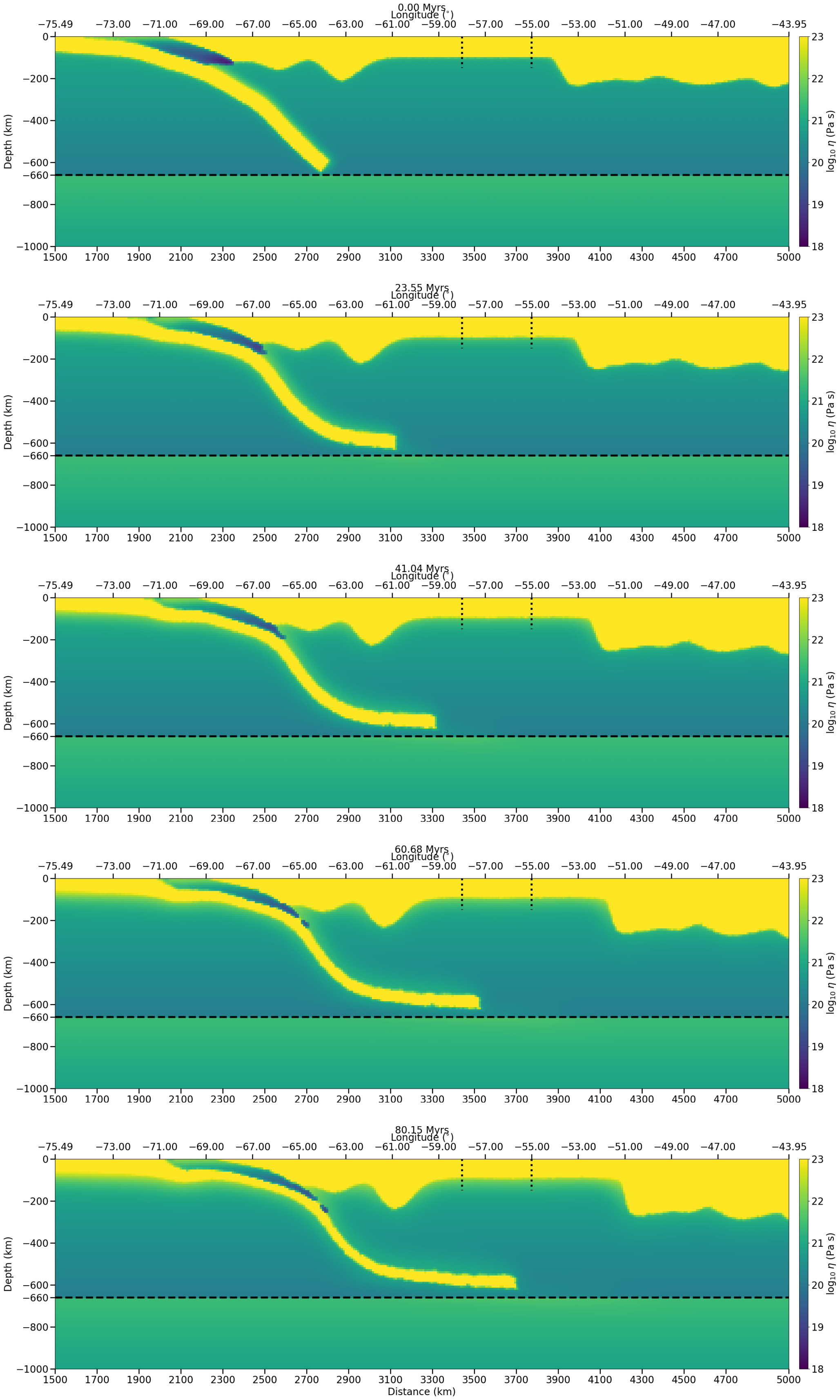

Figure B.7: Viscosity evolution for Simulation FCS 03.

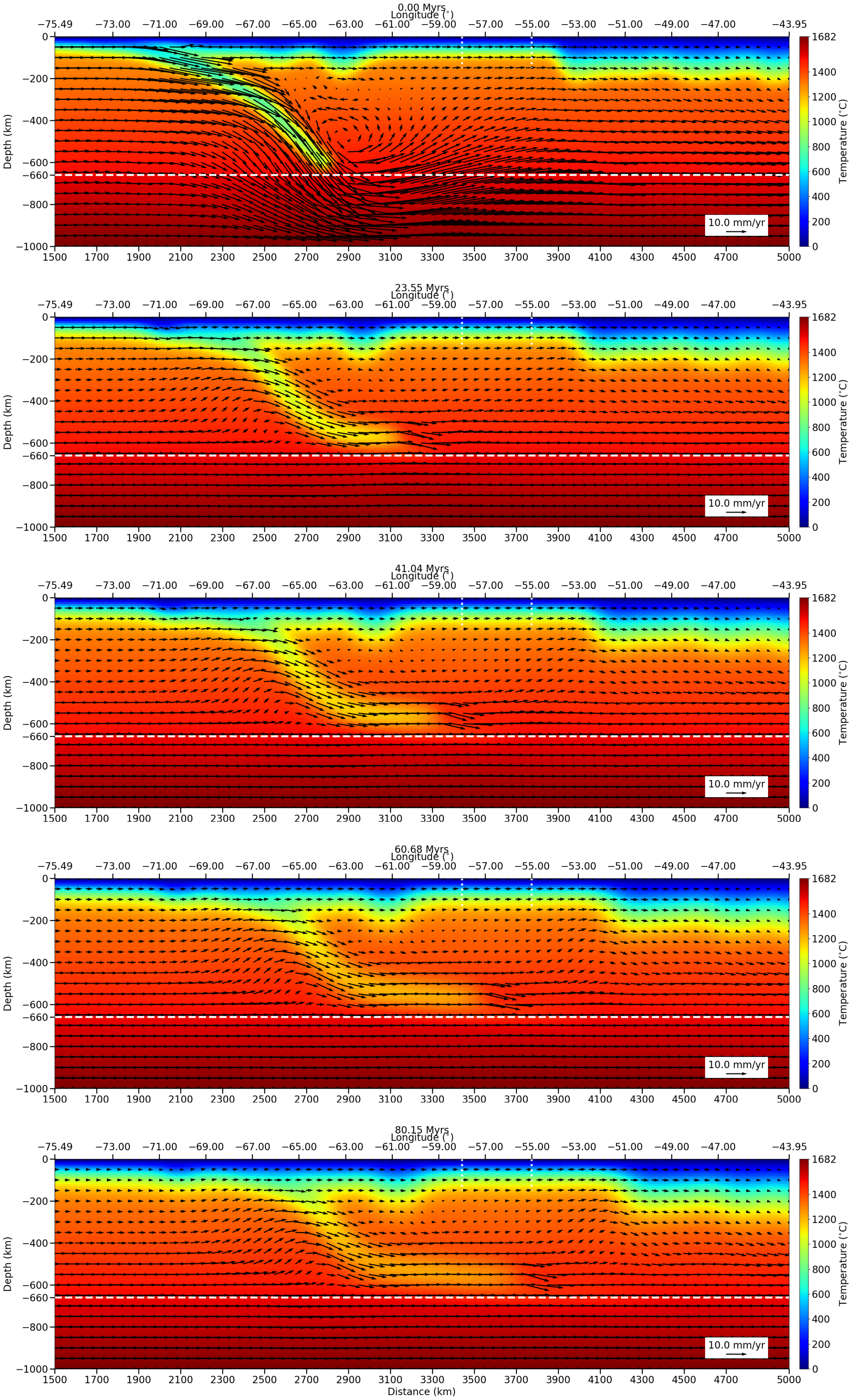

Figure B.8: Temperature and velocity field through time for Simulation FCS 03.

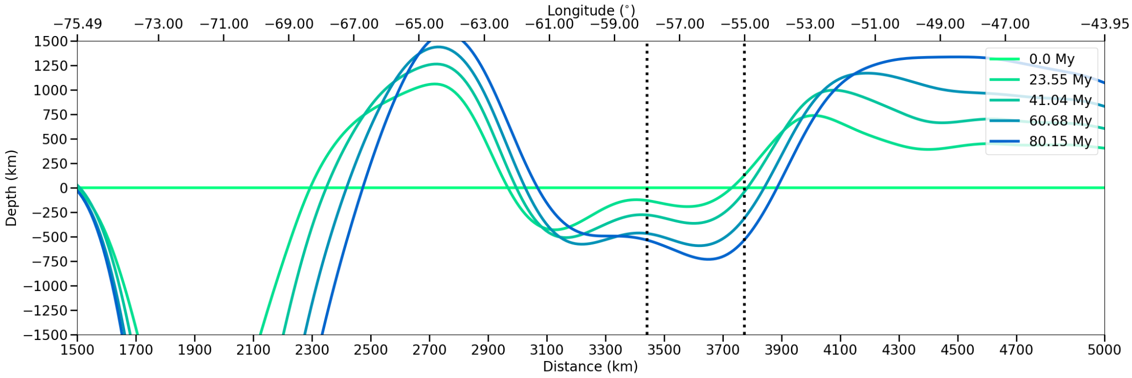

Figure B.9: Dynamic topography evolution for the Simulation FCS 03.

While the lubricant unit was compressed and deformed through time, it was dragged with the subducting oceanic lithosphere for a couple of kilometers (Figure B.7). The subducting plate also stretched in the process, with some coupling with the lubricant layer. The velocity field evolution was subtle, with a main west-to-east flow direction since 20 Myr. Some upward flow under the continental area appears around the same time. The cold subducting slab was very horizontal right above the 660 km interface and the observed diffusion pattern (Figure B.8) showed the subducting slab heated and consequently the asthenospheric mantle cooled around it.

The topography evolution has an eastward migration component due to the adopted velocity boundary condition (Figure B.9). Allowing the continental slab to move freely on the surface caused its compression and drift to the east, as figures B.7 and B.8 show.

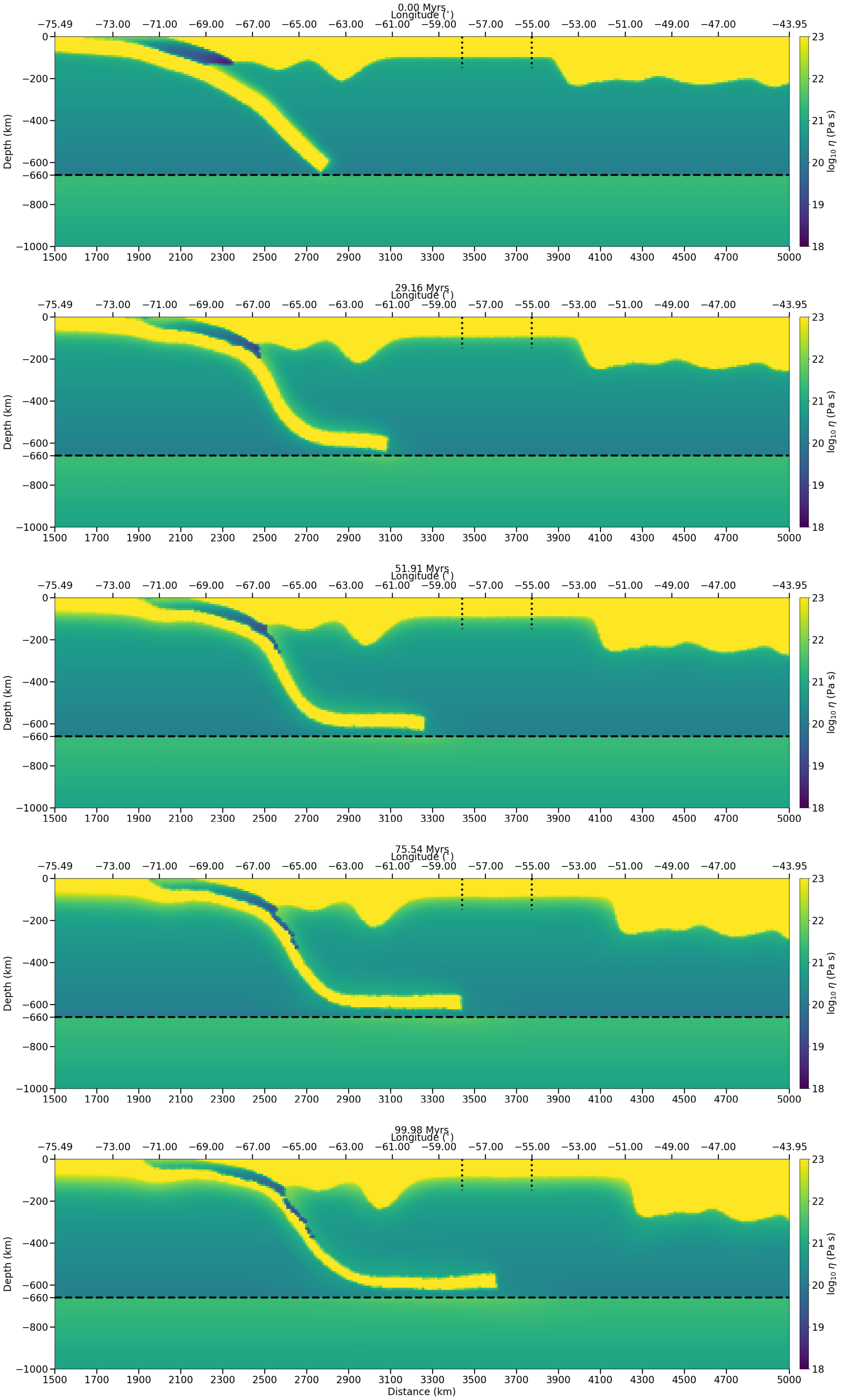

Figure B.10: Viscosity evolution for Simulation FCS 04.

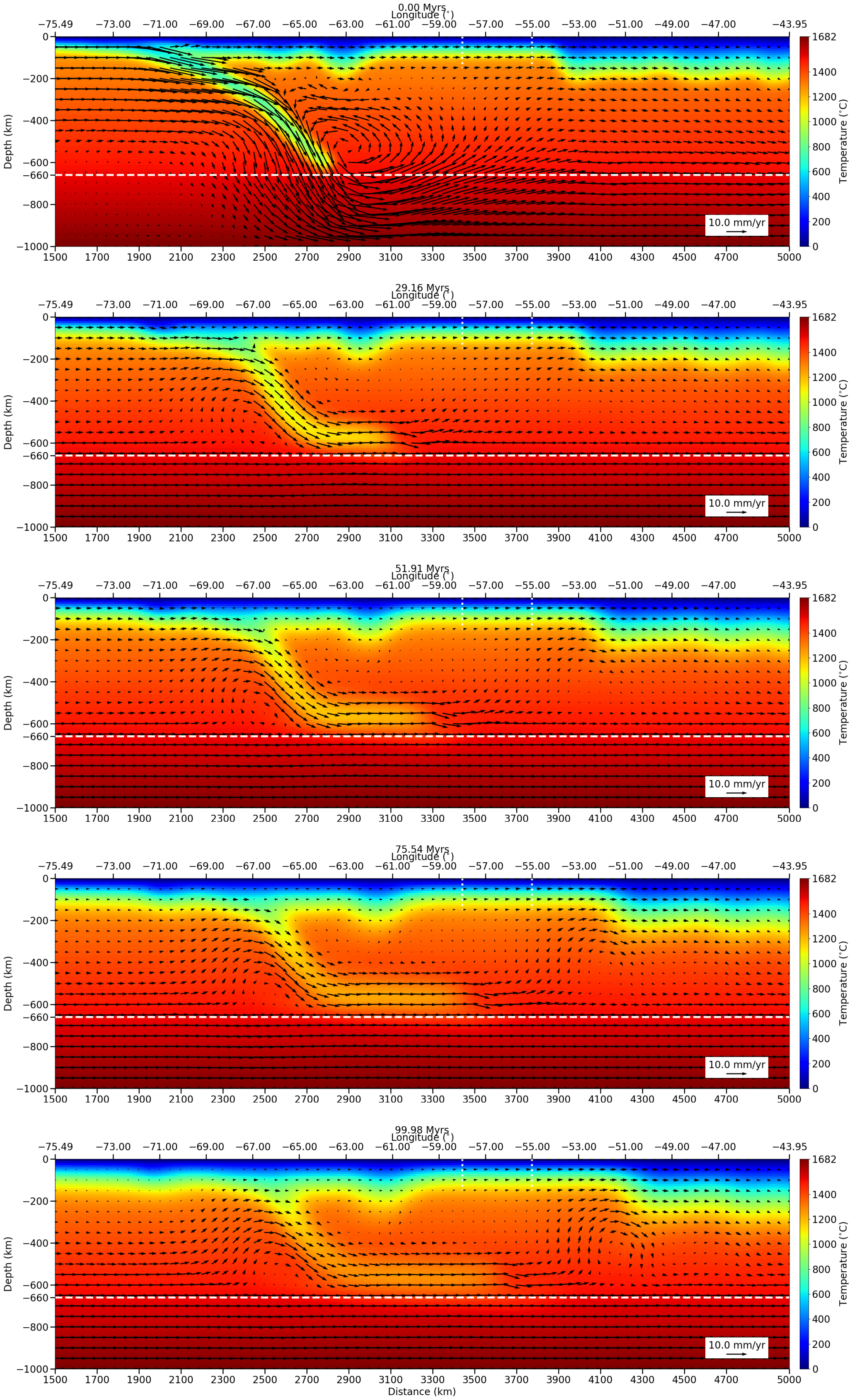

Figure B.11: Temperature and velocity field through time for Simulation FCS 04.

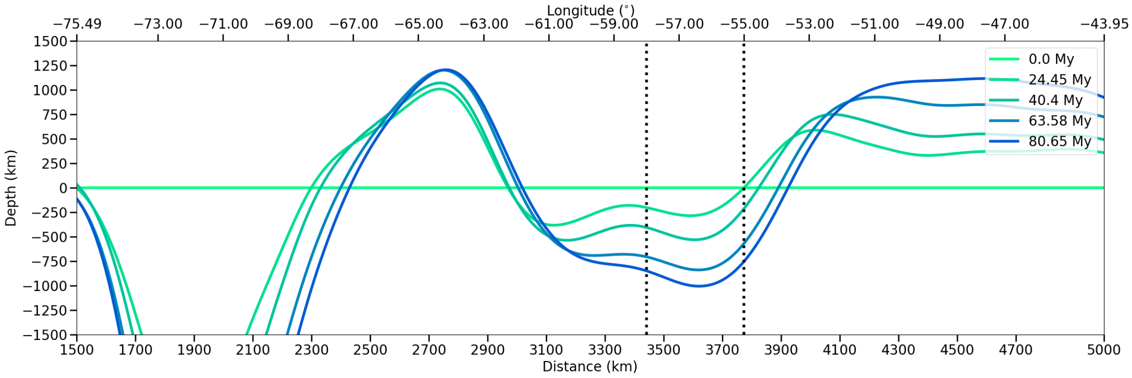

Figure B.12: Dynamic topography evolution for the Simulation FCS 04.

In this simulation it was possible to see the effect of a relativelly slow lower mantle with a velocity amplitude of $v_{LM} = 10$ mm/yr, half of the amplitude of the previous simulation for the same lower mantle density. As expected, the initial subduction angle is preserved better across the time steps, essentially making contact with the 660 km interface at the same position (Figure B.10). The subducting slab stretched noticeable less than the simulation with the same parameters but double v_{LM}.

Such initial configuration resulted in a convection cell right above the subducting slab slope (see Figure B.11), longitude $63 - 61°$W, an upward flow under the Pantanal basin region, and two regions with very low velocities at 60°W and 52°W.

Yet, the continent eastward migration is still non-negligible, compressed by the also moving oceanic lithosphere. The topography evolution is still not suitable for the boundary conditions.

B.0.2 Stationary continental slab - SCS

B.0.2.1 Lower mantle of $\rho_{OL} = 3300$ kg/m^3

Simulation $\rho_{OL} = 3300$ kg/m^3 01. SCS simulation, where $\rho_{LM} = 3300$ kg/m^3, $\rho_{OL} = 3300$ kg/m^3, $C_{OC} = 1000$, $C_{OL} = 1000$, $v_{LM} = 20$ mm/yr. The boundary conditions for the velocity are those from the SVM in Section 3.2.4, similar to Figure 3.9b.

Simulation $\rho_{OL} = 3300$ kg/m^3 02. SCS simulation, where $\rho_{LM} = 3700$ kg/m^3, $\rho_{OL} = 3300$ kg/m^3, $C_{OC} = 1000$, $C_{OL} = 1000$, $v_{LM} = 10$ mm/yr. The boundary conditions for the velocity are those from the SVM in Section 3.2.4, similar to Figure 3.9b, but the amplitude was halved.

Simulation $\rho_{OL} = 3300$ kg/m^3 03. SCS simulation, where $\rho_{LM} = 3400$ kg/m^3, $\rho_{OL} = 3300$ kg/m^3, $C_{OC} = 1000$, $C_{OL} = 1000$, $v_{LM} = 20$ mm/yr. The boundary conditions for the velocity are those from the SVM in Section 3.2.4, similar to Figure 3.9b.

Simulation $\rho_{OL} = 3300$ kg/m^3 04. SCS simulation, where $\rho_{LM} = 3400$ kg/m^3, $\rho_{OL} = 3300$ kg/m^3, $C_{OC} = 1000$, $C_{OL} = 1000$, $v_{LM} = 10$ mm/yr. The boundary conditions for the velocity are those from the SVM in Section 3.2.4, similar to Figure 3.9b, but the amplitude was halved.

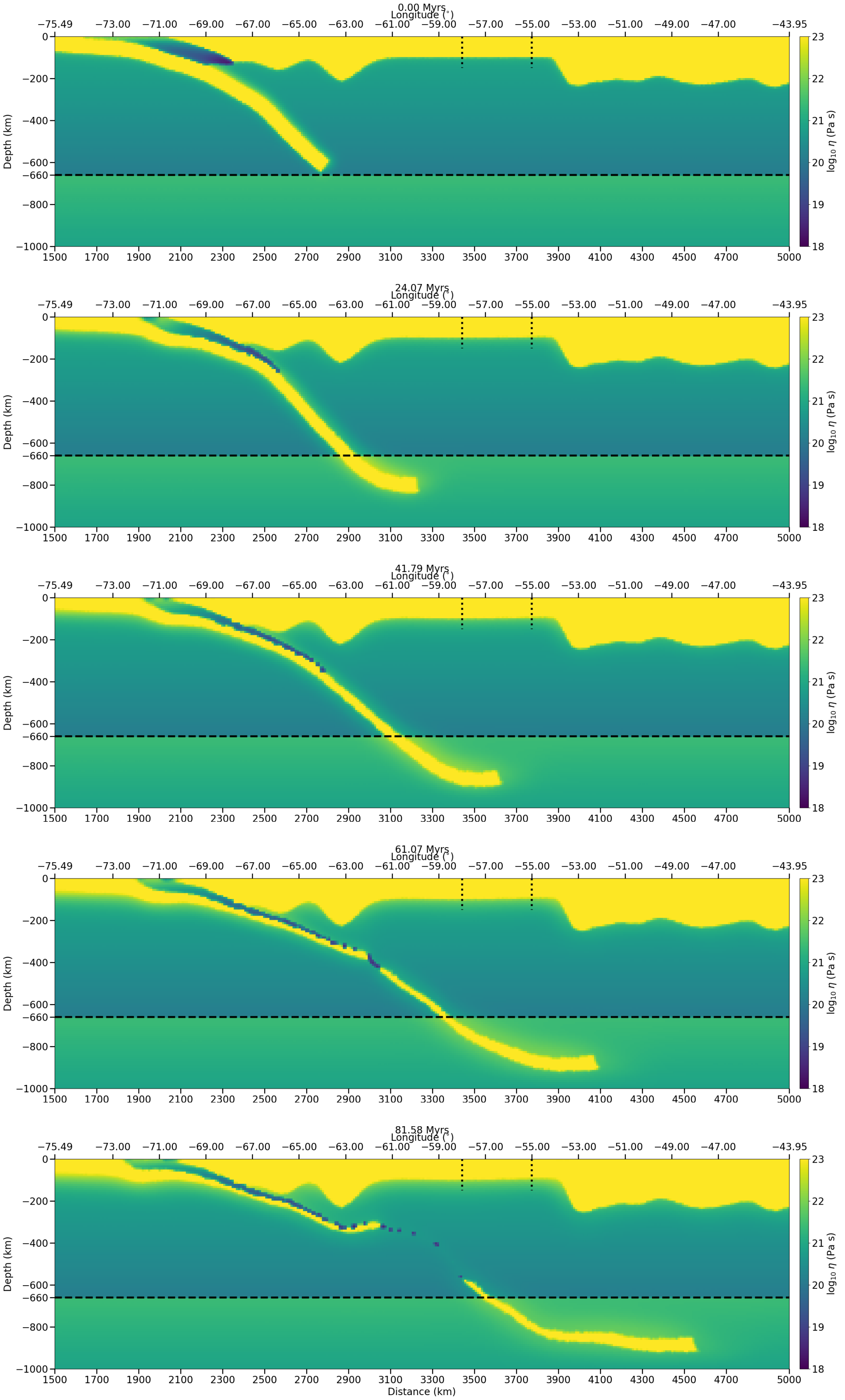

Figure B.13: Viscosity evolution for Simulation $\rho_{OL} = 3300$ kg/m^3 01.

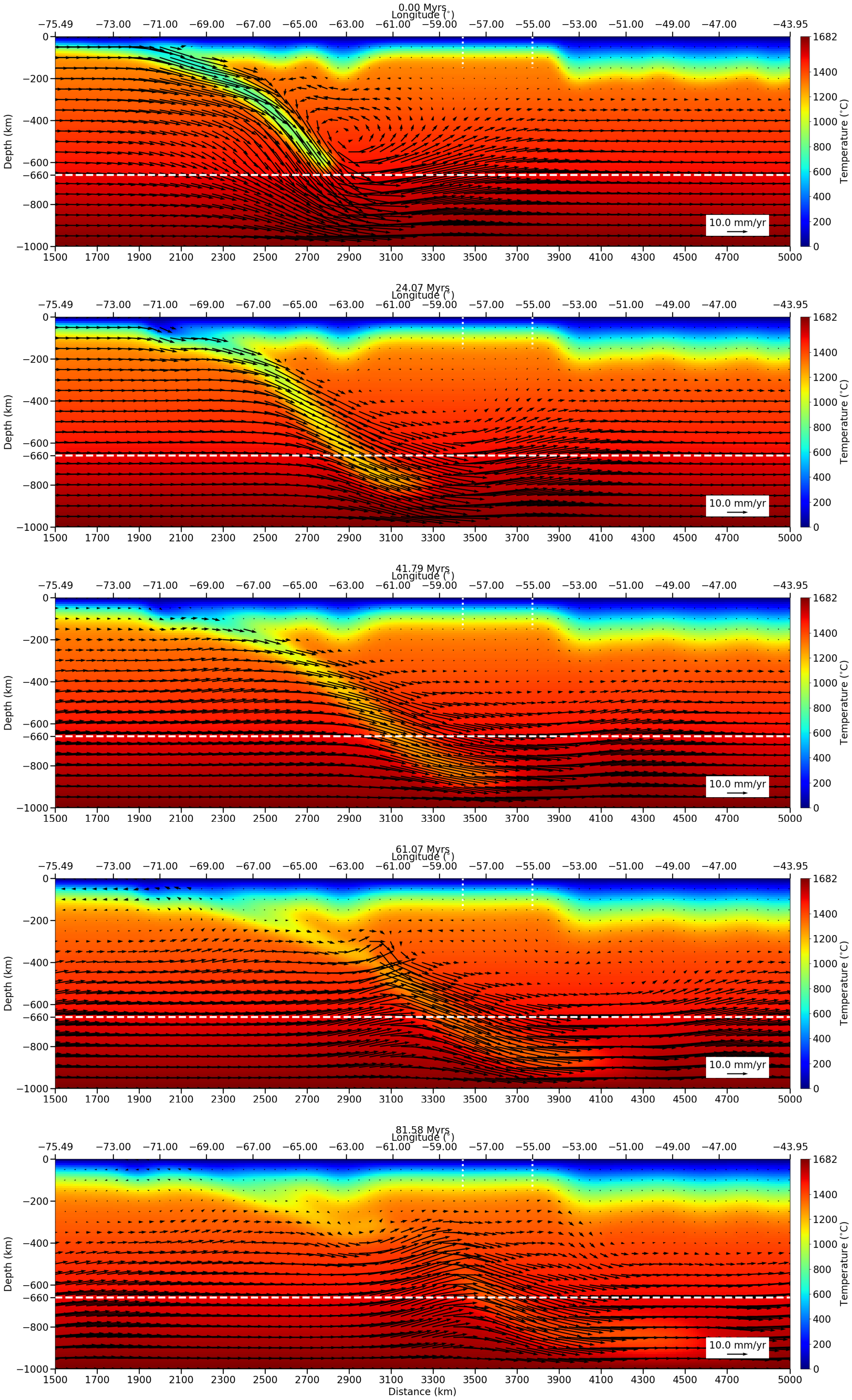

Figure B.14: Temperature and velocity field through time for Simulation $\rho_{OL} = 3300$ kg/m^3 01.

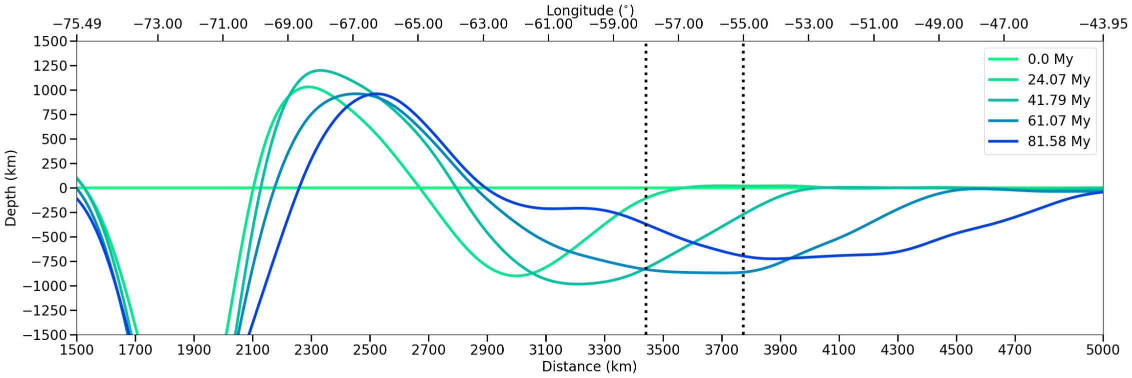

Figure B.15: Dynamic topography evolution for the Simulation $\rho_{OL} = 3300$ kg/m^3 01.

Because the continental lithosphere is fixed on the surface, the subducting slab was greatly stretched during the simulation.

It is possible to observe a clear break-off on Figure B.13 due to the relatively high velocity of the lower mantle, which dragged the slab with it. An interesting effect of such process is how the material flowed between the two now separated pieces (Figure B.14). This caused a more regional mantle flow under the continental area around 80 Myr and the now free tip of the subducting slab should warm up faster as its surface area increased.

The topography evolution map shown on Figure B.15 shows the passage of the subducting slab, its detachment and even the flow coming from the breach in the slab. The subducting slab passage is represented by the west-to-east subsidence evolution. The break-off is represented by the subsequent relative uplift.

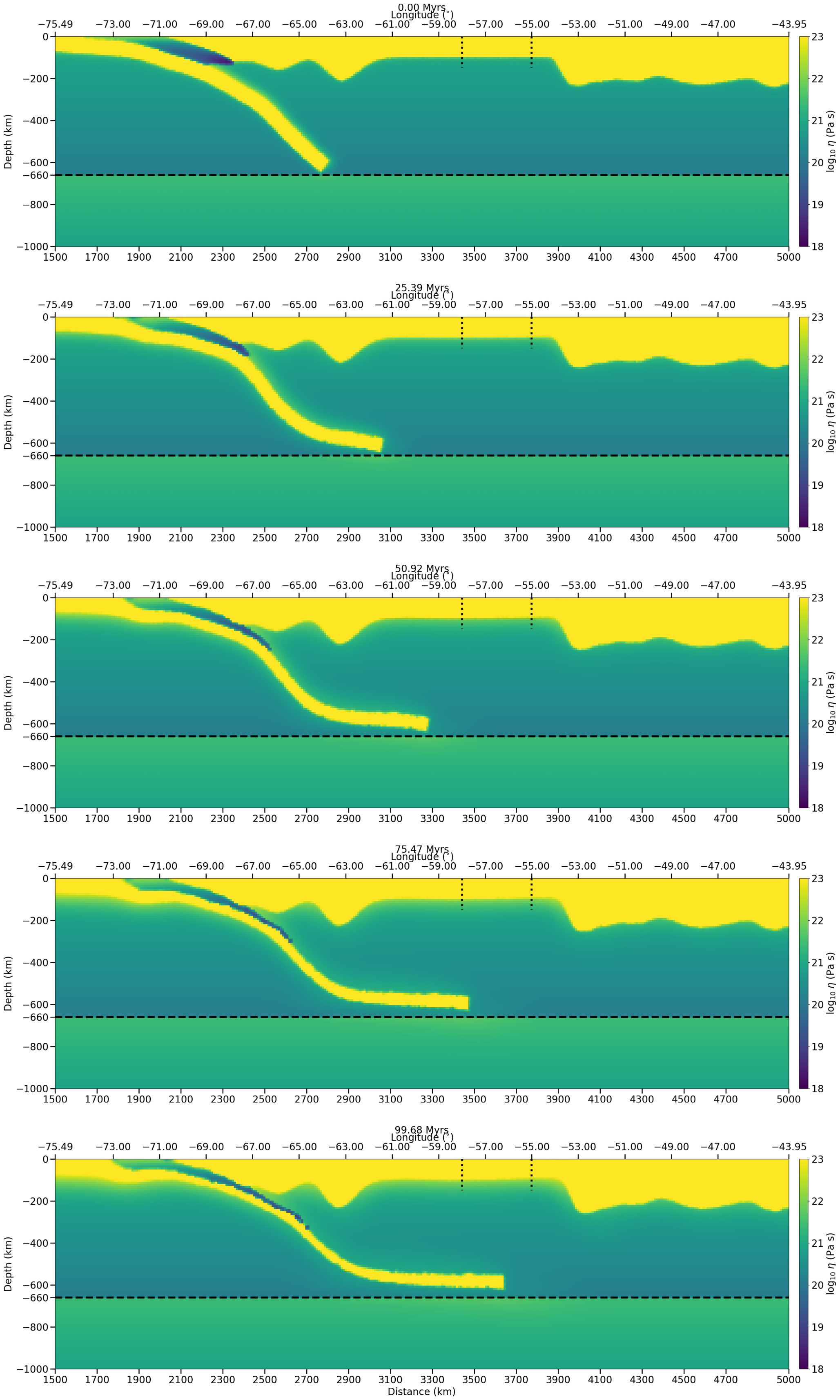

0.00 Myrs

25.39 Myrs

50.92 Myrs

75.47 Myrs

99.68 Myrs

Figure B.16: Viscosity evolution for Simulation $\rho_{OL} = 3300$ kg/m^3 02.

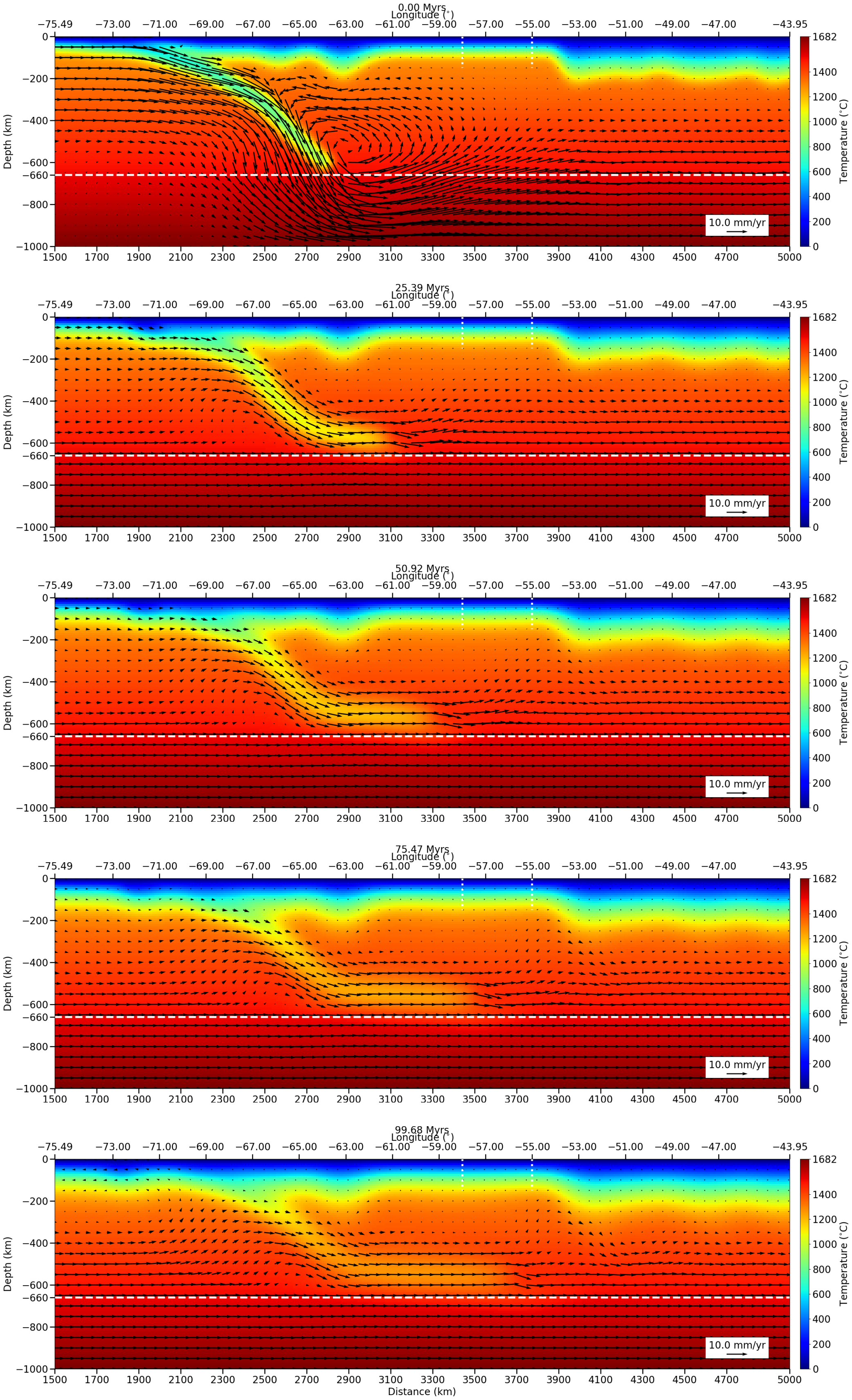

Figure B.17: Temperature and velocity field through time for Simulation $\rho_{OL} = 3300$ kg/m^3 02.

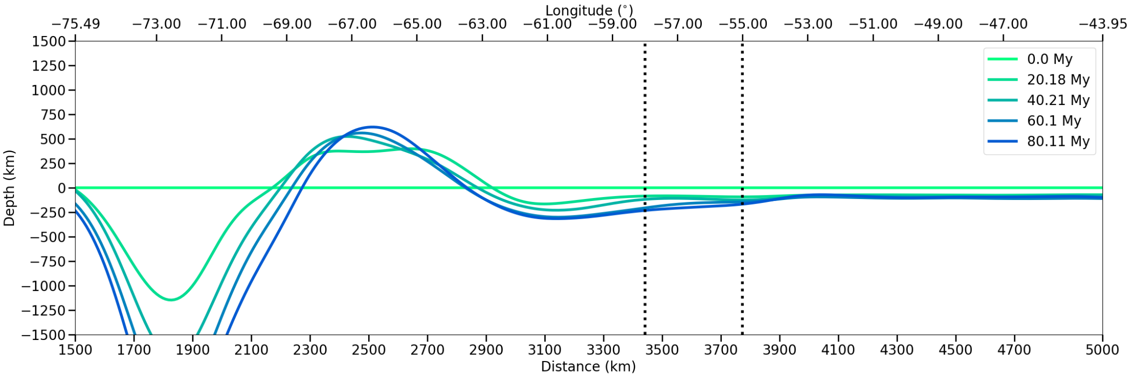

Figure B.18: Dynamic topography evolution for Simulation $\rho_{OL} = 3300$ kg/m^3 02.

The evolution of this simulations is essentially the same as the one presented in Figures 5.3 and 5.4. The difference is the amplitude observed for the dynamic topography (Figure B.18). As the slab moved slower, its temperature increased before it reached the same positions as the previous simulation (with double velocity).

The subducting slab stretched (Figure B.16) and the velocity field was mostly horizontal, from west to east, as seen on Figure B.17. In addition, a convection cell rotating anticlockwise is observed between the subducting slab plateau and the continental mass.

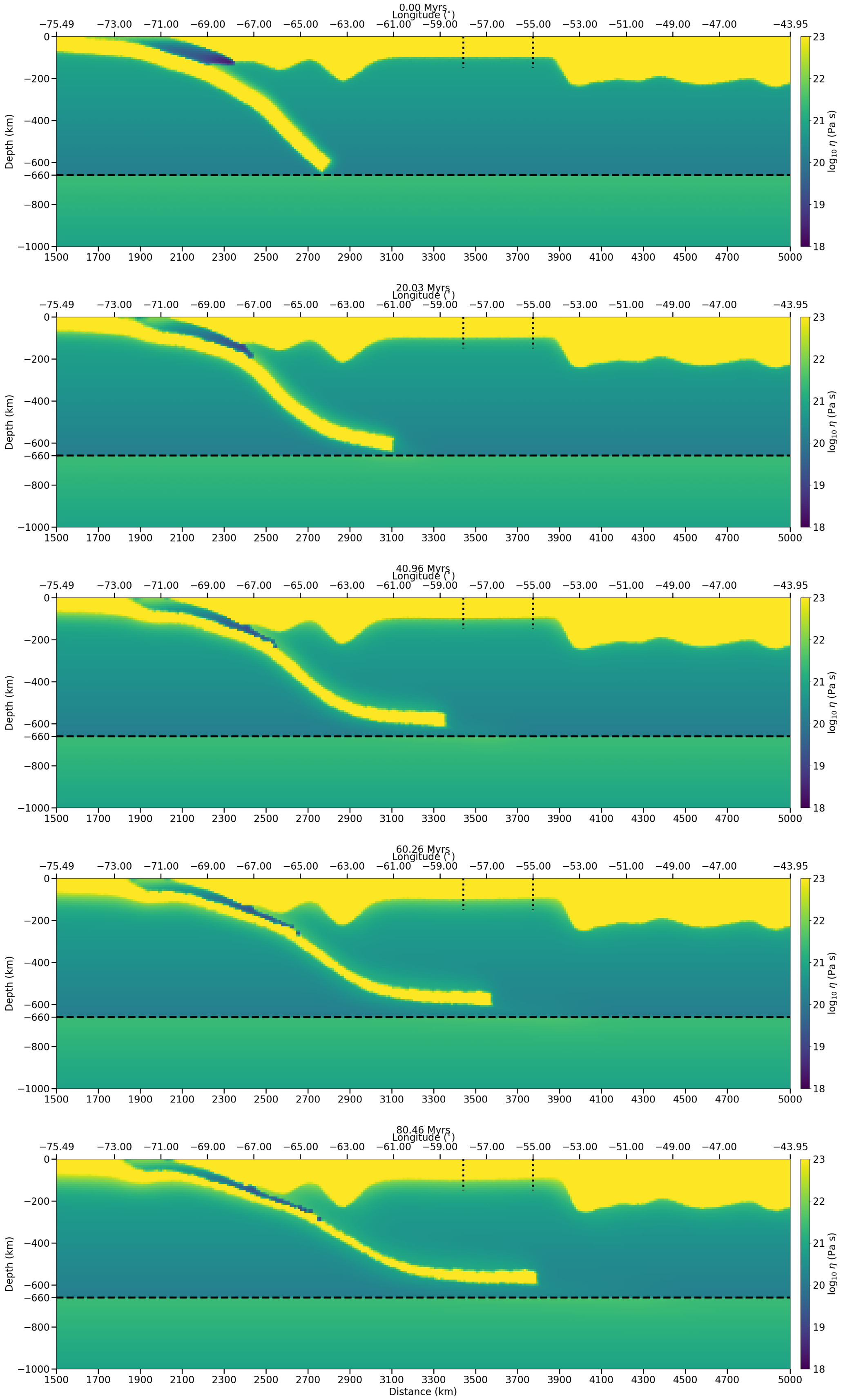

Figure B.19: Viscosity evolution for Simulation $\rho_{OL} = 3300$ kg/m^3 03.

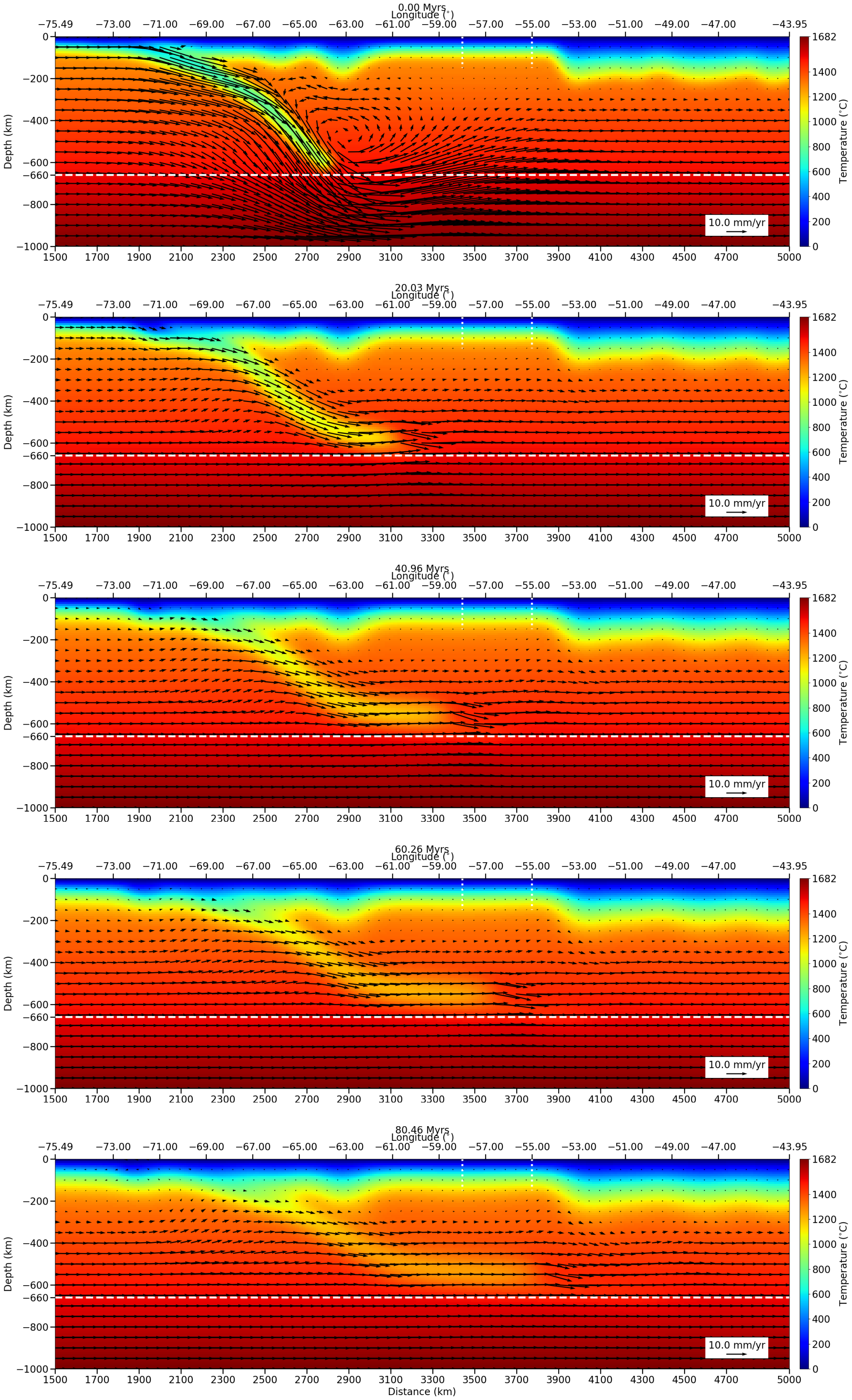

Figure B.20: Temperature and velocity field through time for Simulation $\rho_{OL} = 3300$ kg/m^3 03.

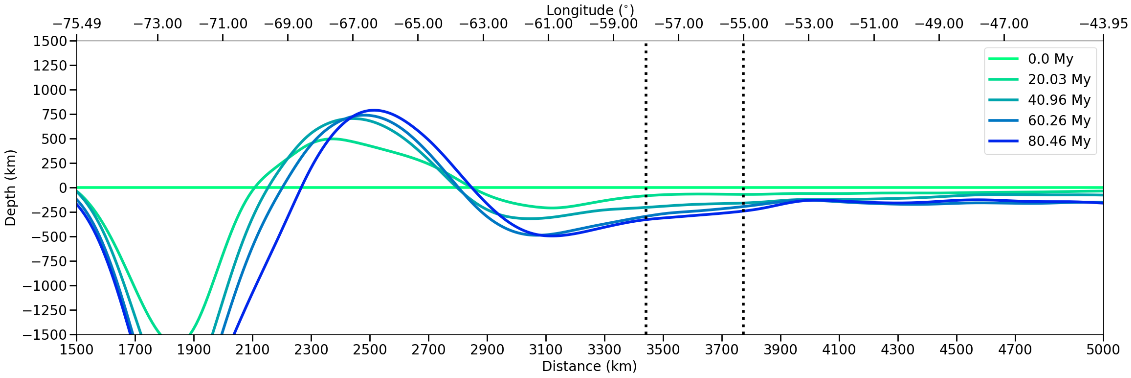

Figure B.21: Dynamic topography evolution for the Simulation $\rho_{OL} = 3300$ kg/m^3 03.

The purpose of the simulations with a lower mantle with a density of 3400 kg/m^3 was to assess how this change would manifest in the model. The result was that this simulation virtually indistinguishable from a simulation with a denser lower mantle, which means they are essentially the same.

For this simulation, the subducting plate stretched across the model, as seen on Figure B.19.

The thermal and velocity evolution profiles are very similar to the previous simulation, except the amplitudes are higher for the velocity field. The main flow followed a west-to-east trend and it is possible to observe an upward flow under the longitude of 54°W.

The dynamic topography (Figure B.21) shows the same trend from the previous simulation, where the subsidence rate increases towards the west for the continental region.

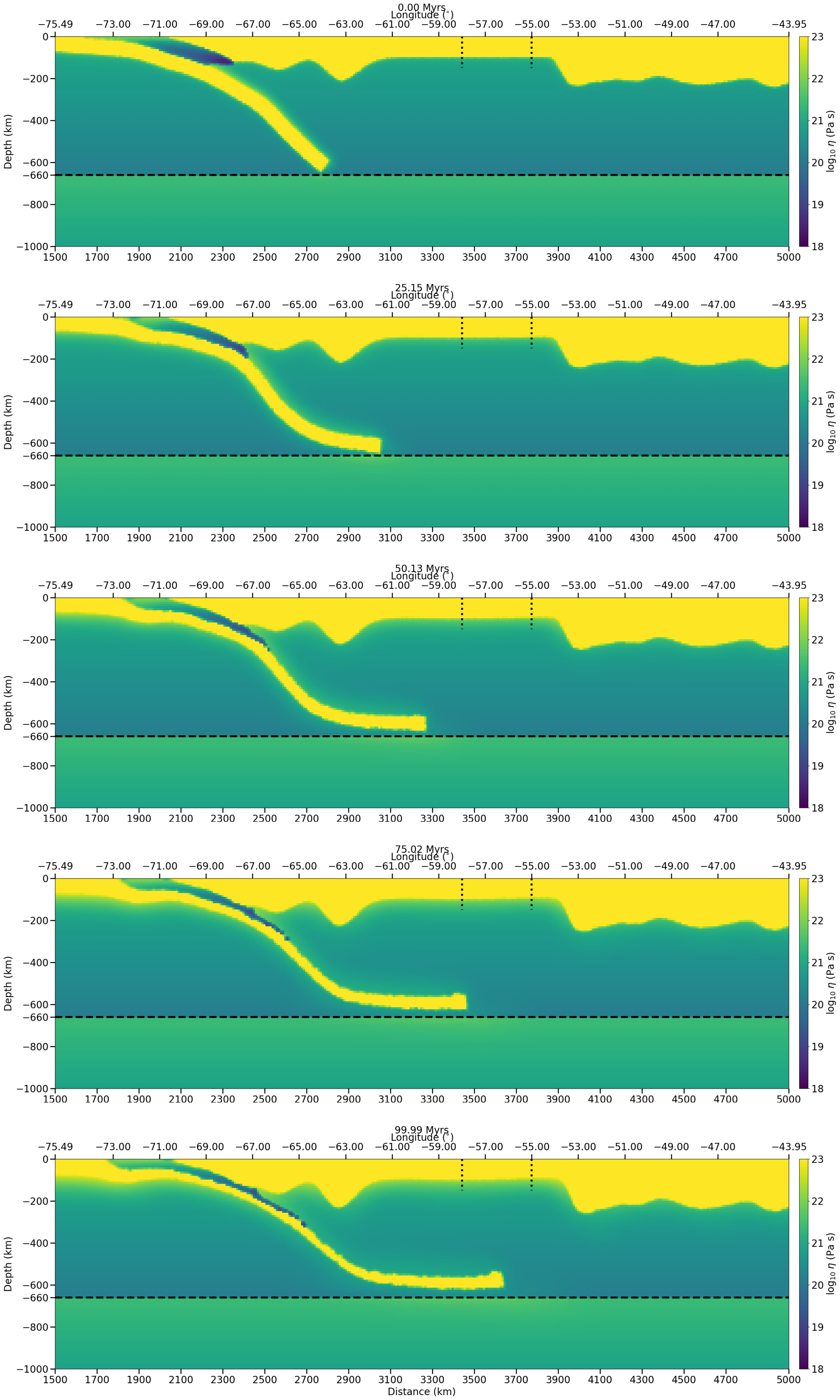

Figure B.22: Viscosity evolution for Simulation $\rho_{OL} = 3300$ kg/m^3 04.

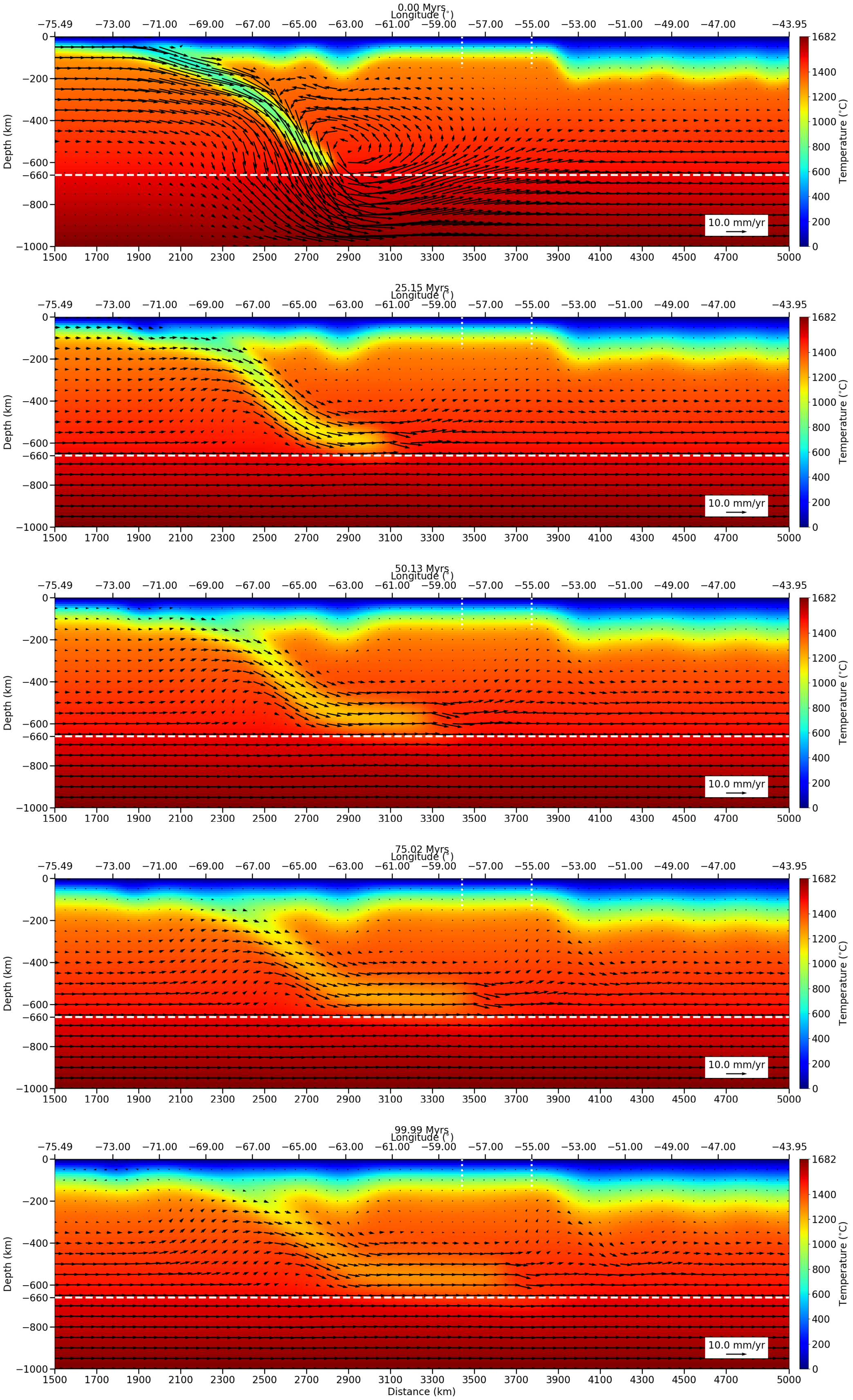

Figure B.23: Temperature and velocity field through time for Simulation $\rho_{OL} = 3300$ kg/m^3 04.

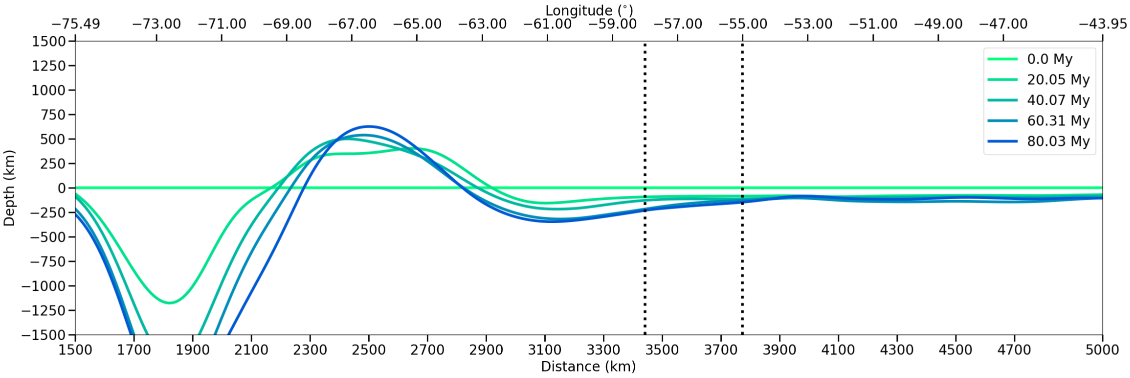

Figure B.24: Dynamic topography evolution for the Simulation $\rho_{OL} = 3300$ kg/m^3 04.

Figures B.22, B.23 and B.24 are essentially the same as the simulations presented on Figures B.16, B.17 and B.18. And the observations are the same.

B.0.2.2 Lower mantle of $\rho_{OL} = 3400$ kg/m^3

Simulation $\rho_{OL} = 3400$ kg/m^3 01. SCS simulation, where $\rho_{LM} = 3300$ kg/m^3, $\rho_{OL} = 3400$ kg/m^3, $C_{OC} = 1000$, $C_{OL} = 1000$, $v_{LM} = 10$ mm/yr. The boundary conditions for the velocity are those from the SVM in Section 3.2.4, similar to Figure 3.9b, but the amplitude was halved.

Simulation $\rho_{OL} = 3400$ kg/m^3 02. SCS simulation, where $\rho_{LM} = 3700$ kg/m^3, $\rho_{OL} = 3400$ kg/m^3, $C_{OC} = 1000$, $C_{OL} = 1000$, $v_{LM} = 10$ mm/yr. The boundary conditions for the velocity are those from the SVM in Section 3.2.4, similar to Figure 3.9b, but the amplitude was halved.

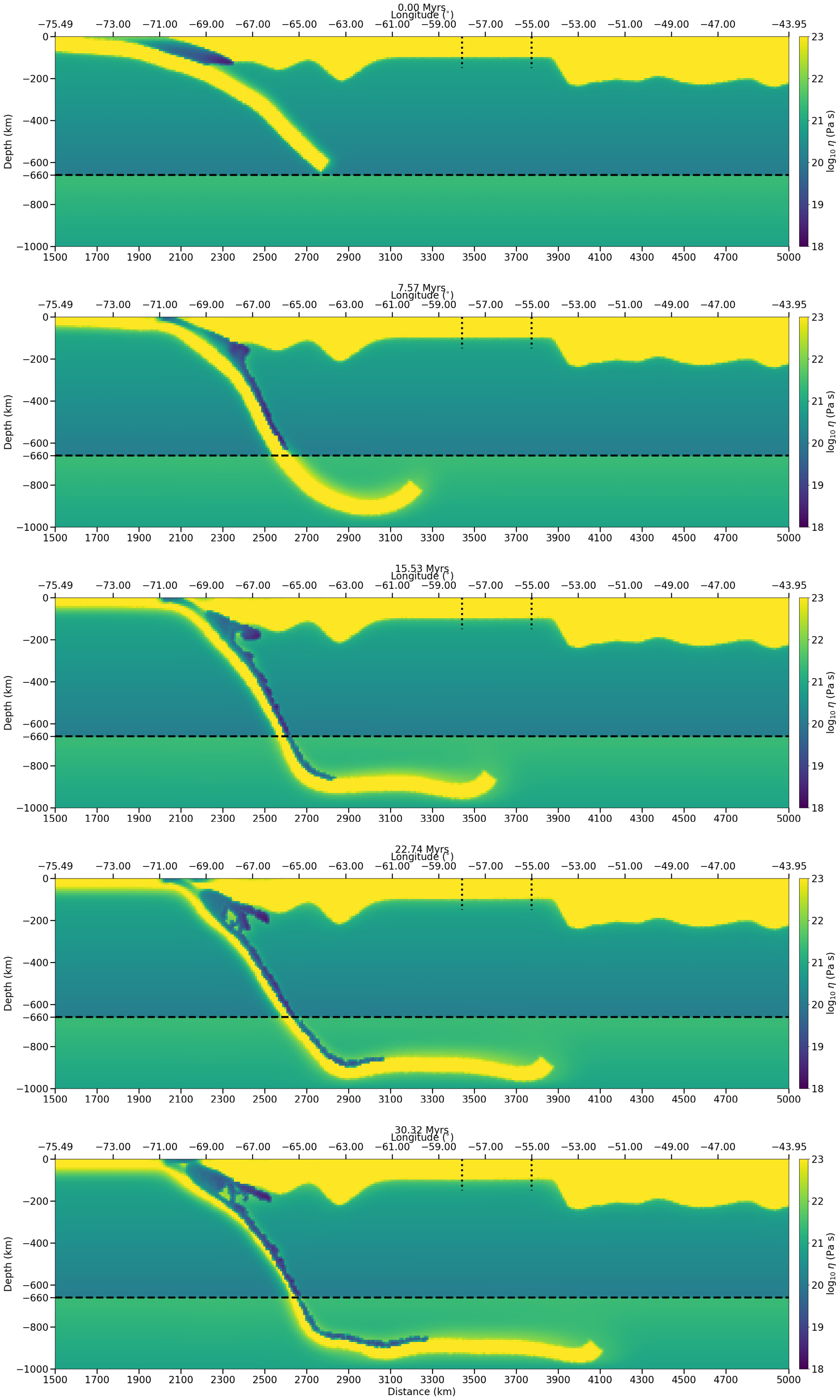

Figure B.25: Viscosity evolution for Simulation $\rho_{OL} = 3400$ kg/m^3 01.

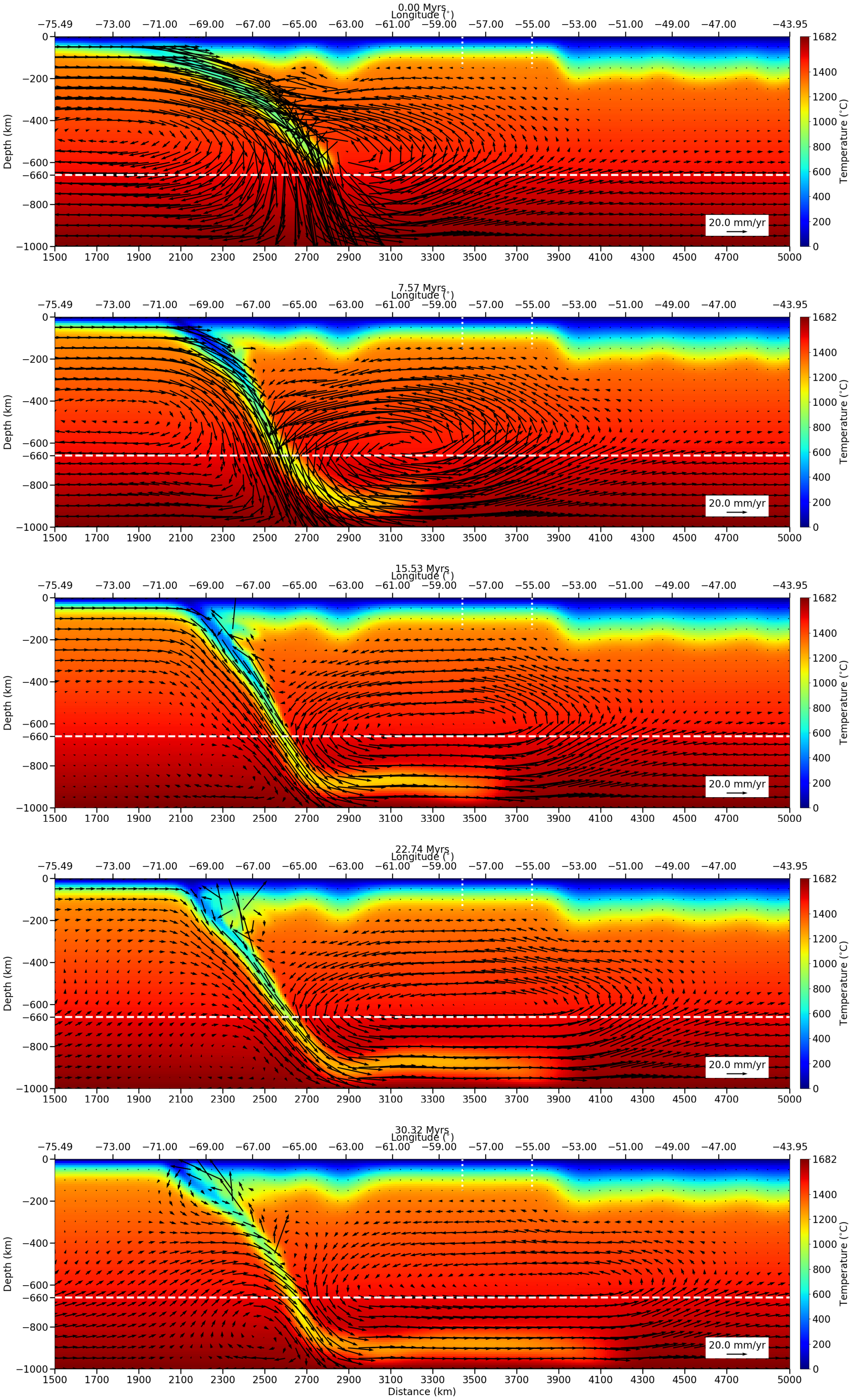

Figure B.26: Temperature and velocity field through time for Simulation $\rho_{OL} = 3400$ kg/m^3 01.

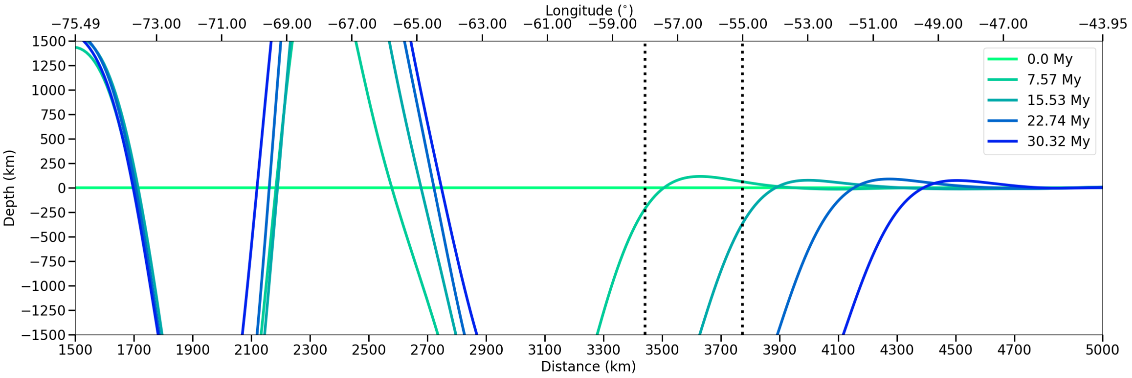

Figure B.27: Dynamic topography evolution for the Simulation $\rho_{OL} = 3400$ kg/m^3 01.

This simulation had a very similar result to the previous one, as the subducting slabs acquired the same velocity while penetrating the mantle (asthenospheric and lower).

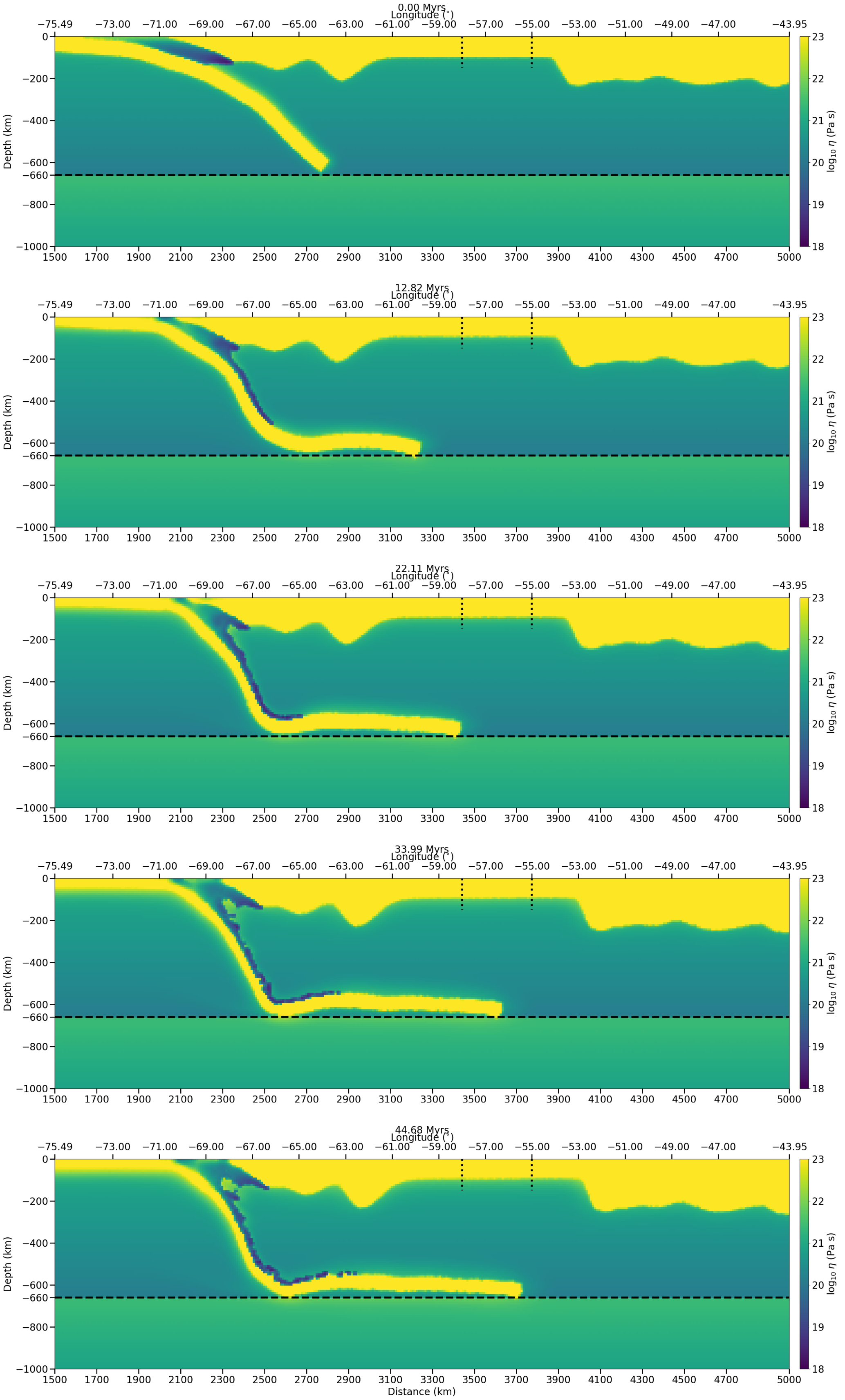

Figure B.28: Viscosity evolution for Simulation $\rho_{OL} = 3400$ kg/m^3 02.

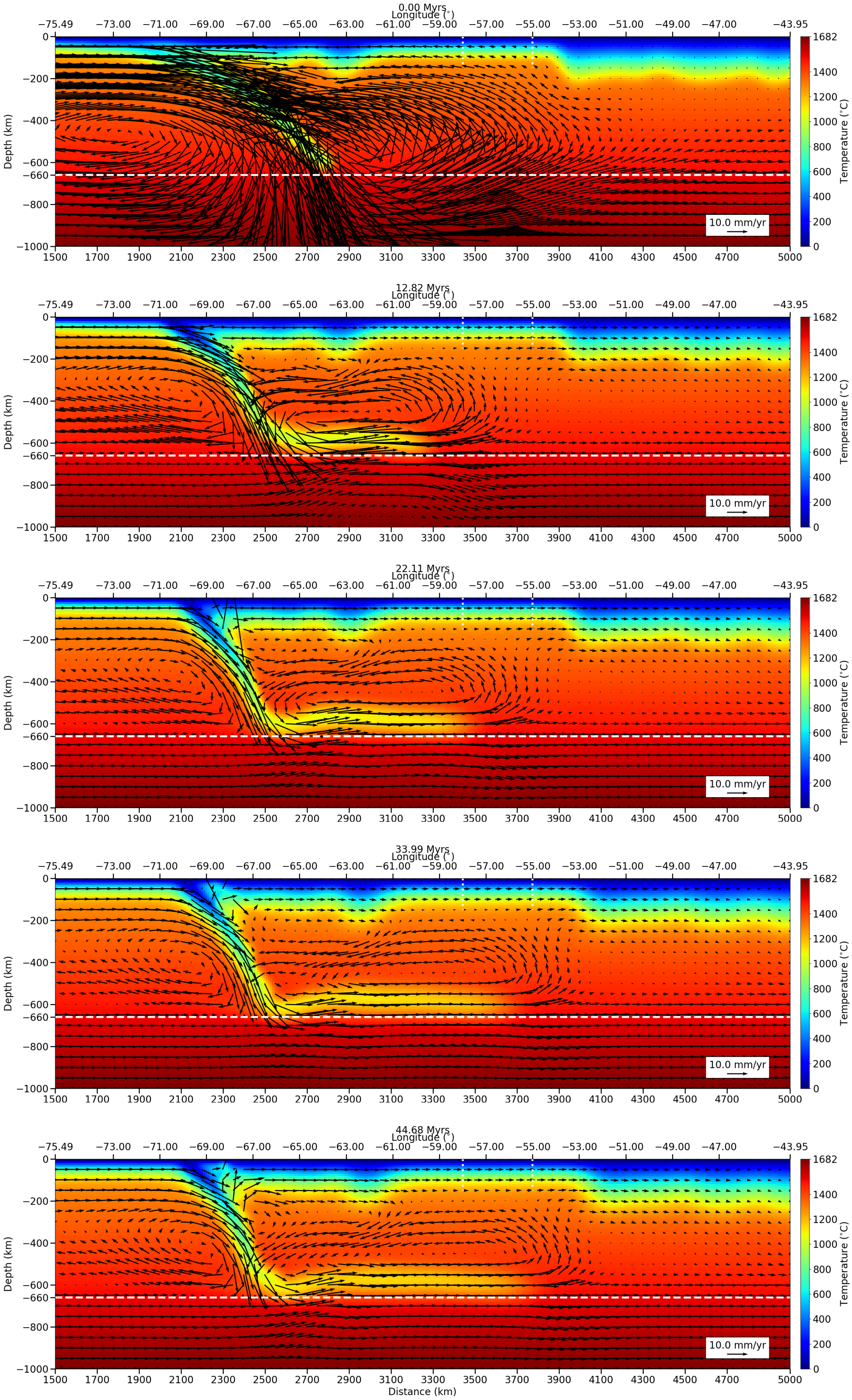

Figure B.29: Temperature and velocity field through time for Simulation $\rho_{OL} = 3400$ kg/m^3 02.